

Universidade de Santiago de Compostela
Departamento de Física de Partículas



**INVESTIGATING THE PRODUCTION
OF MEDIUM-MASS NEUTRON-RICH
NUCLEI**

David Pérez Loureiro
under the supervision of
José Benlliure Anaya

June 2010

UNIVERSIDADE DE SANTIAGO DE COMPOSTELA

José Benlliure Anaya, Profesor Titular de Física Atómica, Molecular y Nuclear de la Universidad de Santiago de Compostela,

CERTIFICO: que la memoria titulada **Investigating the production of medium-mass neutron-rich nuclei** ha sido realizada por **David Pérez Loureiro** en el **Departamento de Física de Partículas** de esta Universidad bajo mi dirección y constituye el trabajo de **tesis** que presenta para optar al **Doctor en Ciencias Físicas**.

Santiago de Compostela, Junio de 2010

Fdo: José Benlliure Anaya

Fdo: David Pérez Loureiro

*A quien pueda
interesar.*

Contents

| | |
|---|-----------|
| Introduction | 1 |
| 1. Production of nuclei far from stability | 5 |
| 1.1. The interest of nuclei far from stability | 5 |
| 1.2. The production of Radioactive Ion Beams | 8 |
| 1.2.1. Cross section | 8 |
| 1.2.2. Intensity of the primary beam | 9 |
| 1.2.3. Production target | 9 |
| 1.2.4. Reaction mechanisms | 10 |
| 1.2.5. Present limits of the nuclide chart | 18 |
| 1.3. Techniques for the production of exotic nuclei | 19 |
| 1.3.1. In-flight | 19 |
| 1.3.2. Isotopic Separation On-Line (ISOL) | 20 |
| 1.3.3. Hybrid techniques | 22 |
| 1.4. Existing RIB facilities | 23 |
| 1.4.1. ISOL | 23 |
| 1.4.2. IN-FLIGHT | 24 |
| 1.5. Future Facilities | 25 |
| 1.5.1. RIBF at RIKEN, Japan | 25 |
| 1.5.2. SPIRAL2 | 25 |
| 1.5.3. SPES | 26 |
| 1.5.4. HIE-ISOLDE | 26 |
| 1.5.5. FAIR | 27 |
| 1.5.6. EURISOL | 27 |
| 1.5.7. FRIB | 27 |
| 2. Experimental technique | 29 |
| 2.1. The experimental facilities | 29 |
| 2.1.1. The GSI accelerator system | 29 |
| 2.1.2. The beam monitor | 31 |
| 2.1.3. The targets | 32 |

| | | |
|-----------|--|-----------|
| 2.1.4. | The fragment separator (FRS) | 33 |
| 2.2. | The detection equipment | 35 |
| 2.2.1. | The multiwire chambers | 36 |
| 2.2.2. | The time projection chambers | 36 |
| 2.2.3. | The plastic scintillators | 38 |
| 2.2.4. | The ionization chambers (MUSIC) | 38 |
| 2.2.5. | The data acquisition system | 39 |
| 2.3. | Separation and identification of reaction products | 39 |
| 2.3.1. | Magnetic rigidity determination | 40 |
| 2.3.2. | Velocity determination | 41 |
| 2.3.3. | Atomic number determination | 42 |
| 2.3.4. | Mass-over-charge ratio determination | 43 |
| 3. | Production of medium-mass neutron-rich nuclei in fission re- | |
| | actions | 47 |
| 3.1. | Determination of the production cross sections | 47 |
| 3.2. | Measured cross sections | 52 |
| 3.2.1. | Energy dependence of the fission yields | 59 |
| 3.3. | Conclusions | 62 |
| 4. | Production of medium-mass neutron-rich nuclei using a two- | |
| | step reaction scheme | 65 |
| 4.1. | Description of the experiment | 65 |
| 4.2. | Isotopic separation and identification of fission residues | 67 |
| 4.3. | Isotopic separation and identification of fragmentation residues | 69 |
| 4.4. | Determination of the fragmentation cross sections | 70 |
| 4.4.1. | Efficiency of the detection set-up | 72 |
| 4.4.2. | Angular and momentum transmission | 73 |
| 4.4.3. | Secondary reactions | 73 |
| 4.5. | Results and discussion | 74 |
| 4.5.1. | Comparison with ^{136}Xe fragmentation results | 75 |
| 4.6. | Conclusions | 76 |
| 5. | Production of medium-mass secondary beams in future RIB | |
| | facilities | 79 |
| 5.1. | The FAIR facility | 79 |
| 5.2. | Production yields at FAIR | 82 |
| 5.3. | The EURISOL facility | 83 |
| 5.4. | Production yields at EURISOL | 86 |
| 5.4.1. | Production in fission | 86 |
| 5.4.2. | Two-step reaction scheme | 91 |

| | |
|---|------------|
| 5.5. ISOL Fission versus In-Flight fission | 101 |
| 5.6. In-flight fission versus fragmentation of fission residues | 102 |
| 5.7. Conclusions | 105 |
| Conclusions | 107 |
| Resumen en castellano | 111 |
| A. Measured fission cross sections | 123 |
| B. Measured fragmentation cross sections | 129 |
| C. Fit parameters for fission velocities | 131 |
| D. Release efficiency from ISOL targets | 133 |
| E. Layers of matter in the beamline | 135 |

Introduction

The subject of this dissertation is the investigation of the reaction mechanisms better suited for the production of medium-mass neutron-rich nuclei for the preparation of radioactive ion beams.

In recent years, radioactive ion beams have proven to be a powerful tool to explore the properties of nuclei. Until recently, most of our knowledge about structure of the atomic nucleus was based on the properties of nuclei close to the line of β stability, where the proton to neutron ratio is rather similar to that of stable nuclei. However, today we know that we cannot extrapolate this behaviour to regions far from stability. In fact, when we increase the number of neutrons, new phenomena are observed, such as the appearance new magic numbers, neutron halos or skins.

The availability of radioactive ion beams has made research on the limits of the existence of nuclei possible. On the proton-rich side, the proton dripline has been reached up to $Z=80$. However, on the neutron-rich side, the dripline has only been reached for the lightest elements ($Z=12$) and a vast region still remains unexplored. We have proposed the investigation of the production of medium-mass neutron-rich nuclei in order to study new areas of the nuclear landscape.

Medium-mass neutron-rich nuclei have shown very important implications in nuclear structure (neutron skins) and in nuclear astrophysics (r-process's path in stellar nucleosynthesis). However, experimental access to this region of the nuclear landscape is limited by the difficulties of producing radioactive beams of these species. The fission of actinides has been the mechanism used for the production of neutron-rich nuclei, in either in-flight or ISOL facilities. However, the production yields of nuclei in the $N=82$ shell lighter than Sn are very low. In addition, the refractory nature and short half lives of these elements, makes their extraction from ISOL targets impossible with the present technology. In order to overcome this difficulty, a two-step reaction scheme based on the fragmentation of neutron-rich fission fragments has been proposed.

In this work, both mechanisms for the production of medium-mass neutron-

rich nuclei are investigated: the fission of actinides, and the fragmentation of very neutron-rich fission fragments. Fission is studied at different excitation energies, in order to determine the optimum fission energy for the production of the largest number of very neutron-rich nuclei using this reaction mechanism. For this purpose, an experiment was performed in the FRagment Separator of the GSI facility in Darmstadt between November and December, 2006. In this experiment, the fission of a ^{238}U beam accelerated by the SIS synchrotron at 950 AMeV was induced, impinging onto a lead and a beryllium target. The two targets allowed us to study the fission at different excitation energies. During this experiment, the feasibility of the two-step reaction scheme was also investigated. A secondary beryllium target was placed at the intermediate focal plane of the FRS in order to induce the fragmentation of the fission fragments already identified using the first stage of the magnetic spectrometer.

Chapter 1 of this dissertation opens with an explanation of the motivation behind research with radioactive ion beams. This is followed by a description of all the different elements involved in the production of exotic nuclei, such as primary beam intensities, production targets and the reaction mechanisms better suited for populating different regions of the chart of nuclides. A brief summary is then given of the two different techniques used in the production of radioactive ion beams, the ISOL method and in-flight technique. The chapter ends with an overview of the existing and future radioactive beam facilities.

Chapter 2 describes the experiment we performed, with a detailed description of the FRS, the detection set-up and the separation method.

In Chapters 3 and 4 the results of the investigation of the production of medium-mass neutron-rich nuclei from fission or from fragmentation in a two-step reaction scheme are presented. The technique for the separation and identification of the reaction products is described, together with the method for determining the production cross sections. The different correction factors that had to be applied are also discussed. The results of the fission for both targets are compared with previous data found in the literature and with model calculations. The experimental data are also fitted in order to extrapolate the behaviour of the cross sections to large neutron excess, thus determining the optimum excitation energy for the production of medium-mass neutron-rich nuclei. The results obtained in the fragmentation of the ^{132}Sn , which was produced in the fission of the ^{238}U are presented in Chapter 4. The measured production cross sections for all the fragmentation residues are compared with the EPAX and COFRA codes. Data are also compared with the results obtained in the fragmentation of ^{136}Xe .

With the results obtained from the previous chapters, in Chapter 5 we

present realistic estimations of the production yields of medium-mass neutron-rich nuclei in future radioactive beam facilities in Europe, namely, EURISOL and FAIR. After a brief description of the facilities, an estimation of the production rates is given. Finally the yields obtained by different methods are compared for the two facilities, indicating the optimum mechanisms for the production of each nuclei.

This manuscript closes with a set of appendices that summarize all the measured production cross sections in both mechanisms, along with a list of all layers of matter present in the beam line and the release efficiencies used in the determination of the final yields.

Chapter 1

Production of nuclei far from stability

The present chapter is devoted to describe the production of exotic nuclei. We will begin by discussing why we are interested in the production of nuclei far off stability, and then move on to new phenomena discovered when approaching the limits of existence and the interest in these nuclei for describing stellar nucleosynthesis models. The following section explains all the factors involved in the production of radioactive beams, from primary beam intensities and target thickness to reaction mechanisms. Special attention will be given to those reaction mechanisms related with exotic nuclei produced by high-energy beams, which is the focus of our study. The third section describes the two techniques currently used to produce radioactive ion beams, the ISOL method and the in-flight technique. Finally, we will briefly describe the existing facilities and those being developed worldwide for this kind of research.

1.1. The interest of nuclei far from stability

The atomic nucleus is built of protons and neutrons, collectively called nucleons. Nucleon interactions are governed by the strong force, forming an intrinsically highly correlated, non-perturbative system. Atomic nuclei range from few-body systems up to the region of super-heavy elements with hundreds of nucleons. These provide an ideal terrain for theoretical many-body theories in a regime where perturbative approaches fail.

Nuclei that are stable against β decay are located in a very narrow band on the chart of nuclides (See Fig. 1.1). This chart shows the distribution of stable and known radioactive nuclei on a proton number *versus* neutron

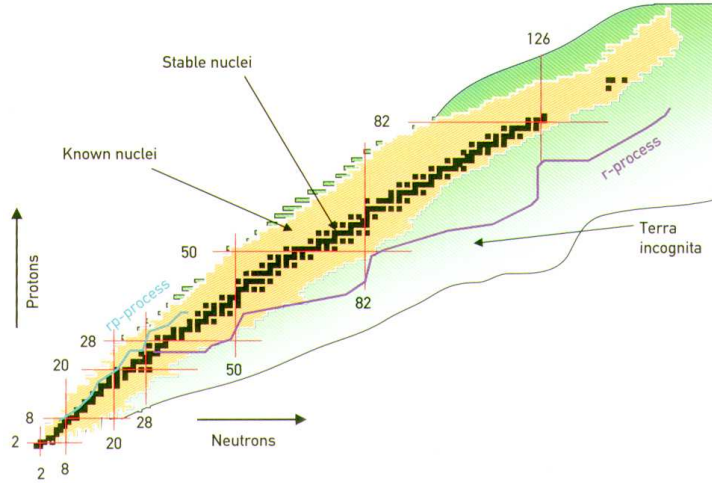


Figure 1.1: Chart of the nuclides: the border lines define the proton and neutron driplines. Black squares represent stable nuclei and light grey squares represent those radioactive nuclei already observed. The figure also shows the magic numbers for protons (neutrons) as vertical (horizontal) lines. Two nucleosynthesis paths can be seen: the *rp* process along the neutron deficient part of the nuclide chart, and the *r*-process, along the neutron-rich part.

number grid. Unbalanced neutron-to-proton ratios lead to a decrease in the stability of the nucleus. As more neutrons are added to a nucleus of a given proton number, the binding energy of the last neutron gradually drops and at a certain number the nucleus will decay instantaneously by neutron emission. In other words, the nucleus becomes unbound and the neutron *drip line* is reached. Similar behaviour is observed when we add protons. At present, the neutron drip line is only known for the light elements. It is much further away than the proton drip line because neutrons are not affected by the Coulomb repulsion. As more and more exotic nuclei become available, new properties are being observed, which we will describe in the following paragraphs.

Proton-rich nuclei The proton drip line has already been reached for a large number of elements. Beyond the proton drip line, valence protons are still confined by the Coulomb and centrifugal barriers. A nucleus beyond the proton drip line thus forms a quasi-bound state, from which it decays after a certain lifetime via tunneling of protons through the barrier [Hof82]. A peculiar situation can occur when single proton emission from the ground state is forbidden, but the emission of two protons is allowed [Gio02].

Neutron-rich nuclei While many neutron-deficient nuclei can be produced in nuclear reactions using stable beams, the region of neutron-rich nuclei is largely a *terra incongnita*. As mentioned before, the neutron drip line lies much further away from the valley of stability than the proton drip line does. In fact, neutron drip line has only be reached for elements up to $Z=13$ [Bau07]. Among the bound nuclei, ${}^8\text{He}$ has the largest N/Z value reached so far. However, larger values may be obtained in the formation of resonant nuclear systems beyond the drip lines: ${}^7\text{H}$ [Caa07] and ${}^{10}\text{He}$ [Kor94], have been observed as quasi-bound nuclear states. One of the most exciting discoveries in nuclear structure has been the observation of the halo nuclei, i.e., some of the nucleons extend far outside the region of their nuclear core [Tan85].

In heavier nuclei, although the drip line cannot be reached, nuclei of extreme neutron-to-proton ratio can be produced. The proton-neutron asymmetry leads to a weak binding which significantly alters nuclear matter properties. In stable nuclei, the strong proton-neutron attraction keeps the volumes occupied by the two species. Proton and neutron matter radii differ only marginally, mainly by Coulomb effects. In neutron-rich nuclei, this is no longer the case. The density distributions of proton and neutrons shift away from each other and the surface region is predominantly occupied by neutrons (neutron skins). The first experimental evidence for neutron skins was observed for sodium isotopes [Suz95]. The evolution of neutron skins with increasing neutron excess is expected to be a global trend.

Super-heavy elements In addition to the proton and neutron driplines a third limit of the existence of the nuclei arises with the maximum charge and mass a nucleus can reach. During the last decades nine new elements ranging from $Z=107$ to $Z=118$ have been discovered at GSI [Hof00] and Dubna [Oga06].

Shell structure There are indications that the shell structure changes as one moves towards very neutron-rich nuclei. A detailed understanding of how shell reorganization evolves with isospin is definitely needed. Quenching of the known shell gaps [GM84] and the appearance of new ones [Oza00] goes hand in hand with the evolution of shapes and deformations. There are only five stable isotopes with both neutron and proton magicity. This number can be doubled by going to unstable nuclei.

Nuclear astrophysics Nuclear astrophysics will strongly profit from the integrated information deduced from the nuclear structure data measured for

exotic nuclei. Research with exotic nuclei will even help us to understand the origin of the elements in our solar system. Above iron, nucleosynthesis proceeds on the neutron-rich side of the valley of β stability via a chain of neutron captures and subsequent decays towards heavier masses and higher- Z nuclei, as shown in Figure 1.1. Two different stellar processes are responsible for the production of heavy neutron-rich elements above iron, the s-process and the r-process. The s-process (slow neutron capture), primarily generates nuclei in close proximity to the valley of stability. In contrast, the r-process creates a wealth of extremely neutron rich nuclei by successive fast neutron captures and β decays. The proton rich part of the nuclide chart is populated by the rapid capture of protons (*rp-process*).

The last decade has provided a rich scientific harvest from exotic nuclear beam facilities which were installed worldwide. This has partly been due to the possibility of using unstable nuclei as secondary beams in nuclear reactions. Exciting new discoveries are expected in the unexplored regions of the nuclear landscape.

1.2. The production of Radioactive Ion Beams

The production of Radioactive Ion Beams (RIBs) can be synthesized in the following equation:

$$I = \sigma N_{target} \Phi \quad (1.1)$$

where I is the intensity of the secondary beam (s^{-1}) σ is the production cross section (cm^2), N_{target} is the number of target atoms per surface area (cm^{-2}) and Φ is the intensity of the primary beam. These three factors influence the production of exotic nuclei and should be optimized in order to overcome the current limits of the chart of nuclides.

1.2.1. Cross section

The cross section is the magnitude used to express the likelihood of interaction between particles. The value of this magnitude depends on the different reaction mechanisms and the energy of the primary beam. Different mechanisms enhance the production of specific isotopes. Fission produces neutron-rich isotopes, for example, while fusion + evaporation reactions produce more neutron-deficient isotopes. The different reaction mechanisms have to be combined in order to cover different regions of the nuclear landscape. A description of the different mechanisms is given in section 1.2.4. The influence of cross-sections in the production of exotic nuclei is directly

proportional, the larger the cross section, the higher the intensity of our secondary beam.

1.2.2. Intensity of the primary beam

As shown in Eq. (1.1), another factor which has to be taken into account is the intensity of the primary beam. Again, the intensity of the secondary beams produced is linear with the intensity of the primary beam and depends on the nature of the projectiles used. For light projectiles, like protons, the development of superconducting linear accelerators (SC LINACS) allows to produce high energy proton beams with intensities of 1 mA¹, although intensities up to 5 mA can be achieved. Heavy ions are usually accelerated by cyclotrons and synchrotrons. However the production of very high intensity beams is not easy, due to the space charge effects that affect to the quality and stability of the beams. At this time, intensities of 10¹² ions/s are difficult to achieve.

1.2.3. Production target

The production target is the last factor which has to be taken into account for the production of exotic nuclei. Generally, the thicker the target, the larger the production. However, both, the range of the projectile in target and the energy deposited by the projectile must also be taken into account.

Projectile Range

The projectile range is directly related to the energy of the primary beam. With low energy beams, the range of the projectile will be very short, and the probability of having a nuclear reaction very small, as can be seen in the left panel of Figure 1.2. As the energy of the beam increases, the probability of interaction increases, as does the range of the particle. Therefore, the use of more energetic beams, requires the increase of the thickness of the target. Figure 1.2 also shows the reaction probability for different projectile-target combinations, and how using a heavy projectile (target) with a light target (projectile), produces a very high probability of nuclear reaction at moderated energies, when compared to the use of heavy projectiles and targets.

¹1 mA is 6×10^{15} protons/second

Deposited energy

The main problem of using high energy charged beams is the energy deposited by the beam in the production target due to atomic interactions. This limits the maximum intensity which can be used for the primary beam corresponding to a determined target thickness, because the very high energy deposition deteriorates the production target. Cooling systems such as water cooled rotating targets [Yos04] or liquid metal targets [Nol03] are required to prevent this situation. Figure 1.2 illustrates how the use of light projectiles at energies around few hundreds of MeV, maximizes the probability of having a reaction in the target, while keeping the energy deposition low.

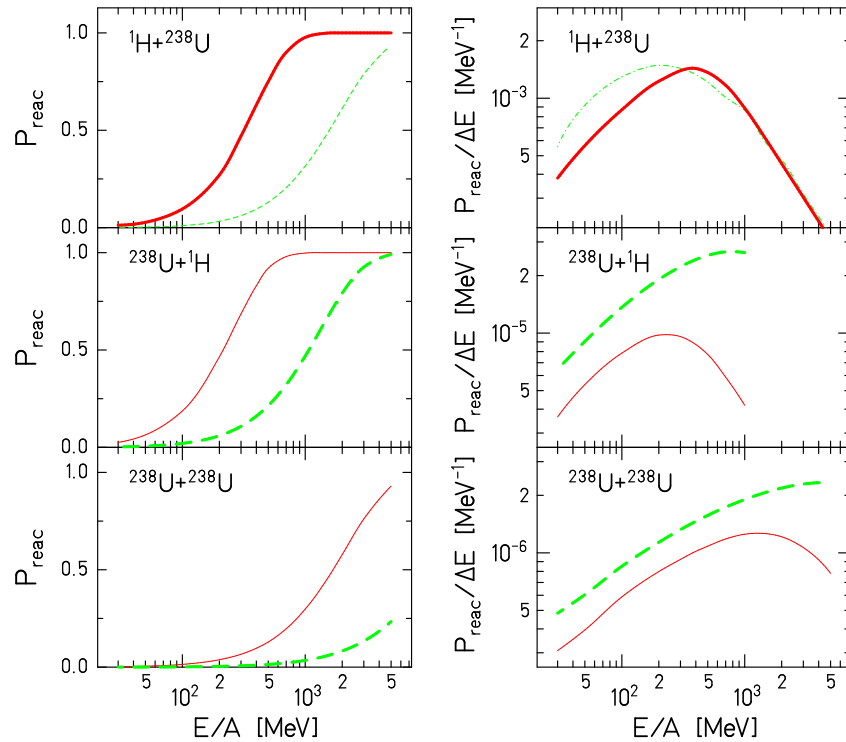


Figure 1.2: Reaction probability (left panel) and ratio between reaction probability and energy deposited in the production target (right panel), for thick (solid line) and thin (dashed line) production targets.

1.2.4. Reaction mechanisms

In order to optimize the production yields we can select different reaction mechanisms according to the projectiles to be used or the region of the chart

of nuclei we want to populate. These are described in the following subsections with emphasis on the reaction mechanisms related to reactions at high energies, and fission.

Uncharged projectiles

To avoid the problem of the heat load in the production targets due to the very high intensity of the primary beams, the use of uncharged projectiles like neutrons and photons has been considered. High energy neutrons can be produced by a high energy proton driver from spallation reactions, or using a deuteron beam with a Be/C converter. High fluxes of thermal neutrons are produced by nuclear reactors. Another option is to use an intense electron accelerator associated to a tungsten converter, producing a high flux of energetic photons from *bremstrahlung*. In all methods, the neutral particles are used to induce hot or cold fission on an actinide target, leading to the production of very neutron-rich nuclei.

Low energy beams

Another possibility for avoiding the problem of the high power deposited in the production targets is to lower the energy of the beam. Fusion-evaporation reactions are the main reaction mechanism for lower energies. This reaction with light ions, mainly produces nuclei close to stability on the neutron deficient side of the nuclide chart. The advantage of this mechanism for light ions is the high cross section of the reactions. However, although fusion reactions with heavier ions present similar cross sections, they mainly lose protons during the evaporation process, therefore it will be very difficult to produce very proton-rich heavy nuclei from fusion reactions.

Other possibilities at low energy beams include the multinucleon transfer reactions at energies around the Coulomb barrier [Szi05] and the deep inelastic transfer reactions [Sou07]. Both mechanisms, have shown an enhancement in the production of neutron-rich reaction residues when using neutron-rich targets.

High energy beams

The reaction mechanisms discussed in the previous section produce a limited number of different isotopes with a small range in isospin covered. In this section we will describe two processes in which hundreds of different elements, with a very wide range in neutron-proton ratio are produced. High energy beams have a higher range in the production target, maximizing the reaction probability. The high energy involved in the reactions will also

produce more isospin fluctuations, thus covering a larger range of the nuclear landscape. Projectile fragmentation, as well as spallation reactions² are the two reaction mechanisms which take place at high energies.

Nuclear reactions at relativistic energies are usually explained based on the two-step mechanism proposed by Serber [Ser47]. According to this model, inelastic nuclear reactions at relativistic energies can be described in two steps that occur in two different time scales. In the first stage, the interaction of both reaction partners may modify their composition and introduces a certain amount of excitation energy. The characteristic time of this reaction step is $\sim 10^{-23}$ s. In the second reaction step, the system reorganizes, that is, it thermalizes and de-excites by the evaporation of protons, neutrons and light nuclei, as well as by fission and emission of γ -rays. According to the statistical model, the characteristic time for the emission of particles varies depending on the excitation energy.

Fast initial step There are several models that describe this first step. Some of the mostly used are the intra-nuclear cascade model (INC) [Met58] and the abrasion model [Bow73]. The INC model is based on a microscopic description in which the nuclear reaction is interpreted as a series of nucleon-nucleon collisions.

The abrasion model is a macroscopic description based on the picture of a clean cut of the target nucleus by the projectile and *vice versa*. The overlapping areas contain the nucleons that actually interact in the collision (*participants*). Outside the interaction region the nucleons are not affected by the collision and remain as *spectators*. After abrasion most of the participants have left the collision region and only spectators remain. The target spectator is nearly at rest and the projectile spectator move with almost the velocity of the initial projectile. Initially, the excitation energy was understood as the excess of the surface energy of the deformed prefragment with respect to a sphere of equal volume [Gos77]. This excitation energy was later explained as the creation of vacancies in the Fermi distributions of the prefragment [Gai91].

In INC models, the incident nucleons follow straight trajectories until they collide with a target nucleon. These models usually offer a semi-classical description in which the nucleons see each other. Relativistic kinematics is used and reflexion and refraction effects due to the nuclear potential are taken into account. These models are implemented in simulation codes and are continu-

²Spallation and fragmentation refers to the same reaction but in inverse kinematics. The first is produced by light projectiles on heavy targets, while the latter is the inverse process that of a heavy projectile impinging upon a light target.

ously tested with the available experimental data in a wide range of reactions. Typically there are two types of INC codes, depending on the treatment of the nuclear medium: the *Bertini-like* codes [Yar79; Yar81] and the *Cugnon-like* codes [Cug87; Bou02]. In Bertini-like codes the nuclear density is considered as continuous and in Cugnon-like, the nucleons are treated individually from the beginning. In both codes, the elastic and inelastic nucleon-nucleon interactions are defined from free Nucleon-Nucleon-cross sections. In the case of inelastic collisions, pion production and absorption occur from the production of the Δ resonance. The cascade is initiated with the interaction of the projectile with the target and stops when some cut-off condition is fulfilled.

Statistical de-excitation The statistical model describes the de-excitation of the pre-fragment formed in the initial stage of the collision assuming Bohr's compound nucleus hypothesis [Boh36]. According to this hypothesis, the pre-fragment reaches the statistical equilibrium defined by its excitation energy and angular momentum. This implies that all possible decay channels have on average the same probability of being populated. The excitation energy is then dissipated, either by particle or photon emission or by fission. Assuming that the residue at each step is a compound nucleus, the de-excitation chain continues as long as excitation energy is available.

The probability $P(\omega)$ of a certain de-excitation channel ω at a certain evaporation step is

$$P(\omega) = \frac{\Gamma_{\omega}}{\sum_{\Omega} \Gamma_{\Omega}} \quad (1.2)$$

where Γ_{ω} is the width of the specific channel.

For the treatment of the evaporation of particles, the decay widths are obtained based on the statistical model proposed initially by Weisskopf [Wei37; Wei40] which was later improved by Hauser and Feshbach [Hau52], who introduced a proper treatment of the angular momentum. Another formulation of the statistical model based on the transition state method allowed Bohr and Wheeler the description of the fission process [Boh39].

Particle emission As mentioned before, the particle-decay widths are obtained based on the Weisskopf model. The principle of detailed balance for two systems a and b in statistical equilibrium with level densities ρ_a and ρ_b states that:

$$\rho_a \Gamma_{ab} = \rho_b \Gamma_{ba} \quad (1.3)$$

where Γ_{ab} is the decay width for the transitions from a to b and Γ_{ba} is the decay width of the reverse process.

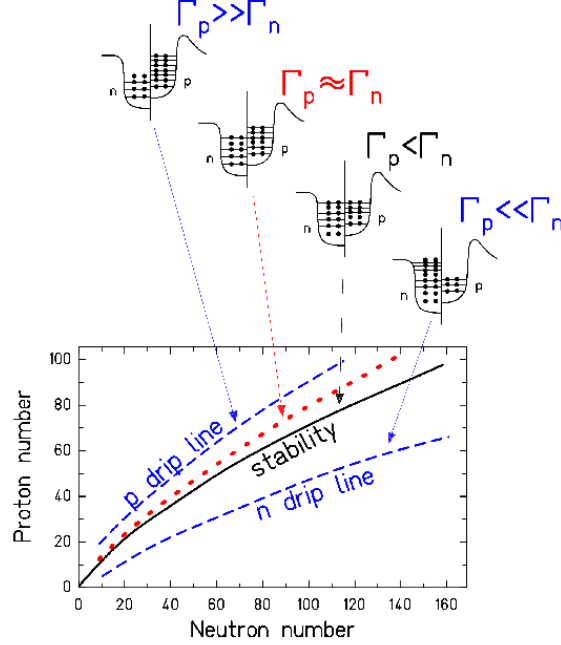


Figure 1.3: Schematic illustration of the evaporation attractor line (light-grey dashed line). See text for details.

Following this description, we can write the width of a certain channel integrating in energy the probability of emission from an initial compound nucleus with energy E_i and angular momentum J_i , to a final compound nucleus with energy and angular momentum E_f, J_f as

$$\Gamma_\nu = \int_{S_\nu - B_\nu}^{E_i - B_\nu} \left[\sum_{J_f} \frac{1}{2\pi} \frac{\rho(E_f, J_f)}{\rho(E_i, J_i)} \sum_{S=|J_f-s|}^{|J_f+s|} \sum_{l=|J_i-S|}^{|J_i+S|} T_l(u) \right] du \quad (1.4)$$

where $\rho_{i/f}$ are the level densities of the initial/final states, s is the spin of the emitted particle, l is the angular momentum between the residue and the emitted particle, B is the Coulomb barrier and S_ν the separation energy. T_l are the transmission coefficients, given by the penetration through the potential barrier for the inverse process.

The neutron and proton evaporation are generally the most important evaporation channels. The competition of these two channels produces the so called *evaporation corridor*. Figure 1.3 shows the occupied single particle levels on different region of the nuclide chart. On the beta-stability line, the Fermi levels of protons and neutrons are equal. However, neutron evaporation prevails for stable nuclei because proton emission is suppressed by

the Coulomb barrier. Thus the daughter nucleus becomes more and more neutron-deficient and consequently, the Fermi level of the protons increases, lowering the proton separation energy. At a certain point, the decay widths for protons (Γ_p) and neutrons (Γ_n) becomes comparable, and the evaporation of neutrons and protons reaches an asymptotic equilibrium. When starting from a proton-rich nucleus the evaporation of protons will prevail, also approaching the equilibrium from the other side. Therefore, there is a line where all the evaporation residues will finally end, if the evaporation cascade is long enough. This line is called the attractor line [Cha98] and the residue distribution in asymptotic equilibrium is called the evaporation corridor. Figure 1.4, shows the calculated production yields in the reaction $^{136}\text{Xe}+^1\text{H}$ for different energies of the projectile: 200 (left), 500 (middle) and 1000 (right) AMeV. The behaviour of the evaporation residues production yields of with the excitation energy can be observed. For lower energies, the residues are near the projectiles. As the energy increases, the residues approach the evaporation corridor. For high energies, the reaction products lie in this evaporation corridor, but reach lighter fragments.

When determining the proton-to-neutron ratio of the final residues in fragmentation reactions, the isospin and excitation energy of the prefragment must be taken into account. The abrasion process described previously determines only the number of nucleons abraded from the initial nucleus; it does not specify the number of protons or neutrons abraded. The most used approximation is the hyper-geometrical model [Hüf75], where there is no correlation at all between the nucleons during the abrasion. In this model, the statistical chance of any removed nucleon to be a proton or a neutron is determined by the neutron-to-proton ratio of the initial nucleus in the following way:

$$\sigma(N_p - n, Z_p - z) = \frac{\binom{Z_p}{z} \binom{N_p}{n}}{\binom{A_p}{a}} \sigma(A_p - a) \quad (1.5)$$

where Z_p , N_p and A_p are the numbers of protons, neutrons and nucleons from the initial projectile, and n , z and a are the corresponding quantities of the particles removed from the projectile during the abrasion. $\sigma(A_p - a)$ is the cross section to abrade a nucleons, depending on the impact parameter.

Based on these considerations, the fragmentation reactions leading to the most neutron-rich residues are those where proton removal plays a predominant role, producing cold prefragments with a low probability of neutron evaporation (*cold fragmentation* [Ben99]). The mean excitation energy of the prefragment per abraded nucleon is 27 MeV, but there is a non-zero probability of obtaining an excitation energy below the particle evaporation threshold [Gai91].

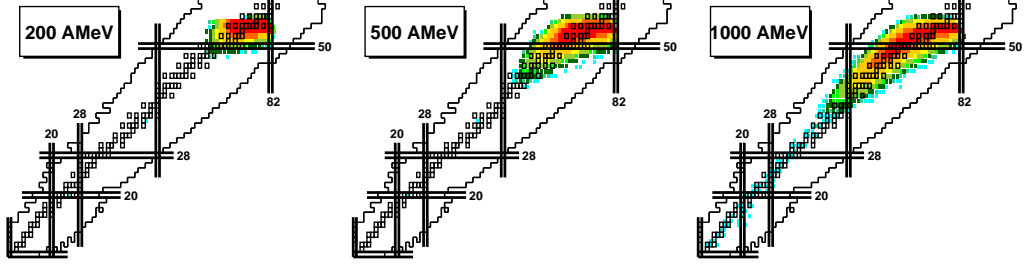


Figure 1.4: Calculated production yields with INCL4+ABLA on top of the chart of nuclei for the reaction $^{136}\text{Xe}+^1\text{H}$ for different energies of the projectile. The color scale represents the different production yields. See text for details.

Fission The fission is the splitting of the nucleus in two fragments. This process can occur spontaneously for certain nuclei or be induced in nuclear reactions. The excitation energy gained by the nucleus is transformed into collective motion that provokes the deformation of this nucleus. While the nucleus deforms, the surface energy increases, opposing the deformation. At the same time, the separation of the charges reduces the Coulomb term, favouring the elongation. The competition of these two effects creates a potential barrier in the deformation coordinate. The top of the barrier, is a 'point of no return'. Beyond this point, the system separates in two fragments.

A statistical description of the fission process was given by Bohr and Wheeler [Boh39], but presents a difference with the evaporation model: instead of considering the level density on the final state, the width of the process depends on the level density at the saddle point (*transition state method*).

$$\Gamma_f = \frac{1}{2\pi} \frac{1}{\rho(E_i, J_i)} \int_0^{E_i - B_f} \rho_{sad}(E_i - B_f - u, J_i) du \quad (1.6)$$

where *sad* refers to the saddle point and B_f is the fission barrier.

This model gives us the probability of fission occurring, but it does not take into account the mass asymmetry degree of freedom or the dynamical effects that appear at high energy [Kra40]. Consequently, it provides no information on the mass or charge distribution of the fragments produced in the fission process. Moretto [Mor75], proposed the use of a potential in the fission barrier which depends on the mass asymmetry $B_f(q) = B_0 + \alpha q^2$, where q is the mass asymmetry coordinate. Benlliure *et al.* [Ben98] improved this formalism by introducing a more realistic description of the mass asymmetry dependence of the potential of the fission barrier at the saddle

point, based on a semiempirical description of the shell effects observed in the experimental results and the Brosa model [Bro90]. The proposed potential has three main components as a function of the neutron number at the saddle point. The first one is the symmetric component (V_{mac}) described by a parabolic function as defined by the liquid drop model. This parabola is modulated by two neutron shells located at $N = 82$ and $N = 88$ in the nascent fission fragments. The potential is therefore the sum of five contributions. The parameters for each component of the potential are taken from experimental results. The probability of a given splitting is obtained by the statistical weight of transition states above the mass-asymmetry potential.

The dynamical effects first described by Kramers must also be considered to describe the fission width. Kramers showed that the fission widths are related with the statistical ones obtained using the Bohr and Wheeler model with the following equation.

$$\Gamma_f = K \cdot \Gamma^{BW} \quad (1.7)$$

where K is the Kramers factor defined as

$$K = \left\{ \left[1 + \left(\frac{\beta}{2\omega_0} \right)^2 - \frac{\beta}{2\omega_0} \right] \right\} \quad (1.8)$$

In this equation β is the reduced dissipation coefficient and ω_0 represents the frequency of the harmonic oscillator describing the inverted potential at the fission barrier.

The residues produced in fission reactions allow us to populate the medium-mass neutron-rich region of the nuclear chart, but the excitation energy at which the fission takes place must be taken into account. Fission at low excitation energy, produces an asymmetric charge distribution. The fission residues present shell effects, enhancing the production of fragments with $N=82$ and $N=88$ along with their corresponding charge and mass partners. Fission at higher excitation energies produces a more symmetric distribution whose width increases with temperature [Arm70]. Figure 1.5 shows the calculated yields for fission residues of ^{238}U at 1 MeV (left panel) and 100 MeV (right panel) excitation energy on top of the nuclide chart. Here we can see the effects already described. The distribution of the fragments at higher excitation energies is more symmetric and wider compared to the results obtained at lower excitation energies. Shell effects can also be observed at low energies. It should be pointed out that results shown in right panel of Figure 1.5 are normally not observed. In an experiment, evaporation residues of ^{238}U will also fission, therefore the real yields will be a mixture of the fission residues of different nuclei at different excitation energies.

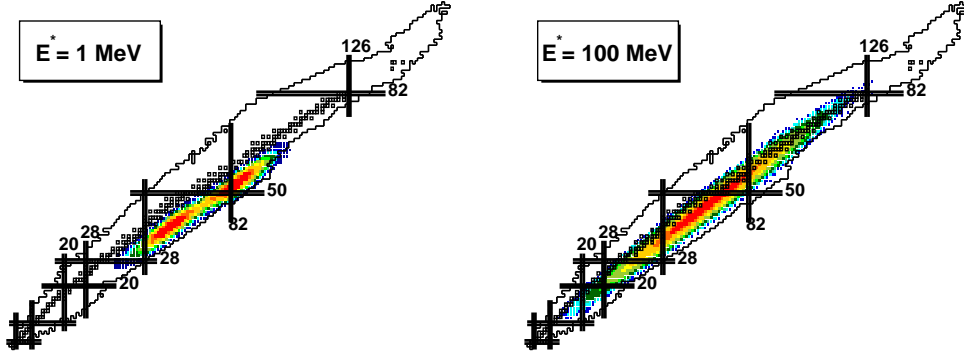


Figure 1.5: Calculated production yields in ^{238}U fission on top of the chart of nuclei for different excitation energies. The color scale represents the different production yields. See text for details.

1.2.5. Present limits of the nuclide chart

As mentioned in Section 1.1, the limits of existence in the nuclei are defined by the proton and neutron driplines and the maximum charge and mass a nucleus can reach. The proton dripline is closer to the stability valley than the neutron dripline, due to the Coulomb repulsion. Over the years, several different experimental techniques for reaching the driplines were developed. Reaching the limits of existence is easier for the lightest nuclei, where the driplines are close to the valley of stability. The proton dripline up to $Z=11$ (^{20}Na) and the neutron dripline up to $N=9$ (^{14}B) had already been reached in the 1960's. Single or multiple particle transfer reactions with stable targets and beams as well as spallation reactions were used to reach the driplines. The development of projectile fragmentation made it possible to explore of the limits of the existence towards larger proton and neutron numbers.

In proton dripline, for elements in the region with atomic numbers between $Z=20$ and $Z=50$, projectile fragmentation is the only reaction mechanism for producing nuclei at and beyond the proton dripline [Sch94; Lew95]. For heavier elements, the most appropriate mechanism is heavy ion fusion-evaporation reactions [Mac65]. Today, the proton dripline has been reached for all odd nuclei up to $Z=83$ [Woo97]. It has been reached only up to nickel ($Z=28$) for proton-rich even- Z nuclei.

The neutron dripline has only been reached for very light isotopes, up to $Z=13$ [Bau07], using projectile fragmentation. Different methods have been used to produce neutron-rich nuclei, depending on the region of the chart of nuclides. For lighter elements, the dripline was initially explored with deep

inelastic reactions, projectile fragmentation and spallation reactions. However the medium-mass neutron-rich region has to be populated by different mechanisms. Fission has proven itself to be a powerful technique for the production of medium-mass neutron-rich nuclei [Ber97] and cold fragmentation has produced heavier neutron-rich nuclei. Eighty new neutron-rich isotopes of elements between tantalum and actinium were produced from the cold fragmentation of ^{197}Au , ^{208}Pb , and ^{238}U on Be at relativistic energies [Ben99; AP09; Ben10].

As the intensities of the radioactive ion beams have increased, it has become feasible to use them for secondary reactions. For example, neutron-rich fragments produced in a fragmentation reaction could be used for secondary fragmentation [Luk09].

Regarding the limits of superheavy elements, $Z=118$ is the element with the highest number of protons so far, as mentioned in Section 1.1. This nucleus was produced in fusion evaporation reactions using ^{48}Ca as a projectile and a ^{249}Cf radioactive target [Oga06].

1.3. Techniques for the production of exotic nuclei

In general, two complementary methods exist for producing good quality beams of exotic nuclei: the in-flight separation technique and the Isotope Separation On-Line (ISOL). Figure 1.6 shows the main aspects of both methods. A driver accelerator or reactor provides the particles for inducing nuclear reactions in a production target. In the in-flight method, relativistic projectiles are fragmented and their recoil residues used as secondary beams. The ISOL method takes advantage of the spallation reactions induced by intense proton beams and thick targets.

1.3.1. In-flight

The in-flight method is based on the fragmentation or fission of energetic heavy-ion projectiles, followed by the in-flight separation of the fragments produced. Typical energies of secondary beams presently range from 30 AMeV to 1AGeV. The technique is based on the kinematic (forward) focusing present in the peripheral nuclear reactions that occurs when heavy projectiles at relatively high incident energies impinge onto thin targets. The reaction products recoil out from the production target. The exotic nuclei must then be separated from the primary beam and from the other reaction products by some combination of magnetic and electrostatic elements.

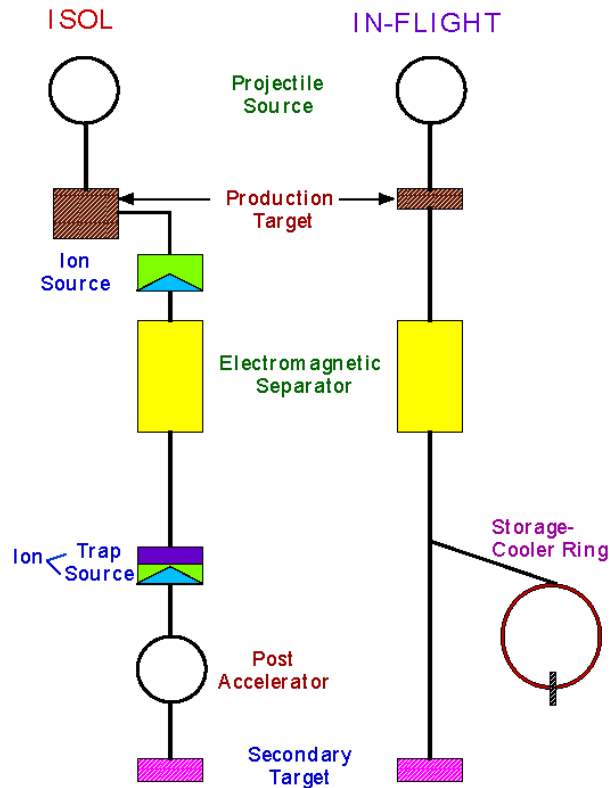


Figure 1.6: Schematic representation of the ISOL (left) and in-flight (right) techniques for the production of radioactive ion beams (RIBs), showing the different stages of each.

Particle identification of fast ions is relatively simple, and the contaminant level can be checked on-line. One of the main features of this method is that the process is independent of the chemical properties, or the half-life of the isotopes of interest. The limitation of the half-life is only given by the flight time of the ions through the separator, which is generally less than $1 \mu\text{s}$. With the appropriate ion optics, separation efficiencies are close to 100% for fragmentation reactions.

1.3.2. Isotopic Separation On-Line (ISOL)

The ISOL technique is based on the production of radioactive species by spallation, and by photon- or neutron-induced fission in a thick target at rest. The isotopes produced are then extracted from the target-catcher material and ionized to a certain charge state in an ion source. After ionization, the species are mass analyzed using a magnetic spectrometer and subsequently

post-accelerated to the required energy.

The main elements of the ISOL technique are shown in the left panel of Figure 1.6. The accelerator driver produces a primary beam of light ions at high energies and impinges onto a thick production target-converter. Once the exotic nuclei are produced in a nuclear reaction, the radioactive nuclei of interest are extracted from the target by thermal diffusion and then transported to the ion source. However, diffusion in the target material depends on the chemical properties of the reaction products. Moreover, the diffusion takes some time, thus the short-lived isotopes of some elements have very low surface release efficiency. After the extraction from the target, the selected elements have to be ionized for a later magnetic separation. Depending on the requirements, several different ionization mechanisms are used. In general, single-charged positive or negative ions are produced. Different mechanisms can be used for the ionization of the selected fragment: electron impact ionization, surface ionization and laser ionization.

Electron Impact Ionization This ionization mechanism is used in ECR and EBIS sources for isotopes of elements with ionization potentials (W_i) higher than 7 eV and for the creation of multiple-charged ions. The atoms of the ions are bombarded by energetic electrons and lose one or more of their own outer electrons. This method is not very chemical selective, due to the unselective nature of the ionization process.

Surface ionization This second ionization mechanism is based on surface ionization. When an atom interacts with a heated surface, it can lose or gain an electron before leaving the surface. This technique is used for elements with very low ionization potentials ($W_i < 7$ eV) and with electron affinities larger than 1.5 eV, to generate positive and negative ions, respectively. The surface ionization method is extremely selective when the elements produced in the same reactions present different ionization potentials.

Laser ionization During this ionization process, atoms are stepwise excited by laser photons, leading finally to the continuum, to auto-ionizing states, or to states close to the continuum. This ionization process consists on two or three steps, and because of the resonant nature of most of them, laser ionization is very efficient and selective.

After the ions are created in the ion source, they are extracted and accelerated in a DC electrical field. The ions are then transported to an analyzing magnet where they are mass separated due to the different curvatures of the different masses in a magnetic field.

The beam is then 'cooled' in order to improve its ion optical properties. The cooling consists on the reduction of the axial and radial momentum, or energy spread of the beam. Beams can be cooled by Penning traps or radio frequency coolers. Buffer gases such as helium or argon are introduced in order to reduce the energy of the ion beam from collisions between the gas and the ions.

In order to obtain a simpler and more efficient post-acceleration of the radioactive ion beam, high ionization charge states of the beam must be produced. This is done with a charge-state breeder. ECR and EBIS ion sources are used. As mentioned before, the ionization is based on the collisions of the energetic electrons with the ions.

The highly charged ion beam from the breeder or the beam itself, can be injected into an accelerator (linear accelerators, tandems or cyclotrons) to increase the energy of the RIB.

1.3.3. Hybrid techniques

The possibility of combining both methods has been investigated as a way of overcoming their separate limitations.

Gas catchers

A new approach to the production of low-energy radioactive beams involves the stopping of fast beams (produced by fragmentation, in-flight fission or fusion-evaporation reactions) in a large gas catcher where the reaction products are thermalized in high-purity helium and extracted as singly charged ions for post-acceleration. This removes the limitation present in the standard ISOL technique for species that are difficult to extract from the target/ion source assembly.

Two-step reaction scenario

This approach is the complete opposite of the gas catcher. The idea is to produce very neutron-rich nuclei from the fragmentation of post-accelerated neutron-rich reaction products. This combined technique also overcomes the limitation of the impossibility of the extraction of the refractory elements³ produced in fission from the ISOL targets.

³a refractory elements is a chemical element that vaporizes (that is, boils) at high temperatures or condenses from a gas at high temperatures.

1.4. Existing RIB facilities

In this section, the existing RIB facilities will be described. We will divide this section in the two techniques described previously, namely, ISOL and in-flight.

1.4.1. ISOL

At different places worldwide ISOL facilities are operational. Here we will give an overview of the existing facilities, with a brief description of the capabilities of each facility.

CRC at Louvain-La-Neuve, Belgium

This was one of the first facilities where ISOL-based radioactive beams were produced by means of the radioactive ion beam (RIB) project in 1989, within the radioactive ion beam (RIB) project. CRC combines two cyclotrons with a target-ion source system. The radioactive isotopes are produced with a 30 MeV proton beam with intensities of 200 μA . Direct reactions on C, Li and F targets are used to produce intense beams of light radioactive isotopes which are then post-accelerated to energies between 0.2 and 10 AMeV [CRC].

HRIBF at Oak-Ridge, USA

The HRIBF uses a cyclotron as a driver accelerator, with intensities of 13 μA (for protons and deuterons at 44 MeV) and 3 μA (for α particles at 85 MeV). Both direct reactions and fission are used. The isotopes are then post-accelerated by a 25 MV tandem accelerator. Energies up to 5 AMeV are reached for masses below 100 [RIB].

ISAC facilities at TRIUMF, Canada

At the ISAC facility, a primary proton synchrotron accelerator delivers 500 MeV beams, with intensities up to 100 μA . The radioactive isotopes are produced in spallation and fragmentation reactions. Thick targets are used and the 1+ ions produced are accelerated (by a linear accelerator) up to 1.5 AMeV. The ISAC-II is a superconducting LINAC which accelerates ions for masses up to 150 at 6.5 AMeV [TRI].

REX-ISOLDE at CERN, Switzerland

At CERN, the proton-synchrotron booster delivers 1.4 GeV proton beams with an intensity of $2 \mu\text{A}$. Target spallation, fragmentation and fission produce a wide spectrum of radioactive ion beams. A linear accelerator post-accelerates the isotopes produced up to 3.1 AMeV [ISO].

SPIRAL at GANIL, France

The SPIRAL facility at GANIL accelerates heavy ions at intermediate energies (C up to 95 AMeV with an intensity of $(10^{12}$ ions/s) and U up to 24 AMeV (10^{10} ions/s), and sends them to a carbon target to produce radioactive isotopes from fragmentation reactions. Post-acceleration up to 25 AMeV is done by a cyclotron [GAN].

EXCYT at INFN-LNS, Italy

The EXCYT facility at INFN-LNS, is based on a K-800 Superconducting Cyclotron that injects stable heavy-ion beams (up to 80 AMeV, $1 \mu\text{A}$) into a target-ion source assembly (TIS) to produce the required nuclear species. A 15 MV Tandem is used for post-accelerating the radioactive beams [EXC].

1.4.2. IN-FLIGHT**NSCL at MSU, USA**

Radioactive ions beams are created using the in-flight method at the National Superconducting Cyclotron Laboratory at Michigan State University. The driver accelerators are two superconducting cyclotrons that can accelerate any element up to uranium. The energies achieved range from 20 AMeV to 200 AMeV and the reaction products are separated and identified with the A1900 magnetic spectrometer. The A1900 is a projectile fragment separator composed of 40 large-diameter superconducting multipole magnets and four 45° dipoles with a maximum magnetic rigidity of 6 Tm. The A1900 has a solid angle of 8 msr and a momentum acceptance of 5.5% [NSC].

LISE at GANIL, France

The LISE spectrometer installed at GANIL is used to produce secondary beams using the in-flight technique. It consists of a set of 10 quadrupoles and two 45° dipoles with a total momentum acceptance of 5%. The maximum rigidity is 3.2 Tm and the angular acceptance is 1 msr [Ann87].

FRS at GSI, Germany

At the GSI facility, the SIS18 synchrotron delivers beams of heavy ions up to uranium at energies reaching 1 AGeV. Both fragmentation and fission are used for the production of radioactive ion beams. The reaction products are separated and identified using the FRS spectrometer. The FRS is composed of a set of 20 focusing quadrupoles and four 30° dipoles with a maximum rigidity of 18 Tm. The angular acceptance of the FRS is 15 mrad in both directions and the momentum acceptance is 3 % [Gei92].

1.5. Future Facilities

1.5.1. RIBF at RIKEN, Japan

The Radioactive Ion Beam Factory, at RIKEN, is an accelerator complex that consists on a set of different accelerators with capabilities to accelerate ion beams of heavy ions up to uranium. The maximum beam energy available is 400 AMeV for light elements and 350 AMeV for uranium. Radioactive ion beams are produced via fragmentation and fission. The reaction products are separated and identified with the bigRIPs magnetic spectrometer. The two main features of the BigRIPS are its large acceptances and a two-stage separator scheme. The large acceptances are achieved by the use of superconducting quadrupoles with large apertures. The two-stage separator scheme makes it possible to deliver tagged RI beams. In the first stage of the BigRIPS separator RI beams are produced and separated. In the second stage RI-beam species are identified in an event-by-event mode. The first stage, from the production target to the F2 focus, comprises a two-bend achromatic spectrometer, consisting of four superconducting quadrupole triplets (STQs) and dipoles with a bending angle of 30°. The second is a four-bend achromatic spectrometer, consisting of eight STQs and four dipoles with a bending angle of 30°. The maximum rigidity is 6 Tm. The BigRIPS has an angular acceptance of 100 mrad (vertical) and 80 mrad (horizontal), with a momentum acceptance of 6 % [RIK].

1.5.2. SPIRAL2

The SPIRAL2 project is based on a multi-beam driver that will allow RIB production by both ISOL and low-energy in-flight techniques. A superconducting light/heavy-ion LINAC with an acceleration potential of about 40 MV, capable of accelerating 5 mA deuterons up to 40 MeV and 1 mA heavy ions up to 14.5 AMeV is used to bombard both thick and thin targets.

These beams could be used for the production of intense RIBs by several reaction mechanisms (fusion, fission, transfer, etc.). The production of high intensity, neutron-rich nuclei RIBs will be based on the fission of a uranium target induced by neutrons, obtained from a deuteron beam impinging on a graphite converter (up to 10^{14} fissions/s) or by a direct irradiation with a deuteron, ^3He or ^4He beam.

Post-acceleration of RIBs in the SPIRAL2 project is assured by the existing CIME cyclotron, which is well adapted for the separation and acceleration of ions in the energy range from about 3 to 10 AMeV for masses $A \sim 100-150$. SPIRAL2 beams, both before and after acceleration, can be used in the present experimental area of GANIL [SPI].

1.5.3. SPES

The SPES project is concentrating on the production of neutron-rich radioactive nuclei with masses in the 80-160 range, by uranium fission at a rate of 10^{13} fission/s. The Rare Ion Beam (also RIB) will be produced by ISOL technique using the proton induced fission on a UC_x target. The proton driver is a cyclotron with variable energy (15-70 MeV) and a maximum current of 0.750 mA upgradeable to 1.5 mA. The RIBs will be post-accelerated with a superconducting LINAC up to energies of 11 AMeV for masses around 130 [SPE].

1.5.4. HIE-ISOLDE

The HIE-ISOLDE is an upgrade of the existing REX-ISOLDE facility that will greatly expand the physics programme there. The three major elements of the HIE-ISOLDE project are higher energies, improvements in beam quality and flexibility, and higher beam intensities. This requires developments in radioisotope selection and improvements in charge-breeding and target-ion source development, as well as construction of the LINAC4, the new injector for the PS Booster. The most significant improvement will come from replacing most of the existing REX accelerating structure by a superconducting (SC) linear accelerator with a maximum energy of 10 MeV/u. This would allow all ISOLDE beams to be accelerated to energies well below and significantly above the Coulomb barrier, facilitating a broad programme of nuclear structure and nuclear astrophysics research different classes of nuclear reactions [HIE].

1.5.5. FAIR

The FAIR facility is the next generation in-flight facility in Europe [FAI]. In this facility, two synchrotron accelerators, will deliver heavy ion beams up to 1.5 AGeV for the production of exotic nuclei from fission and fragmentation reactions. The produced nuclei will be separated and identified using the Super-FRS magnetic spectrometer. The use of a pre-separator stage and two profiled degraders, will make it possible to obtain very intense radioactive beams of many species. More information on the FAIR facility can be found in Chapter 5.

1.5.6. EURISOL

The European Isotope Separator On-Line (EURISOL) is an ISOL facility that will be developed in Europe. A proton accelerator will be used for the primary beam to induce spallation, fragmentation and fission reactions. Two target options are being considered: direct target irradiation with maximum intensities of 100 μA and irradiation of a proton-neutron converter with 5 mA beams. A linear accelerator will deliver a beam energy of up to 150 AMeV for the later fragmentation of secondary beams. More information on this facility will be given in Chapter 5.

1.5.7. FRIB

The Facility for Rare Isotope Beams (FRIB), is a next generation facility proposed in the USA. Here, a primary heavy-ion accelerator capable of delivering intense ion beams up to uranium at 400 AMeV will be used for fission and fragmentation reactions. Both, in-flight and ISOL system techniques will be used. Apart from the conventional target-ion source system, a gas catcher program is proposed, whereby the beams delivered by a fragment separator will be stopped in a large gas cell for thermalization. The post-accelerator will bring the secondary beam up to 12 AMeV [FRI].

Chapter 2

Experimental technique

To investigate the production of medium-mass neutron rich nuclei, two different experiments were performed in order to determine which reaction mechanism enhances this production. The isotopic production cross sections of fission and fragmentation residues were measured using *inverse kinematics* at relativistic energies. With this technique, the projectile fragments produced in the reaction are emitted in forward direction. This fact allows us to analyze them with an in-flight magnetic spectrometer. The experiments took place at the GSI facility in Darmstadt, Germany. At present time, GSI is the only facility in the world where it is possible to accelerate ^{238}U ions up to 1 AGeV with intensities of 10^8 ions/s. Forward emitted reaction products are identified with the FRagment Separator (FRS) magnetic spectrometer. Radioactive losses are minimized because of the short time needed for the isotopic identification (less than 300 ns).

This chapter includes a brief description of the experimental facilities and the detection setup used in both experiments. Finally, the identification procedure is described. Specific details related to the experimental technique or the identification method different than those described in this chapter will be presented in the chapters corresponding to each experiment.

2.1. The experimental facilities

2.1.1. The GSI accelerator system

The GSI accelerator system is composed of several ion sources and two consecutive acceleration stages (see Figure 2.1). In our experiments the ^{238}U ions produced in the MEVVA source were injected into the first acceleration stage. This consists of a 120-meter long linear accelerator (UNILAC) divided

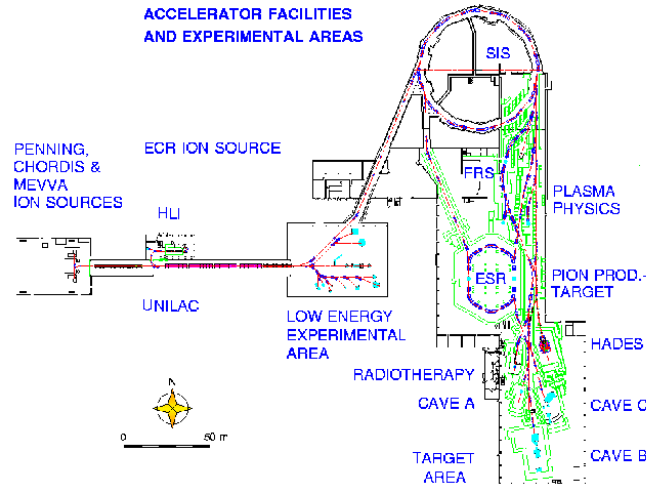


Figure 2.1: Schematic representation of the GSI facilities. We can observe the two acceleration stages (UNILAC and SIS) and the experimental areas, in particular the Fragment Separator (FRS).

into two sections. The first is a combination of RFQ (Radio Frequency Quadrupole) and IH (Interdigital H-Mode) structures operated at 36 MHz. The accelerated ions are then stripped in a transverse nitrogen gas jet. At the end of the process, the uranium ions have an energy of around 1.4 AMeV, and a charge state of 28+. The beam is then injected in the second section, an Alvarez type accelerator whose operation frequency is 108 MHz. Here, the ions are accelerated up to 11.4 AMeV and then injected into the SIS synchrotron. Before entering the synchrotron, the beam passes through a carbon stripper to obtain the 73+ charge state.

The SIS synchrotron has a circumference of 216 m and a maximum bending power of 18 Tm. It consists of a set of 12 identical cells placed along the circumference. Each of them is composed of a pair of dipoles, a triplet of quadrupoles for focusing and a set of sextupoles to correct chromatic aberrations. The maximum energy of $^{238}\text{U}^{73+}$, limited by the bending power, is 1 AGeV. The slow extraction mode used in these experiments produces a low-emittance beam with a spill duration of few seconds. It also provides a very low momentum spread ($\delta p = \Delta p/p < 10^{-3}$).

The acceleration system used at GSI also supplies the very high intensities required to investigate the most exotic reaction products. In these experiments, the beam reached intensities of 10^9 ions/spill. The pulsed beam structure is shown in Figure 2.2, whose duration was 6 s, with a cycle of 20

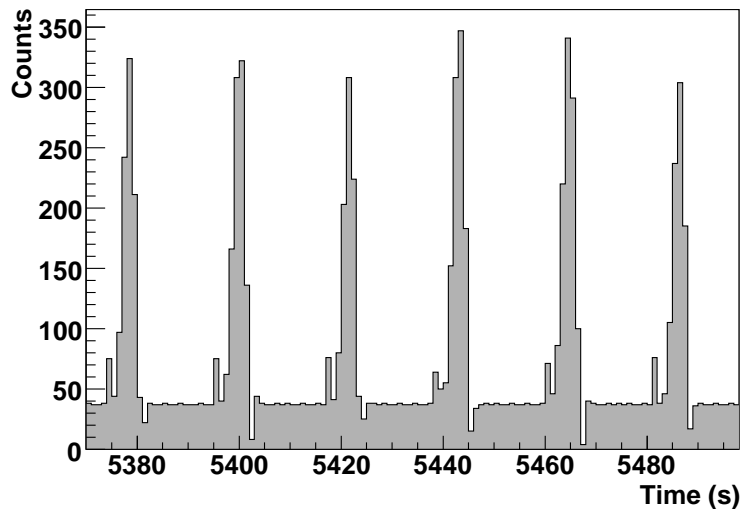


Figure 2.2: Beam profile as a function of time. Here we see the spill structure of the beam, with a 20 s cycle and a 6 s spill duration.

seconds. The beam was monitored during the entire experiment in order to normalize the yields of the reaction products.

2.1.2. The beam monitor

The *SEcondary Electron TRANsmiission Monitor* (SEETRAM) [Jun96] is used as a beam monitor to determine the beam intensity which impinges on the target. The SEETRAM consists of three 10 μm titanium foils. The two outer foils are connected to an +80V voltage and the inner one is grounded. Secondary electrons emitted by the passage of relativistic ions through the inner foil are driven to the outer foils. The resulting positive current in the inner foil is measured with a current digitizer. The digital output signal (SEETRAM units) is recorded during the entire experiment with a scaler.

The dark current present in this detector during the beam pauses produces a nearly constant background signal that has to be subtracted in order to determine the real beam intensity (Figure 2.2).

The SEETRAM counts must be calibrated to beam particles [Jur02]. In order to do so, the SEETRAM signal is compared to a reference plastic scintillator detector at low beam intensities (Figure 2.3). Linearity of SEETRAM for high intensities was verified by comparing the SEETRAM current with the beam current in the synchrotron [Jur02]. The SEETRAM range must also be adjusted depending to the different beam intensities used during the

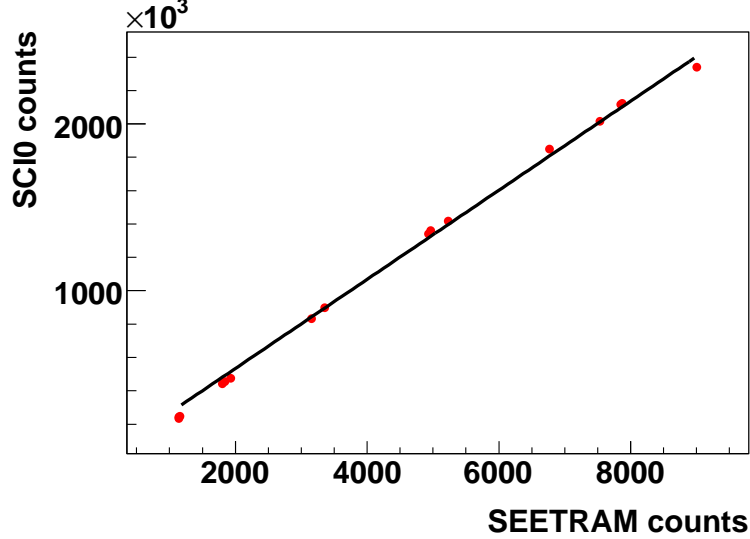


Figure 2.3: Integrated current per spill measured with the SEETRAM detector versus the counting rate given by the plastic scintillator in the non-saturation region. The solid line represents the linear fit restricted to this region.

experiments in order to fit the production to the acquisition rate. The range factor, *sensitivity*, can be selected between 10^{-4} and 10^{-10} . The relation between the SEETRAM counts and the number of beam particles is given by:

$$N_{\text{beam}} = (N_{\text{SEETRAM}} - N_{\text{background}}) \cdot f \cdot 10^{10} \cdot \text{sensitivity} \quad (2.1)$$

where f is the calibration factor, which depends on the projectile type and energy. The calibration factor measured in our experiment was 267 ± 2 ions/SEETRAM, obtained from the slope of the linear fit shown in Fig. 2.3.

2.1.3. The targets

Several targets were used in the experiment to investigate fission at different excitation energies and the fragmentation of fission residues on Be. Target thicknesses are shown in Table 2.1. Most of the targets used were placed in front of the spectrometer during different experimental runs in order to induce fission of the ^{238}U beam. The 2.5 g/cm^2 Be target was placed at the intermediate focal plane as a secondary reaction target in the runs in which fragmentation of fission residues was investigated.

Table 2.1 also shows the reaction probability of ^{238}U in each target, except for the 2.5 g Be target, where the probability has been calculated for a ^{132}Sn projectile. The selected thickness values are a compromise between

| Target | Thickness (mg/cm ²) | React. Prob. (%) |
|-----------------|---------------------------------|-------------------|
| Be | 1036 ± 1 | 21.1 |
| Pb | 649 ± 5 | 1.5 |
| Pb | 1534 ± 7 | 3.48 |
| Be ^a | 2591 ± 7 | 35.2 ^b |

^aPlaced at intermediate focal plane as a secondary reaction target

^bReaction probability for ¹³²Sn at 950 AMeV

Table 2.1: Thicknesses of the different targets used in this study.

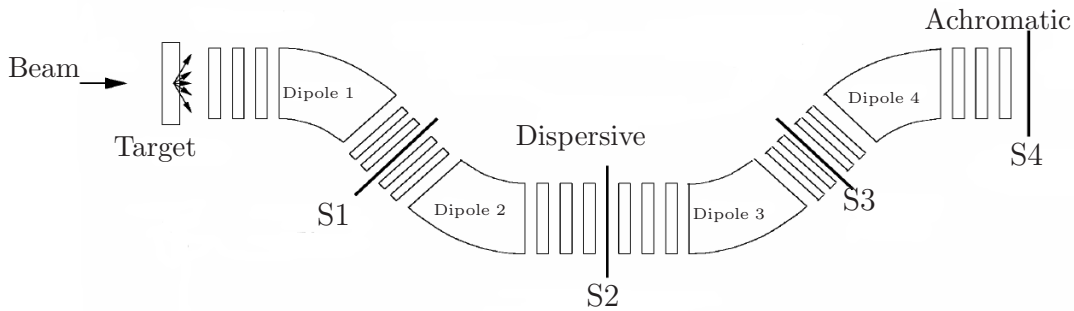


Figure 2.4: Schematic layout of the FRS. Showing dipoles and quadrupoles. This magnetic spectrometer has four focal planes, labeled as S1, S2, S3 and S4. S2 and S4 are the dispersive and achromatic focal planes, respectively.

the production rates and secondary reaction probability, while keeping the energy range of the residues.

2.1.4. The fragment separator (FRS)

The FRS is an achromatic zero-degree magnetic spectrometer. It consists of four independent identical stages with a focal plane between each pair of dipoles. The whole system is symmetrical to the intermediate focal plane. Each stage is composed of one H-type 30° dipole, five quadrupoles, and a set of sextupoles. Two of the quadrupoles are placed in front of the dipole to enlarge the horizontal emittance component, while decreasing the vertical one (see Fig.2.4). The three other quadrupoles are placed behind the dipole

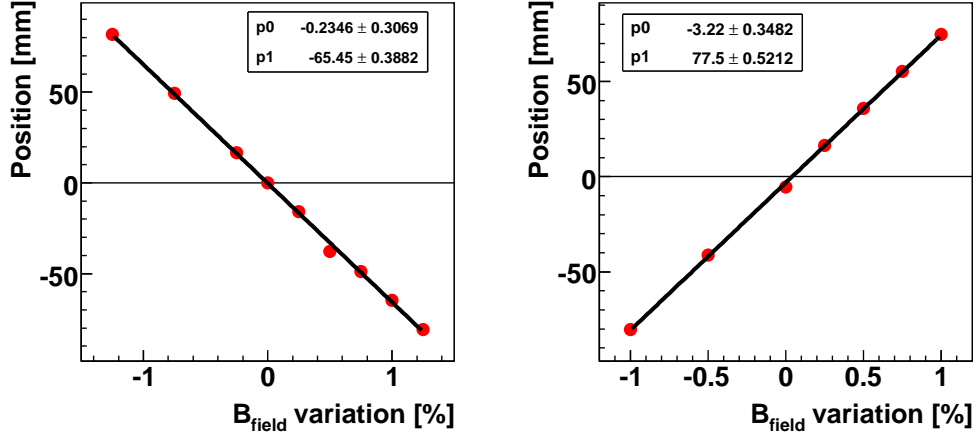


Figure 2.5: Position of the ^{132}Xe beam versus the variation of the magnetic field in the dipole magnets for dispersion calibration in the first (left panel) and second (right panel) sections of the FRS.

and provide the correct optics in the focal planes. The sextupoles are used for higher-order optical corrections.

The FRS can be operated in three different modes, achromatic, mono-energetic, and *energy-loss* mode. In the achromatic mode, point-to-point images are obtained between the entrance and the final image planes along the 72 m flight path. Achromaticity is achieved because the dispersion¹ of the second half of the spectrometer ($D_{24} = 7.75$ cm/%) compensates the dispersion in the first half ($D_{02} = 6.54$ cm/%). The magnification of the system is then $V = D_{24}/D_{02} = 1.185$. These values were calibrated during the experiment by measuring the trajectory of a ^{132}Xe beam at 1200 AMeV for different values of the magnetic fields in the dipoles (see Fig. 2.5).

The FRS has a maximum angular acceptance of ± 15 mrad for its central trajectory, and a momentum acceptance of ± 1.5 %. These values are given by the physical transverse aperture of the magnetic elements and their ion-optical properties. The maximum magnetic rigidity is 18 Tm, determined by the radius of the dipole magnets (~ 11 m) and the maximum magnetic field (1.6 T). The magnetic fields were measured by Hall probes with a resolution of 10^{-4} .

The main feature of the FRS is its high *resolving power*, $R=1500$, for a beam spot of 2.7 mm (FWHM) and an emittance of 20π mm \times mrad. For a

¹Dispersion relates the change in position due to a difference in momentum. It is normally given in cm/%: a variation in momentum of a certain percentage, produces a variation in the position of some cm.

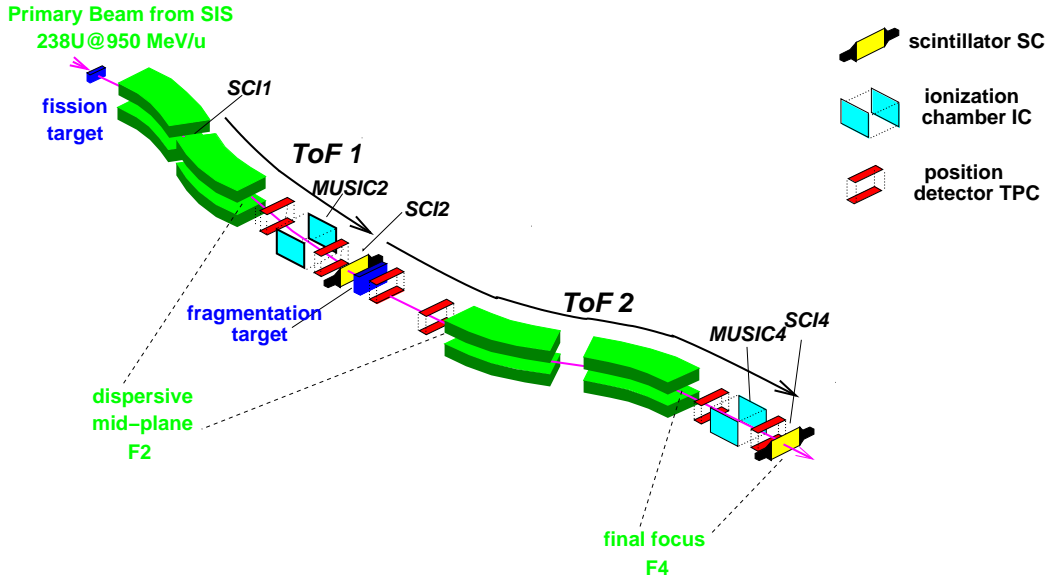


Figure 2.6: Schematic view of the experimental setup, used in these experiments, showing the position of the target and main detectors.

more detailed description of the FRS, see ref. [Gei92].

2.2. The detection equipment

Figure 2.6 shows the FRS and the detectors used in these experiments. The ^{238}U primary beam, monitored with the SEETRAM, impinges on the beryllium or lead target at 950 AMeV. The Lorentz boost causes the fission fragments produced to be forward-focused and they enter the FRS. Time projection chambers (TPC) were placed at the intermediate and final focal planes to track the reaction products, in order to determine the horizontal and vertical position of each fragment. The three plastic scintillators $SC1$, $SC2$ and $SC4$, placed at the S1, S2 and S4 areas allow the measurement of the time-of-flight of the transmitted nuclei from the first (S1) to intermediate focal plane (S2) and from S2 to the final focal plane (S4), respectively. The ionization chambers (MUSIC) placed in both focal planes were used to determine the energy loss in their gas volume for each of the fragments. Multiwire chambers were also used to center the beam during the calibration runs.

2.2.1. The multiwire chambers

A set of multiwire proportional chambers (MW)[Ste91] was used to calibrate the spectrometer. For this purpose, a ^{132}Xe beam at 1200 AMeV was used. This beam energy was selected in order to obtain a magnetic rigidity value similar to that of the fission residues to be studied. Calibration is indispensable for ensuring well-defined ion-optical conditions during the experiment. The MWs were placed in the image focal planes between the dipoles. The calibration is done by passing the ^{132}Xe beam through the spectrometer and registering the position on the focal planes with the MWs. When the beam is centered, the magnetic fields measured times the curvature radii in the dipoles correspond to the magnetic rigidities of the beam in the different stages. Thus we can determine the rigidity that corresponds to the central trajectory of the spectrometer. The MWs were not inserted while the reaction products were being measured, so that the achromaticity of the spectrometer would not be affected.

The MW detectors used at FRS consist of five parallel wire planes connected to different high voltages. The central plane is made of 20 μm tungsten wires placed 2 mm apart. The other planes are made of 50 μm wires, with 1 mm pitch. The first and third planes are the x and y plane respectively, thus the wires are perpendicular to the corresponding axis. The chamber is filled with a mixture of Ar, CO_2 and alcohol at atmospheric pressure. The MW signals are read with a CAEN V775 TDC.

2.2.2. The time projection chambers

Time projection chambers (TPCs)[Hli98] are ionization detectors used for tracking. When a particle passes through the detector, it creates electron-ion pairs along its track. The electrons drift towards the anodes because of the uniform electric field. The drift time provides information about the y coordinate. The electrons accelerate as they approach the anode, ionizing more atoms of the gas and producing a negative electric signal. This signal induces a positive signal in the delay lines, producing a pulse. The time needed to collect the signal in both sides of the delay line gives us information about the x position.

Six TPCs were used in these experiments, four at the intermediate focal plane (S2) and two at the final focal plane (S4). The gas used was argon and windows were made of kapton foils. Two delay lines were used to obtain two independent measurements of the x position. Each one was connected to a pair of anodes (see Fig. 2.7). A CAEN V775 TDC operating in *common-stop* mode was used for the readout of the drift times. These detectors provided

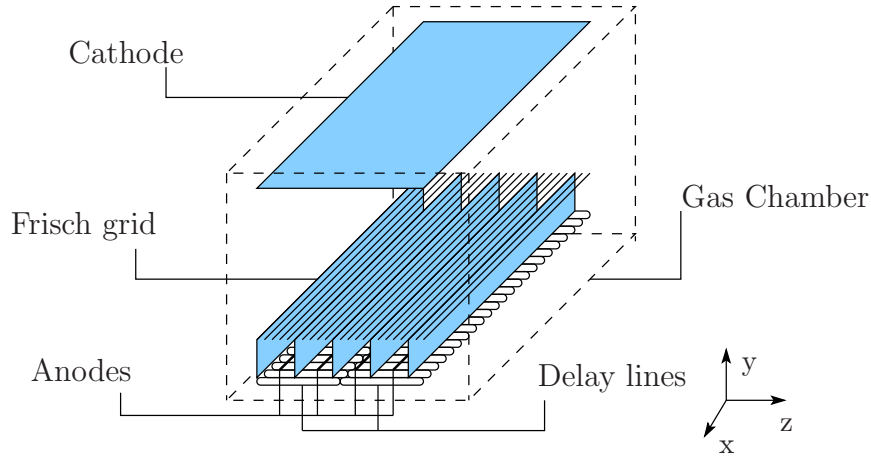


Figure 2.7: Schematic view of the time projection chambers (TPC). Each detector had four different anodes connected in pairs to two different delay lines.

an excellent position resolution (better than 0.5 mm).

The TPCs were calibrated with the ^{132}Xe beam used for the FRS calibration. This calibration was done by placing a scintillator mask in front of the TPCs. The defocused beam covered the mask and the coincidences between the scintillators and the TPCs produced the pattern shown in Figure 2.8. Absolute calibration was obtained by matching the positions of the peaks produced by the grid with their physical positions.

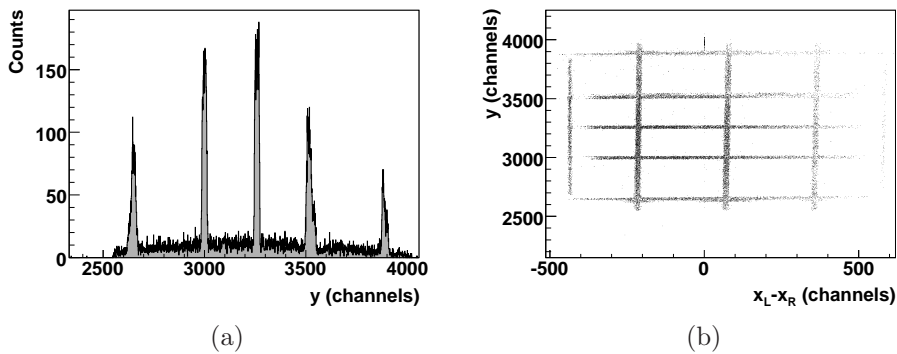


Figure 2.8: TPC position calibration. (a) Calibration for the TPC-4 in y position. Similar spectra were obtained for the other TPCs. (b) Two-dimensional scatter plot of the calibration of TPC4. The lines correspond to the position of scintillator fingers.

2.2.3. The plastic scintillators

BC420 fast plastic scintillators placed at S1, S2 and S4 were used as timing detectors for measuring the time-of-flight of the projectile residues. Their thicknesses were 5, 3.5 and 5 mm respectively and their dimensions provided full coverage of the focal planes. Each plastic scintillator was coupled to a pair of photomultiplier tubes (PMTs)(left-right for SC2 and SC4 and up-down to SC1). This double readout was used to avoid position dependencies in the time resolution. All the PMTs used were Hamamatsu R2083 tubes, but the S1 PMTs have the Hamamatsu H2431-50MOD assembly with a booster base [Yos96]. In this scheme, the interstage voltage of the last dynodes is provided by an independent high voltage power supply, providing very high counting rate capabilities. We expected very high rates produced by the fission fragments at the S1 focal plane.

The signals from the PMTs are filtered using constant fraction discriminators (CFDs) and then sent as START and STOP signals to time-to-amplitude-converters (TACs). The readout of the TACs was done with a CAEN V785 analog-to-Digital Converter (ADC).

2.2.4. The ionization chambers (MUSIC)

Two identical ionization chambers were placed at the intermediate and final focal planes in order to measure the energy loss of the reaction products. This measurement was then used to determine the atomic number of the fragments.

Multisampling ionization chambers were used in this work [Sch00b], with eight different active anodes, as depicted in Figure 2.11. Both chambers were 400 mm long and filled with tetrafluoromethane (CF_4), with an active area of $200 \times 80 \text{ mm}^2$ in the x and y directions. The windows were made of aluminium-coated mylar foils and float glass.

When a fragment crosses the chamber, according to Bethe-Bloch expression [Bet30], it loses energy proportionally to the square of its charge and the inverse of its velocity. An 8000 V voltage produced a uniform electric field between the electrodes, causing released electrons to drift to the anodes. The anode strips were read using an optimized charge-sensitive preamplifier and shaper combination for particle rates up to 200 kHz. The high rate capability is reduced with heavier fragments (40 kHz for fission residues).

The charge sensitive preamplifiers converted the charge of the collected electrons into a proportional amplitude signal. The signal was read by CAEN V785 ADC.

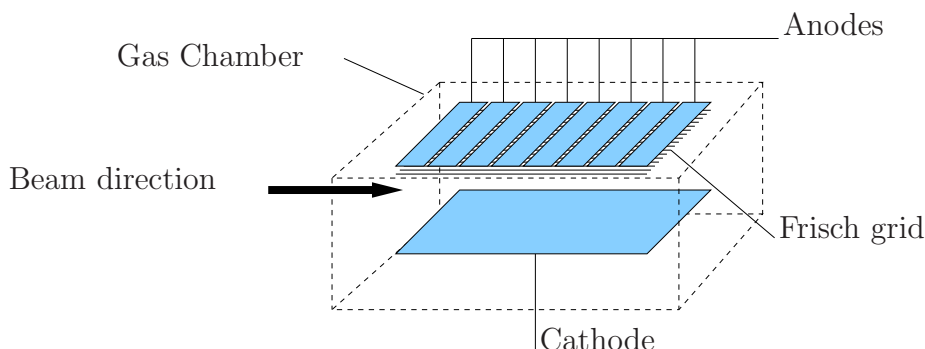


Figure 2.9: Schematic view of the MUSIC. Identical MUSICs with 8 independent anodes and filled with CF_4 were placed at S2 and S4.

2.2.5. The data acquisition system

The data acquisition system (DAQ) was based on the GSI Multi-Branch System (MBS) [MBS] and the VME bus. Two independent VME crates were used during the experiment in order to register the signals produced by each detector: one for the TPCs and one for the other detectors. The readout of each crate was controlled by a CES RIO3 VME processor. Data coming from each crate were sent to the event builder, a PC running LynxOS, a real-time operating system [LYN]. The events were distributed by the remote event server for on-line visualization with GO4 software [Go4]. The acquisition system runs on an event-by-event basis: for each accepted trigger, data are read out and sent to the event builder. Given the number of detection channels used in these experiments, the maximum processing rate possible with this acquisition system was around 1 kHz. Higher rates produced dead times larger than 30%.

2.3. Separation and identification of reaction products

The main challenge in this type of experiments is the unambiguous identification of all the projectile residues produced in the reactions. The identification method is based on the motion of a charged particle inside a uniform magnetic field, perpendicular to its velocity. This relation is expressed with the Lorentz force equation:

$$F = qvB = \gamma m_0 \frac{v^2}{\rho} \quad (2.2)$$

Here, B is the magnetic field, and ρ represents the curvature radius of the particle inside the field. m_0 is the rest mass of the particle and γ is the Lorentz factor, $\gamma = 1/\sqrt{1 - \beta^2}$.

From Eq. (2.2) we obtain:

$$B\rho = \frac{Au}{Qe}\gamma\beta c \quad (2.3)$$

In this expression, u is the atomic mass unit, e is the value of the elementary charge and c is the speed of light. $B\rho$ is known as *magnetic rigidity*. From the measurements of magnetic rigidity and velocity, the *mass-over-charge* ratio, A/Q , can be determined. An additional measurement of the atomic charge² Q with the ionization chamber, will allow us to identify with complete certainty all the nuclei produced in the reactions studied.

2.3.1. Magnetic rigidity determination

The four dipoles of the FRS bend the ion trajectories according to Eq. (2.2). The bending will cause the nucleus to reach different transverse positions in the focal planes of the FRS. Using ion-optical theory [Car87], the phase space coordinates of a particle in two different states is described by the following matricial equation:

$$\mathbf{x}_f = \mathbb{T}\mathbf{x}_0 \quad (2.4)$$

$\mathbf{x}_{0(f)}$ is a phase space vector representing the initial (final) state of the particle and \mathbb{T} is the so-called *transfer matrix*. If we concentrate now on the x position, we obtain:

$$x_f = (x|x)_\mathbb{T}x_0 + (x|x')_\mathbb{T}x'_0 + (x|y)_\mathbb{T}y_0 + (x|y')_\mathbb{T}y'_0 + (x|\delta B\rho)_\mathbb{T}\delta B\rho_0 \quad (2.5)$$

By definition, transverse positions and angles are independent at the focal planes ($(x|x')_\mathbb{T} = (x|y')_\mathbb{T} = 0$); so Eq. (2.6) will be reduced to:

$$x_f = (x|x)_\mathbb{T}x_0 + (x|y)_\mathbb{T}y_0 + (x|\delta B\rho)_\mathbb{T}\delta B\rho_0 \quad (2.6)$$

$(x|x)$ is the *magnification* and $(x|\delta B\rho)$ is the *dispersion*. Both quantities are characteristic of the spectrometer and its operation mode

Magnetic rigidity is usually described in terms of the relative variation of this magnitude with respect to the value of the rigidity of a particle following a central trajectory along the spectrometer:

²Q is different from the atomic number Z, if the ions are not fully stripped.

$$(\delta B\rho)_f = \frac{(B\rho)_f - (B\rho)_c}{(B\rho)_c} \quad (2.7)$$

In this equation, $(B\rho)_{c(f)}$ is the value of the magnetic rigidity in the central (final) positions. For a system with mid-plane symmetry, vertical and horizontal transverse coordinates are independent, therefore $(x|y)_T = 0$. By combining equations (2.6) and (2.7) we obtain a relation between the magnetic rigidity, the position at the intermediate focal plane and the optical characteristics of the magnetic system. For the intermediate focal plane S2, assuming that the beam emittance is small, $x_0 \sim 0$, we obtain:

$$(B\rho)_2 = (B\rho)_c \left(1 - \frac{x_2}{D_{02}} \right) \quad (2.8)$$

$(B\rho)_c$ is the magnetic rigidity corresponding to the central trajectory along the spectrometer, x_2 is the transverse position at the focal plane and D_{02} is the dispersion from the entrance of the spectrometer to the intermediate focal plane. In a similar way, we can determine the relation that provides the rigidity at the final focal plane

$$(B\rho)_4 = (B\rho)_c \left(1 - \frac{x_4 - V_{24}x_2}{D_{24}} \right) \quad (2.9)$$

x_2 and x_4 are the positions at the focal planes, D_{24} is the dispersion and V_{24} is the magnification.

According to these equations, magnetic rigidity can be obtained from the measured positions of the transmitted ions at the intermediate and final focal planes.

The magnitude $(B\rho)_c$ is measured by setting the magnetic fields of the spectrometer so that the primary ^{132}Xe beam is centered along the central trajectory of the FRS. The effective radii are obtained from the initial rigidity of the beam, taking into account the energy losses in the different layers present in the beam line. These radii, together with the magnetic fields in the dipoles measured with the Hall Probes, provide the rigidity of the central trajectory.

2.3.2. Velocity determination

The reduced momentum ($\beta\gamma$) of the reaction products is determined by measuring the time-of-flight (ToF) through the spectrometer. In these experiments, two ToF measurements were performed: one from the the first

focal plane (S1) to the intermediate dispersive plane (S2) ($ToF^{(1)}$) and the other from S2 to the final focal plane (S4) ($ToF^{(2)}$), see Fig. 2.6.

As explained in Sect. 2.2.3, each scintillator provides two time signals. The time-of-flight is obtained from the average of both signals.

$$ToF^* = \frac{1}{2} (\alpha_L \cdot ToF_L^* + \alpha_R \cdot ToF_R^*) \quad (2.10)$$

where ToF^* is the measured time-of-flight, $\alpha_{L(R)}$ are the TAC calibration factors and $ToF_{L(R)}^*$ is the measured time-of-flight with the left (right) PMTs of each scintillator. These factors were obtained using a time calibrator.

The START signals for the ToF measurements are given by the scintillator placed at S2 and S4 for $ToF^{(1)}$ and $ToF^{(2)}$, respectively. For this reason, the signals provided by scintillators placed at S1 and S2 must be delayed a quantity $T_0^{(i)}$ in order to ensure the arrival of the START signal before the STOP signal. The real $ToFs$ are then obtained as

$$ToF^{(i)} = T_{STOP}^{(i)} - T_{START}^{(i)} = T_0^{(i)} - ToF^{*(i)} \quad (2.11)$$

The parameter $T_0^{(i)}$ was obtained by comparing the $ToF^{*(i)}$ signals of the primary beam with the inverse of the velocity ($1/v$) of the ^{132}Xe beam after traversing different layers of matter. The values of the velocities are calculated with AMADEUS taking into account the beam energy and energy losses in the different layers of matter placed along the FRS [AMA]. The results are then fitted to a first-order polynomial (See Fig. 2.10):

$$\frac{1}{v^{(i)}} = \frac{T_0^{(i)}}{L_0^{(i)}} - \frac{ToF^{*(i)}}{L_0^{(i)}} \quad (2.12)$$

In this equation, the two parameters are the delay values ($T_0^{(2)}$) and the path length of the beam from S1 to S2 (S2 to S4) ($L_0^{(2)}$).

2.3.3. Atomic number determination

As mentioned in sect. 2.2.4, the energy loss of the fragments in the MUSICs is proportional to the square of its atomic number (Z^2). Provided the ions are fully stripped, we can determine the atomic number of the reaction residues from the average energy loss of the eight different anodes as follows:

$$Z = A + B \sqrt{\sum_{j=1}^N \frac{\Delta E_j}{N}} \quad (2.13)$$

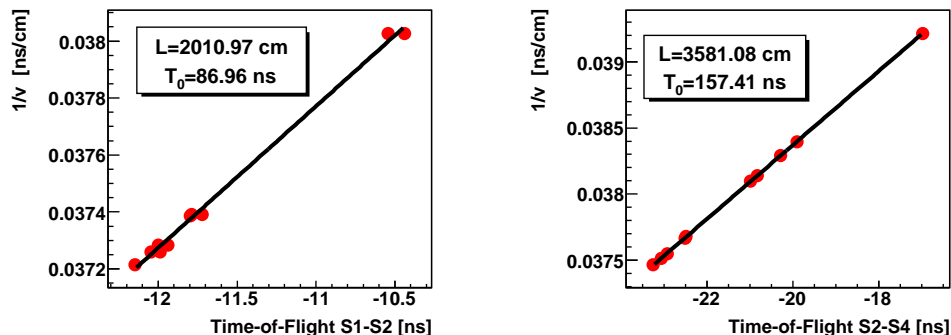


Figure 2.10: Time-of-Flight(ToF) versus inverse of velocity plots used for calibration. The left panel corresponds to S1-S2 ToF and the right panel to the S2-S4 ToF.

where N is the number of anodes with a good signal, ΔE_j is the amplitude of the signals from each anode, and A and B are calibration parameters. These parameters were determined from the characteristic asymmetric charge distribution pattern of the fission fragments at low energies, taking into account the enhanced productions of Te ($Z=52$) and Zr ($Z=40$) (Fig. 2.11). We evaluated the probability of having different charge states in the MUSIC which would produce a misidentification of the reaction products, and found it to be below 2% in the energy and charge ranges used in this work.

2.3.4. Mass-over-charge ratio determination

According to Equation (2.3), the mass-over-charge ratio (A/Q) of the transmitted nuclei can be obtained by combining two independent measurements: the magnetic rigidity, determined from the position measurements, and the velocity, calculated from the measured time-of-flight. The calculated A/Q , together with the atomic number obtained from the MUSIC chambers, can be used to produce an identification cluster plot like the one shown in Figure 2.12, where each nucleus is represented by a spot. As we can see, the resolution in A/Q and atomic number achieved in these measurements are very good, allowing us to unambiguously separate all the fission fragments produced and transmitted along the magnetic spectrometer.

The mass was identified with the help of the ion-optical code LIESCHEN [LIE]. This code predicts the ion optical-separation of secondary beams with the Fragment Separator at GSI and provides a list of all the nuclei transmitted through the spectrometer at a given magnetic setting together with their positions in the focal planes. By comparing the measured position with

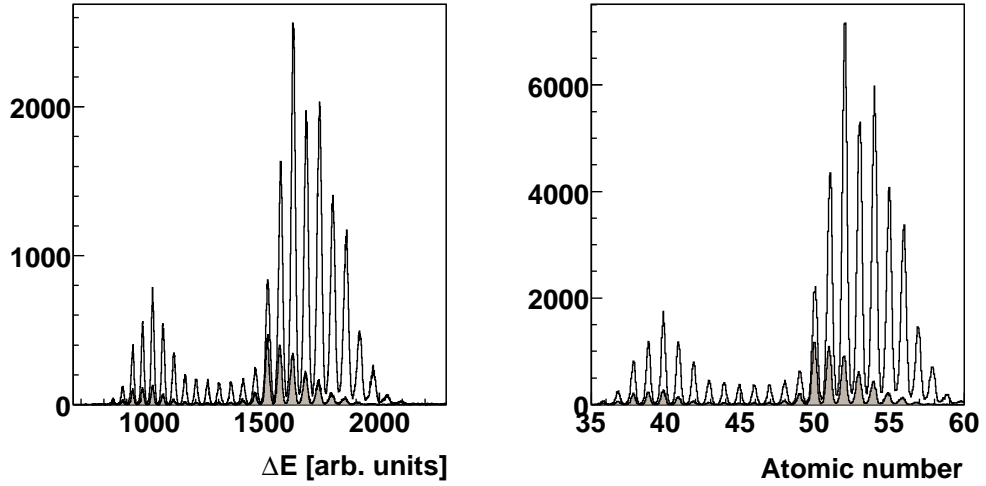


Figure 2.11: Left panel: Average energy loss in the MUSIC detectors. Right panel: Calibrated MUSIC spectrum for two different magnetic settings centered at ^{132}Sn (filled histogram) and ^{129}Sn . (empty histogram)

the TPCs at the focal plane with the positions calculated by LIESCHEN, together with the relative yields of the isotopes for a given element, we were able to identify all the fission residues produced in the reactions $^{238}\text{U} + \text{Pb}$, Be at 950 AMeV at several magnetic settings, centered in different Sn isotopes. ($^{126,129,132,135,138}\text{Sn}$). We also studied the fragmentation on Be of the ^{132}Sn produced in the fission of ^{238}U . The results of both studies will be discussed in detail in the following chapters.

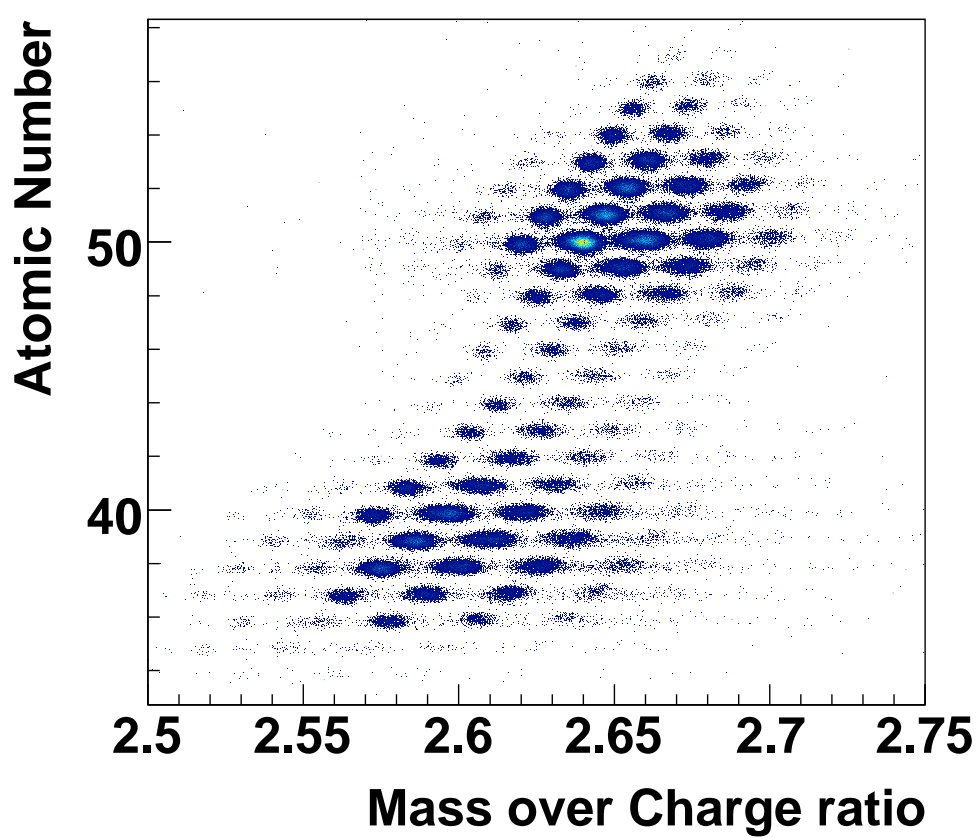


Figure 2.12: Identification plot (atomic number versus mass-over-charge ratio) of the fission residues produced in the reaction $^{238}\text{U}+\text{Pb}$ at 950 AMeV and transmitted along the FRS in a setting centered around ^{135}Sn .

Chapter 3

Production of medium-mass neutron-rich nuclei in fission reactions

This chapter is dedicated to the analysis of the production cross sections of medium-mass neutron-rich nuclei produced in the fission of ^{238}U projectiles induced by lead and beryllium targets at 950 AMeV. These two targets allowed us to explore fission at different excitation energies.

The experimental set-up used in this work made it possible to identify the forward-emitted reaction products. The cross sections were determined from the measurement of their production yields, normalized to the beam intensity and the target thickness.

The chapter is divided in two parts. First is a detailed explanation of how the cross sections were determined, with a discussion of all the corrections that were applied. Then, the experimental results are presented and compared with previous measurements found in the literature and with model calculations.

3.1. Determination of the production cross sections

The production of a given isotope $N(Z, A)$ in a reaction is directly linked to the cross section of that reaction channel, $\sigma(Z, A)$, according to the Equation (3.1)

$$N(Z, A) = N_p \sigma(Z, A) N_t e^{-\sigma(Z, A) N_t} \quad (3.1)$$

Here, N_p represents the number of beam particles and N_t the number

of particles in the target per unit area. Assuming the factor $\sigma(Z, A)N_t$ to be small (for relatively thin targets) we can keep the first-order term in the power expansion of (3.1) to obtain a simple relation between the production yields and the cross sections:

$$\sigma(Z, A) = \frac{N(Z, A)}{N_p N_t} \quad (3.2)$$

In the present experiment, the ratio $Y(Z, A) = N(Z, A)/N_p$ is determined from the number of counts obtained for each identified fragment in the final focal plane of the spectrometer and the number of incident beam particles as explained in Chapter 2.

From these measurements, the production cross sections for the ^{238}U fission residues induced by Pb and Be targets can be obtained with the following expression:

$$\sigma(Z, A) = \frac{1}{N_t} \cdot Y(Z, A) \cdot F \quad (3.3)$$

where N_t is the target thickness and $Y(Z, A)$ the yield for each nucleus. The factor F , corresponds to all the corrections applied due to the limitations of the experimental setup. This factor is calculated as the product:

$$F = f_{eff} \cdot f_{dt} \cdot f_{tr} \cdot f_{sr} \quad (3.4)$$

where f_{eff} accounts for the efficiency of our detection system, f_{tr} corresponds to the angular transmission due to the limited angular acceptance of the spectrometer, and f_{sr} corresponds to the secondary reactions in the different layers of matter present in the beam line. Finally f_{dt} is a correction factor that accounts for the dead time of the data acquisition.

In the next sections, we will describe these factors in detail.

Efficiency of the detection setup

The detection efficiency is defined by the fraction of fission residues that was not registered by the detectors. The detection efficiencies of the three scintillators and the MUSICs were estimated in previous experiments to be greater than 99%. However, the TPC detectors present lower efficiencies, around 85%. This efficiency was determined from the ratio between the number of events registered by the TPC with a good value in the position and the total number of events detected by the scintillator.

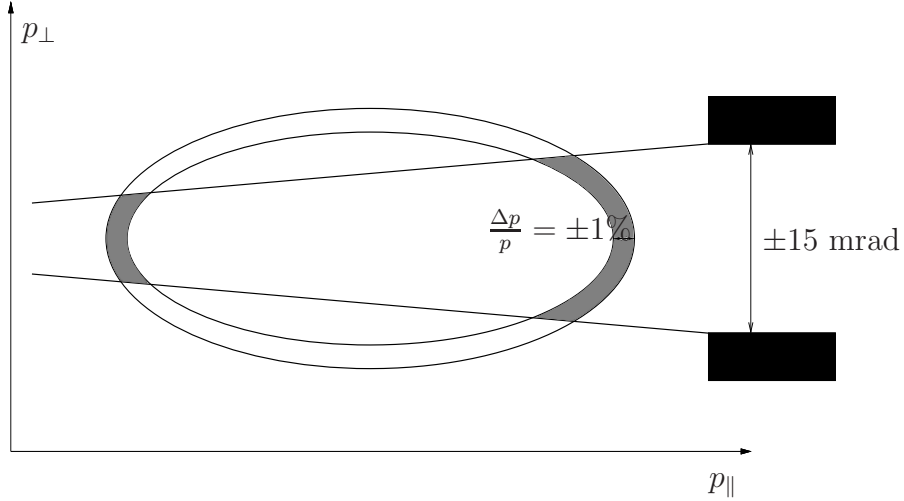


Figure 3.1: Momentum diagram of fission in relativistic inverse kinematics. The shaded area of the ellipsoid is the part of the fission fragment momentum distribution accepted by the FRS.

Dead time correction

In order to correct the measured cross sections for the dead time of the data acquisition system (DAQ), the number of free triggers was continuously monitored with an independent scaler. From the ratio between the number of triggers accepted by the DAQ and the free triggers we obtain a value for the dead time efficiency. The number of free triggers varies depending on the characteristic production rates of the explored isotopical region. In regions with very high counting rates, the dead time was reduced by decreasing the beam intensity in order to keep it below 30%. In the magnetic settings for exploring the most exotic regions, the dead time was lower than 1%.

Angular transmission

The kinematics of the fission residues is governed by the strong Coulomb repulsion between the two fragments. In the ^{238}U reference frame, fragments are emitted back to back with an angular distribution that is isotropic to the first order. For a given nucleus, the resulting spherical shell of momenta is converted to a cone of vectors ending on a shell of an ellipsoid in the laboratory system (see Fig. 3.1). Since the opening angle of this ellipsoid is larger than the limited angular acceptance of the FRS (± 15 mrad) only fragments emitted either forward or backward are transmitted through the spectrometer. In addition, the momentum acceptance of the separator ($\pm 1\%$) selects

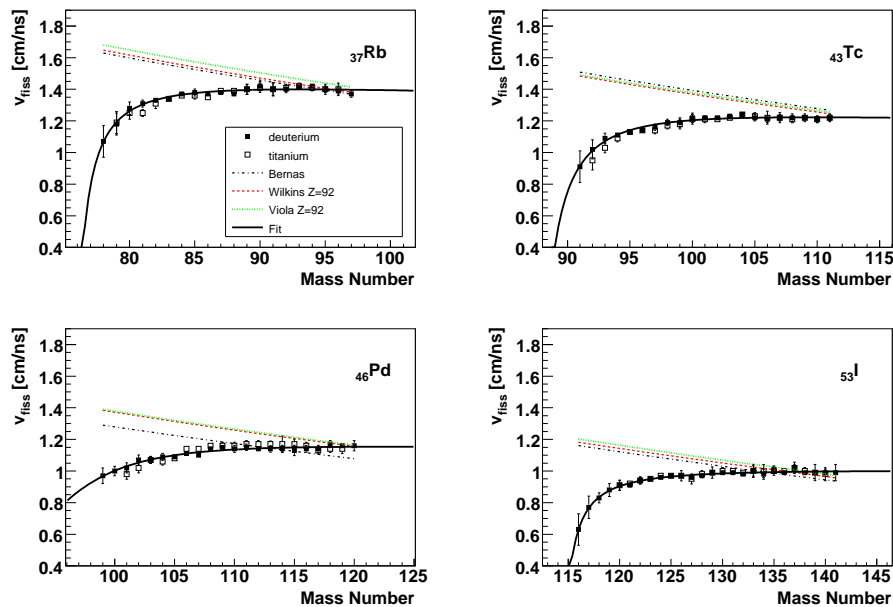


Figure 3.2: Velocity of fission fragments produced in the reaction $^{238}\text{U} + d$ and $^{238}\text{U} + \text{Ti}$ at 1 AGeV. The thick line shows the parameterization, the dashed line is the Wilkins model for $Z=92$ as fissioning system, and the dash-dotted line the parameterization according to M. Bernas.

only one of the two fission fragments. In order to estimate the transmission of the fission residues from the production target to the S4 experimental area along the FRS, we have performed a simulation of the transport of the fission products through the spectrometer with an enhanced version of the MOCADI code [MOC]. In this version, a new parameterization of the fission velocities was included, which was obtained from the fission velocities (Eq. (3.5)) measured in the reactions $^{238}\text{U} + d$ and $^{238}\text{U} + \text{Ti}$ at 1 AGeV in another experiment [Per07a] and extrapolating the behaviour to the more neutron-rich part:

$$v_{fiss}(Z, A) = \frac{a + cA + eA^2}{1 + bA + dA^2} \quad (3.5)$$

where a, b, c, d and e, are parameters that depend on the charge of the fission fragments. These parameters, can be found in Appendix C.

Figure shows the measured fission velocities for Rb, Tc, Pd and I with the deuterium and titanium targets, compared with different models for the Total Kinetic Energy (TKE) released in the fission process [Wil76; Vio85]. The experimental data show that velocities are independent of the target. Moreover, the fission models overestimate the velocities in the neutron-deficient

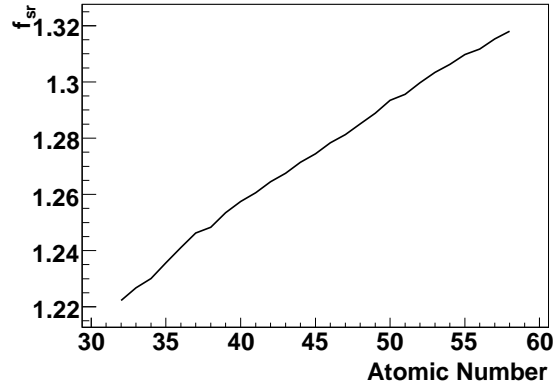


Figure 3.3: Correction factor f_{sr} due to secondary reactions taking place in other layers of matter along the FRS.

part for all the elements. For the neutron-rich part, models underestimate the value of the fission velocities. On the other hand, the fit reproduces fairly well the measurements, reproducing also the expected behavior in the extrapolation. The systematic uncertainty estimated for this correction is around 10%.

Secondary reactions

The forward-emitted fission residues produced in both targets may undergo secondary nuclear reactions before leaving the target or in the scintillator at first focal plane and in the different layers of matter in the intermediate focal plane. The reaction products have different mass-over-charge ratios that will be rejected by the second part of the separator, leading to an underestimation of the measured production yields. This must be corrected in order to obtain an accurate value for the cross sections. The correction factor $f_{sr}(Z, A)$ was determined for each nucleus as the inverse of their survival probability after traversing the different layers of matter:

$$P_{sr}(Z, A) = \prod_i e^{\sigma_T^i(Z, A) \cdot x_i} \quad (3.6)$$

Here, $\sigma_T^i(Z, A)$ is the total reaction cross section of the nucleus in the layer i and x_i is the density of atoms per unit area of the layer. The cross sections are calculated according to the Karol's microscopic model with an accuracy around 10% [Kar75].

Figure 3.3 shows the correction factor f_{sr} averaged over each isotopic chain as a function of the atomic number. The values for this correction factor are

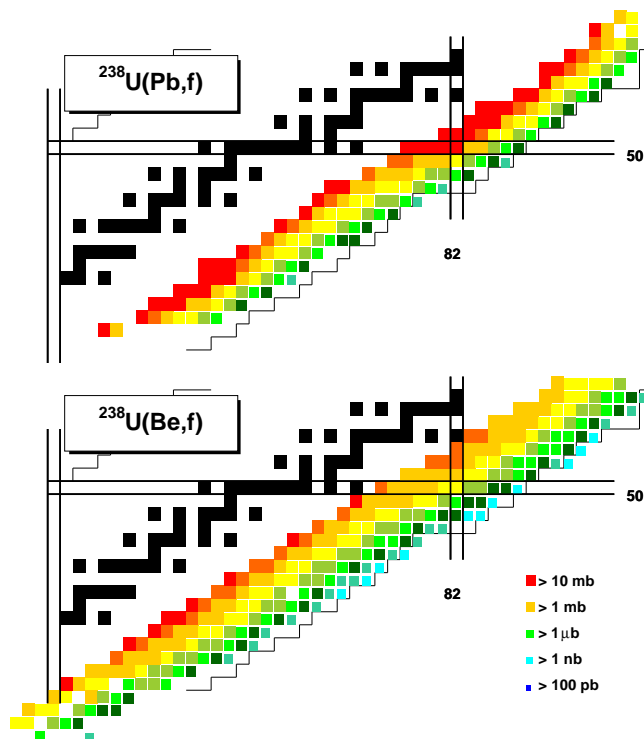


Figure 3.4: Fission residues of ^{238}U at 950 A MeV induced by Pb (top panel) and Be (bottom panel) reactions measured in this work on top of the chart of the nuclides. The color scale indicates the different production cross sections.

quite significant, ranging from 20%, for the lowest charges up to 30% for the highest. The uncertainty associated to this correction is below 2%.

3.2. Measured cross sections

Figure 3.4 presents, for both targets, all the fission residues measured in this work on top of the chart of the nuclides. They mainly cover the most neutron-rich part of the medium- mass fragments, ranging from rubidium to barium. The measured cross sections range from about 100 mb to values as low as 100 pb on the neutron-rich side.

Figures 3.5 and 3.6 provide a more detailed survey of the fission residue production, showing the isotopic production cross sections for all measured fission residues using both targets. Together with the experimental data, polynomial fits in log scale are also shown. They are used to extrapolate the behaviour of the cross sections to the most neutron-rich isotopes which were not measured in this work. This extrapolation will be discussed in detail in subsection 3.2.1.

This work corresponds to the most complete overview of the production of neutron-rich nuclei in fission. As can be seen, after a few hours of measurements, we were able to reach the present limits of the chart of nuclides in the region of medium-mass nuclei.

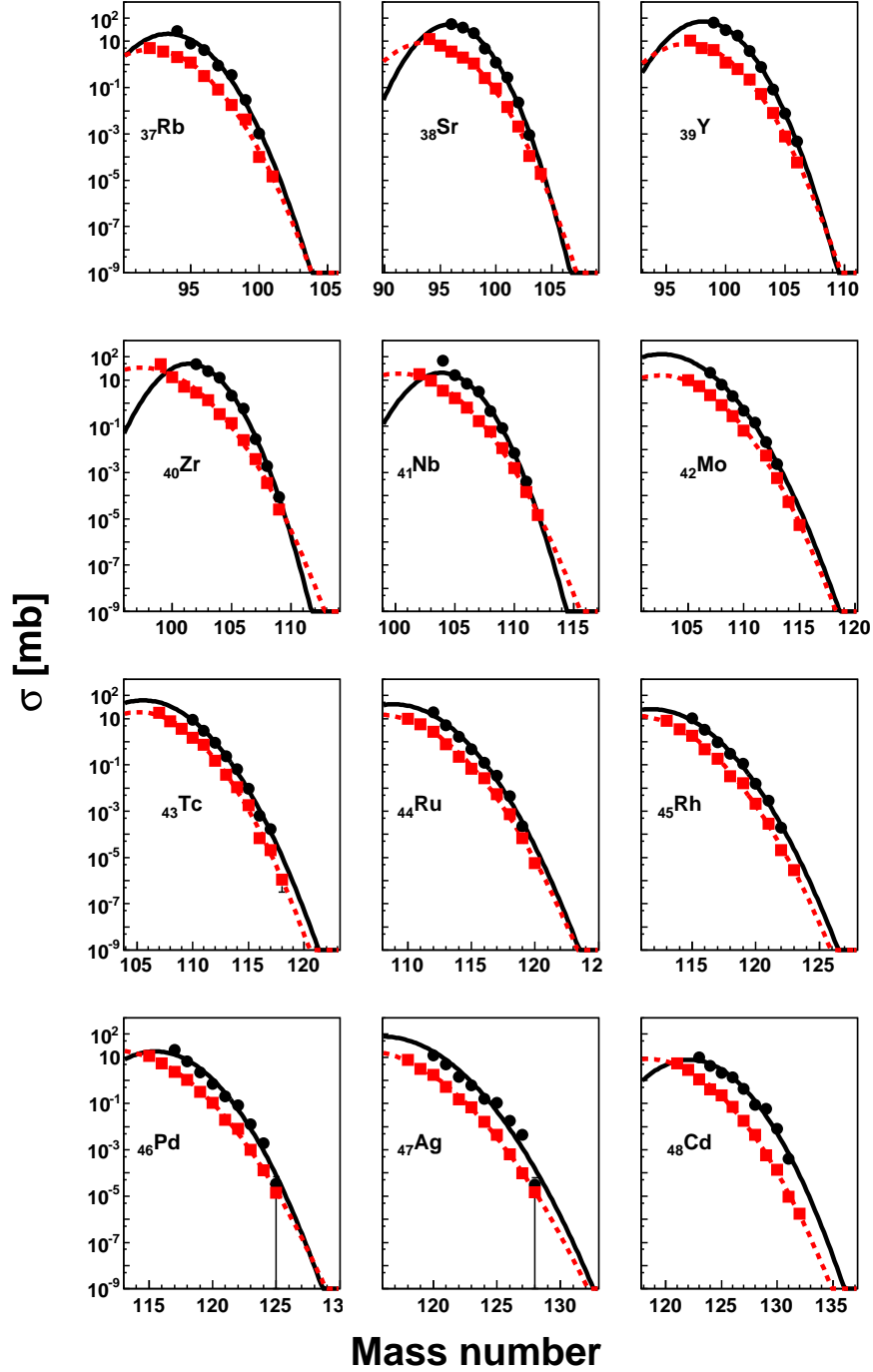


Figure 3.5: Measured isotopic production cross sections of fission residues produced in the reactions $^{238}\text{U}(950 \text{ AMeV})+\text{Pb}$ (black circles) and $^{238}\text{U}(950 \text{ AMeV})+\text{Be}$ (grey squares). Error bars are shown if bigger than the symbols. The lines correspond to polynomial fits of the measured cross sections. (See text for details).

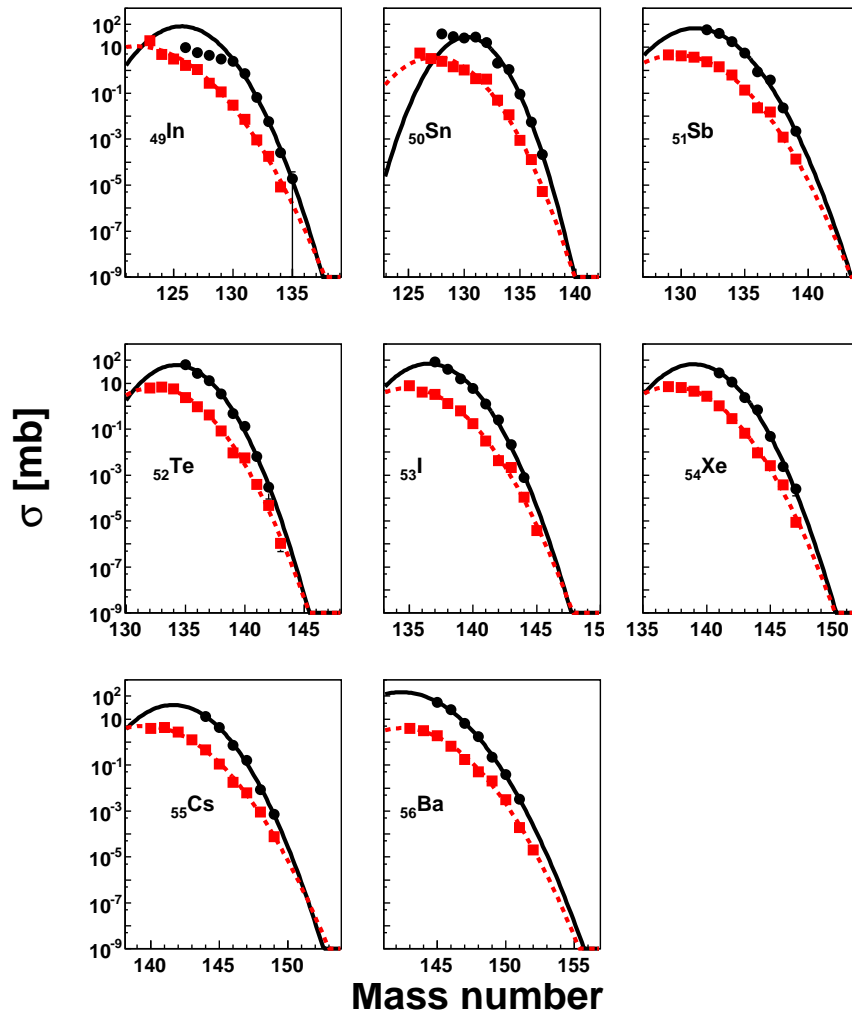


Figure 3.6: Measured isotopic production cross sections of fission residues produced in the reactions $^{238}\text{U}(950\text{ AMeV})+\text{Pb}$ (black circles) and $^{238}\text{U}(950\text{ AMeV})+\text{Be}$ (grey squares). Error bars are shown if bigger than symbols. The lines correspond to polynomial fits of the measured cross sections. (See text for details).

Fission residues of ^{238}U at 950 AMeV induced by Pb

The fission induced by the lead target is mainly due to the electromagnetic excitation of the ^{238}U . Therefore, fission takes place at low excitation energies. In order to benchmark the results measured, we have compared the cross sections obtained with previous measurements performed by Enqvist et al. [Enq99] in the reaction $^{238}\text{U}+\text{Pb}$ at 1 AGeV and the ABRABLA code [Gai91; Ben98; Jon98; Jun98] (See Figure 3.7).

The agreement between both sets of data in the overlapping area is fairly good. The isotopic distributions show the expected behaviour corresponding to low excitation energy fission. The mass distribution is asymmetric, with the largest productions corresponding to ($^{134}\text{Te}/^{104}\text{Zr}$) fragments around $N\approx 82$ shell and ($^{142}\text{Xe}/^{96}\text{Sr}$), $N\approx 88$ [Bro90]. However, the region around the symmetric splitting presents lower production yields. Agreement with the ABRABLA calculations for the most neutron-rich nuclei is also rather good, but in some cases, the calculation can not reach the most exotic fragments measured, even for a very long calculation (one week). This could be due to the low cross sections of these channels.

Fission residues of ^{238}U at 950 AMeV induced by Be

In this section, the production cross sections of the fission residues induced by the beryllium target that were measured in this work are compared with the production cross sections measured in the reaction $^{238}\text{U}(1\text{ AGeV})+\text{d}$ [Per07b]. Due to the fact that both targets present low charges, the fission is mainly induced by nuclear reactions. The fissioning system will not be only ^{238}U , but also their reaction products, with an excitation energy around 27 MeV per abraded nucleon [Sch93]. The fission will take place then at higher excitation energies compared to the lead target. Both the beryllium and deuterium targets should present similar production cross sections for the reactions in which the lowest amount of excitation energy is transferred to the fissioning system due to the abrasion of one or two nucleons. Figure 3.8 shows the measured production cross sections of fission fragments of ^{238}U induced by the beryllium target, compared with the deuterium data and ABRABLA calculations for the $^{238}\text{U}+\text{Be}$ system. As we expected, the mass distribution of the fission fragments is more symmetric, compared to the case of the lead target, with similar productions for all the elements. Agreement with the deuterium data is rather good for the large neutron excess in the overlapping area. However, the most neutron-rich isotopes were not produced with the deuterium target. The ABRABLA calculation also reproduces the experimental results rather well.

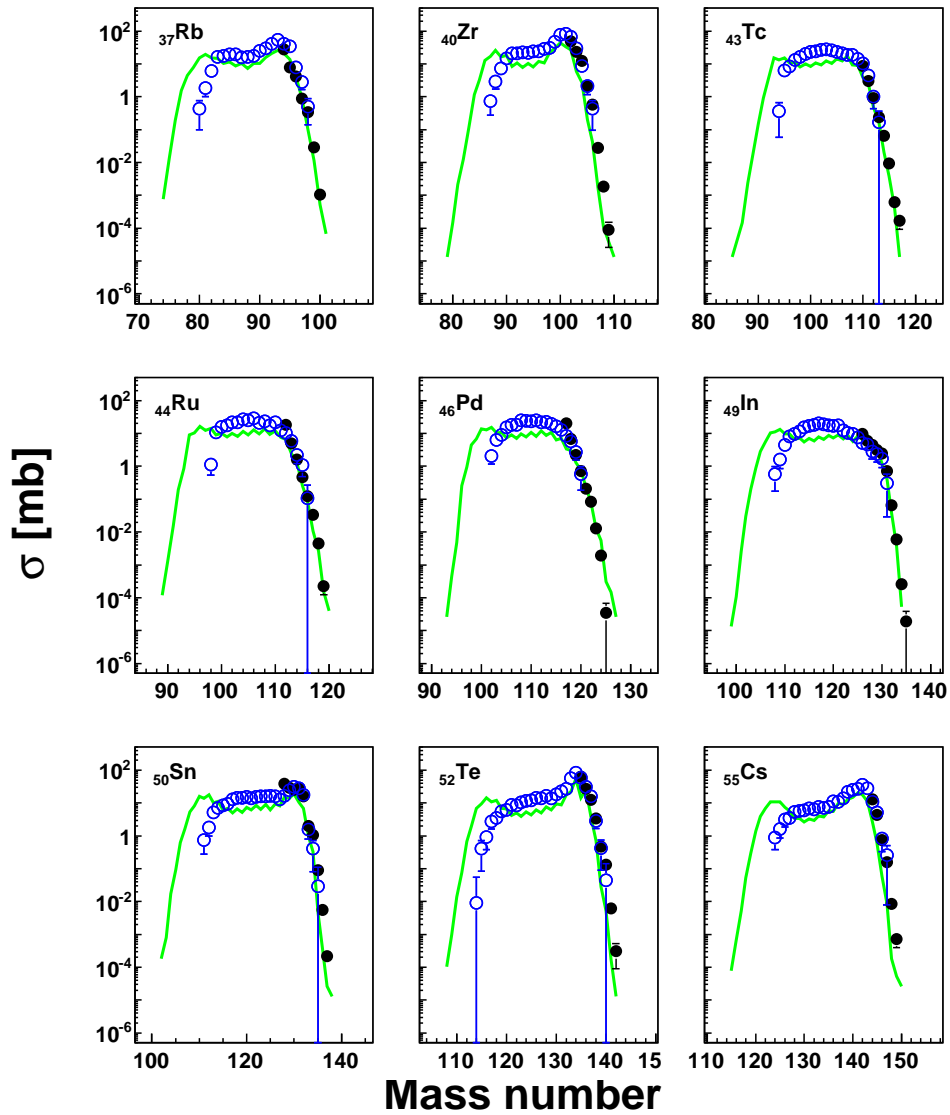


Figure 3.7: Some of measured isotopic production cross sections of fission residues produced in the reaction $^{238}\text{U}(950 \text{ AMeV})+\text{Pb}$ in the present work (full dots) compared to the previous results obtained by Enqvist et al. [Enq99] (empty dots). Error bars are shown if bigger than symbols. The solid line corresponds to the ABRABLA calculations.

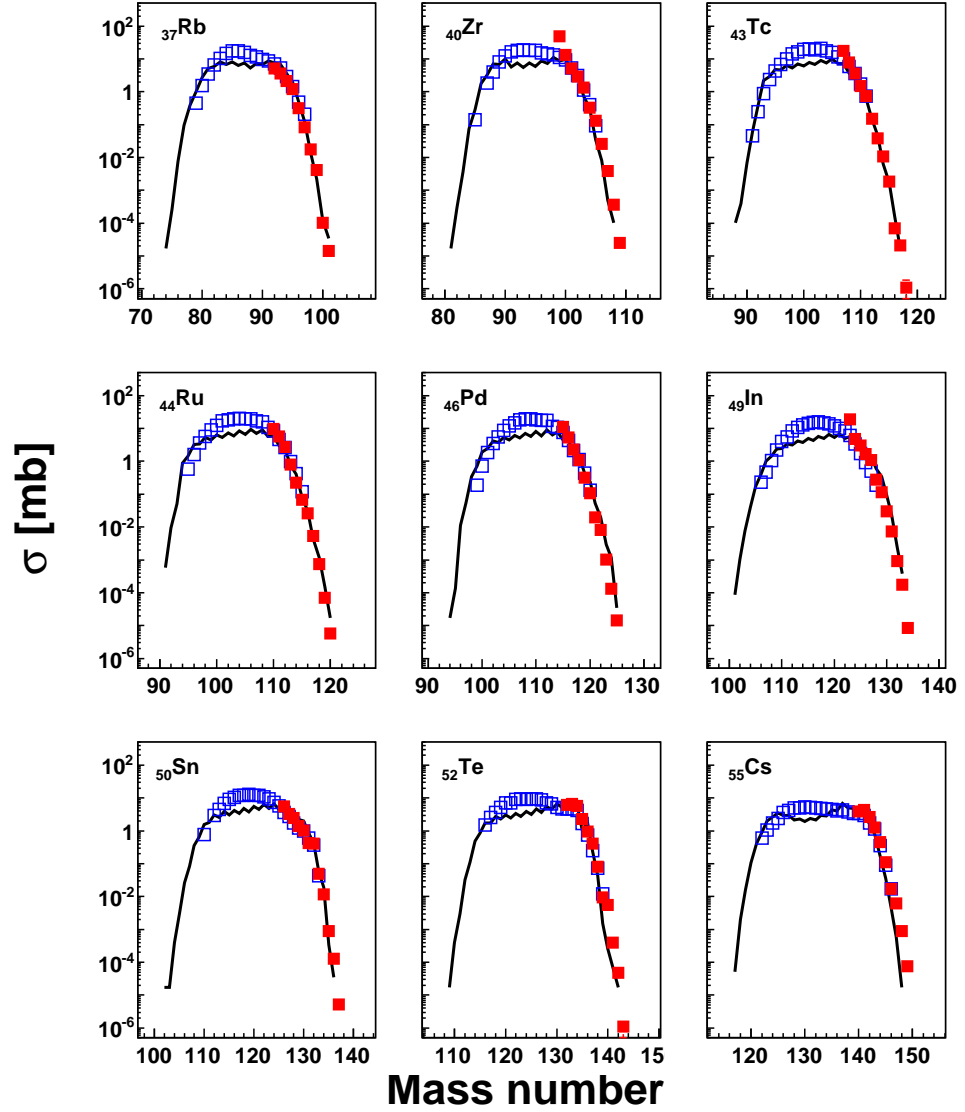


Figure 3.8: Some of the measured isotopic production cross sections of fission residues produced in the reaction $^{238}\text{U}(950 \text{ AMeV})+\text{Be}$ (full squares) compared to the results obtained for the reaction $^{238}\text{U}(1 \text{ AGeV})+d$ [Per07b] (empty squares). Error bars are shown if bigger than symbols. The solid line corresponds to the ABRABLA calculations for the $^{238}\text{U}+\text{Be}$ system.

3.2.1. Energy dependence of the fission yields

In this section we will take advantage of the two targets used in this work for inducing fission to investigate the energy dependence of the fission yields. The lead target, due to its large atomic number, is known to enhance the electromagnetic-induced fission through the excitation of the Giant Dipole Resonance (GDR) in ^{238}U [Sch00a]. In this case, the excitation energies at which the fission takes place range from 5 to 15 MeV. The left panel of Figure 3.9 shows the calculated fission probability induced by Coulomb excitation in ^{238}U as a function of the excitation energy. This probability was calculated with the ABRABLA code from the differential cross section for the electromagnetic excitation of ^{238}U [Gre97; Ber88]. The plot shows a peak around 13 MeV, which corresponds to the GDR. The right panel of this figure shows the fission probability versus excitation energy for the $^{238}\text{U}+\text{Be}$ system. The electromagnetic component is highly suppressed because of the lower atomic number. Therefore, nuclear reactions are the main reaction mechanism with an excitation energy of around 27 MeV per abraded nucleon [Sch93]. The

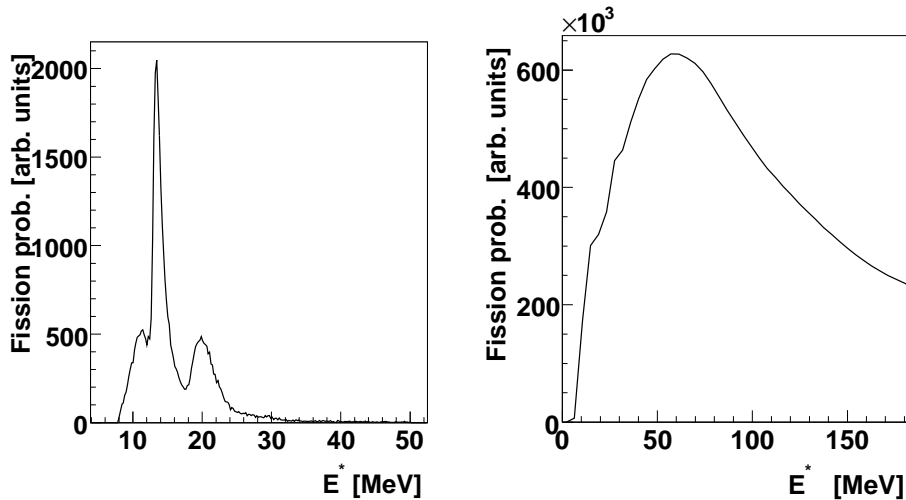


Figure 3.9: Left panel: Calculated fission probability of ^{238}U projectiles after electromagnetic excitation on Pb target. Right panel: Calculated fission probability in the reaction $^{238}\text{U} + \text{Be}$ at 950 A MeV.

cross sections obtained with the beryllium and lead targets (Figs. 3.5 and 3.6) clearly show the different excitation energy regimes. As mentioned before, fission induced by the lead target yields an asymmetric pattern for the fission fragments. This fact is reflected in the larger production cross sections of, Sn, Sb, Te, I, Xe, Cs and Ba, and their light partners when compared to

the symmetric splitting of uranium (Pd). In the case of the beryllium target, the distribution of fission fragments is more symmetric, with similar productions for all the fission residues shown. The isotopic cross sections also show a different behaviour of the maxima in both targets. In the case of the lead target, the maximum of the distribution is more neutron-rich than in the beryllium target. This can be understood in terms of the excitation energy at which fission takes place and the deexcitation of the residues by neutron evaporation. Because the excitation energy between the two emerging fission fragments is shared according to their masses, this effect is more clearly observed for the heavy fragments, which take the greater part of the excitation energy. At low excitation energies, the probability of neutron evaporation is low, therefore, the two fission fragments keep the neutron excess of the fissioning system. At higher excitation energies, evaporation of neutrons may occur during de-excitation.

Another interesting feature observed in the isotopic distributions is that they are wider with the beryllium target. In fact, for lighter elements the production for the most neutron-rich residues obtained with the beryllium target are larger than those measured with the lead target.

In order to extrapolate the behaviour of the cross sections for the different isotopic chains to even larger neutron excess, the measured distributions were fitted with a parabolic function in log scale (Figs. 3.5 and 3.6). This will help us to determine the optimum excitation energy range for the production of the most neutron-rich nuclei. From the extrapolation we conclude that most neutron-rich light fission residues have larger productions with the beryllium target.

Fission at low excitation energies yields a largest production of some specific fission fragments, around the $N=82$ shell closure, such as ^{134}Te and their corresponding charge partners. In contrast, production yields are low around the symmetric splitting (^{119}Pd).

From these results, we can conclude that fission at moderate excitation energies produces more symmetric, but broader mass distribution, increasing the production yields around the symmetric fission. In fact, the neutron excess distribution broadens, compensating the neutron evaporation and leading to the production of fission residues with a larger neutron-excess than that obtained in fission at low excitation energies, especially for light fission fragments.

Figure 3.10 shows the results of calculated fission yields for different excitation energies using the model from [Ben98] for Zr, Tc, Pd and Te isotopes in ^{238}U fission. The calculation reproduces the behaviour observed in the experimental data: The higher the excitation energy, the more symmetric the mass distribution becomes. This is shown in the yield of the palladium

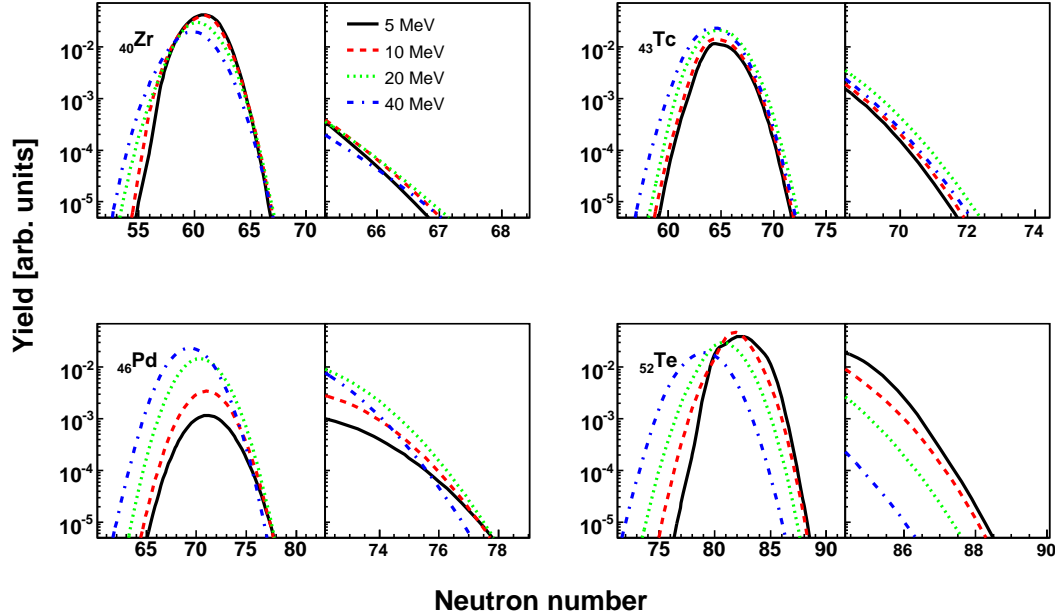


Figure 3.10: Calculated production yields of fission residues of ^{238}U for different excitation energies. The right panels for each element correspond to an close-up view of the large neutron excess area. See text for details.

($Z=46$). At energies above 20 MeV the yield increases by more than one order of magnitude. The right panels of this figure present a close-up view of the calculated isotopic distributions in the region of large neutron excess. We can see how larger excitation energies produce more neutron-rich isotopes in the case of light fission fragments. However, the broader distribution does not compensate the effect of the neutron evaporation for heavier fragments (Te).

From the fit parameters used for the extrapolation, we can define a *mean* value for the distribution, which corresponds to the maximum of the distribution and a *width*, defined as the full width at half of the maximum. Using these values of this two parameters, a systematic study of the behaviour of the two parameters with the charge of the fission fragment is shown in Figure 3.11. The left panel shows the width of the mass distribution as a function of the atomic number of the fragment. As expected, the distributions obtained with the beryllium target are wider than in the case of the lead target. However the differences become smaller around the symmetric splitting. The same happens with the mean value of the distribution. The maximum of the

isotopic distributions is more neutron-rich in the case of the lead target, but maxima are similar in neutron excess around the symmetric fission. This fact leads us to assume that most of the fragments which correspond to the symmetric fission with lead target are also produced in nuclear reactions. The larger cross sections observed in the case of the lead target for the symmetric splitting can be explained based on the larger size of the lead nucleus, compared to the beryllium.

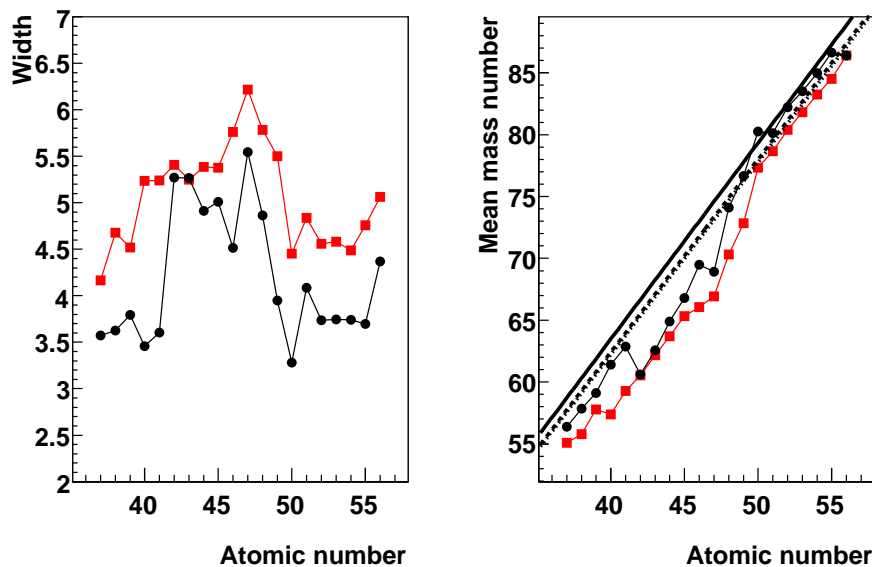


Figure 3.11: Dependence of the width (left panel) and mean value (right panel) of the isotopic distributions for the lead (circles) and beryllium (squares) targets. The straight lines correspond to the mass-over-charge ratio of ^{238}U (solid line) and ^{231}Th (dashed line).

3.3. Conclusions

In this chapter we have investigated the production cross sections of medium-mass neutron-rich nuclei from the fission of ^{238}U at 950 AMeV impinging onto a beryllium and lead targets. These two targets allowed us to investigate the energy dependence of the fission yields to determine the optimum excitation energy for the production of the most neutron-rich isotopes.

The production cross sections of neutron-rich isotopes were measured for elements between Rb and Ba with values as low as 100 pb using both

targets. We have shown that the mass distribution of the fission residues produced by the lead target is more asymmetric, with larger productions corresponding to fragments close to the magic number $N=82$, due to shell effects. In contrast, for the beryllium target, distribution of the fission fragments becomes more symmetric and the shell effects are damped due to the higher excitation energy at which the fission takes place. The isotopic distributions of the fission residues produced in the beryllium-induced fission are also wider due to the larger fluctuations in isospin. In the case of the lead target, the maxima of the isotopic distributions are more neutron-rich than those corresponding to the beryllium target. This fact is due to the larger probability of neutron evaporation in the case of the fission induced by nuclear reactions. However, even though the maximum less neutron-rich, the wider distributions compensate this effect, producing more neutron-rich isotopes, specially for lighter elements. Therefore, we can conclude that fission at moderate excitation energies (around 50 MeV) is a better mechanism for the production of very neutron-rich medium-mass nuclei.

Chapter 4

Production of medium-mass neutron-rich nuclei using a two-step reaction scheme

The fragmentation of post-accelerated fission fragments is being proposed for the production of medium-mass neutron-rich nuclei in ISOL facilities. In this chapter we contribute to the feasibility studies of the production of medium-mass neutron-rich nuclei using the results of an experiment we performed to investigate the fragmentation of ^{132}Sn .

4.1. Description of the experiment

In this experiment, we used ^{238}U at 950 AMeV as primary beam. This primary beam impinged onto a lead target in order to induce electromagnetic fission. The two sections of the FRagment Separator (FRS) were utilized as two independent magnetic spectrometers, each with a different magnetic setting. In the first section of the FRS, which was tuned to get ^{132}Sn in the center of the intermediate focal plane, the fission fragments produced by the primary beam were unambiguously identified in mass and atomic number. As mentioned in Chapter 2, a 2591 ± 7 mg/cm² beryllium target was placed at the intermediate focal plane to induce fragmentation of the fission residues. The fragmentation products were then separated and identified in the final focal plane using the second part of the spectrometer (See Fig. 2.6). To cover a wide range of fragmentation residues, the second part was tuned in 6 different settings, centered in ^{132}Sb , ^{132}Sn , ^{131}In , ^{123}Ag , ^{126}Ag and ^{129}Ag to cover a large range of fragmentation residues.

As shown in Figure 2.6 the scintillators used for the determination of

the time-of-flight in the first section, were placed in the first (S1) and the intermediate (S2) focal planes. This reduced the flight path length to only 18 m, thus, a very high time resolution (better than 150 ps FWHM) was required in order to separate fragments with masses around $A=130$. The photomultiplier tubes coupled to the plastic scintillator placed at S1 also had to be adapted to support very high counting rates (2.2×10^5 events/s) due to the large number of fission fragments produced. In order to overcome this difficulty, the Hamamatsu H2431-50MOD assembly with a booster base was used. In this scheme, the interstage voltage of the last dynodes is provided by an independent high voltage power supply, therefore, even if the output current of the tube is increased, due to high counting rate, there are no voltage losses which would spoil the time resolution. The filled histogram of Figure 4.1, shows the time resolution achieved in the time-of-flight after the correction for the angle of the fragments measured with the TPCs placed at the S2 plane. This correction accounts for the different path lengths of the nuclei due to their trajectories inside the magnetic spectrometer.

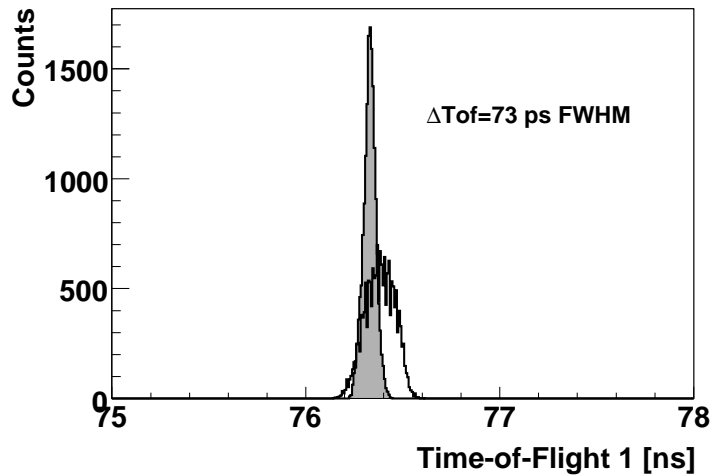


Figure 4.1: Time resolution obtained in the first stage of the FRS, before and after applying angular corrections.

Trigger system

Two different triggers were used in the experiment in order to determine the production cross sections of the fragmentation residues of ^{132}Sn . The two-trigger scheme was required for determining of the number of particles

impinging on the secondary target. This number was used to normalize the production yields and thus obtain the cross sections.

One of the triggers was given by the scintillator placed at S4 (Trigger #3). This trigger corresponds to those ions that reached the final focal plane of the spectrometer. When the data acquisition system (DAQ) was triggered by Trigger #3, the signals from all the detectors were registered.

The other trigger was given by the scintillator placed at S2 (Trigger #1) which corresponded to ions that only arrived to the intermediate focal plane (S2). If the DAQ was triggered by Trigger #1, only the signals of the detectors of the first part of the experimental set up were registered. To avoid double counting events that arrived at the final focal plane, the Trigger #3 had higher priority than the Trigger #1. Trigger #1 was required for the determination of the number of incident particles in the secondary reaction target for the determination of the fragmentation cross sections.

Another important constraint in this experiment was the DAQ, because the maximum rate that could be processed by the system while keeping the dead time below 30 % was 1 kHz.

The difference in counting rates between both triggers could be very high, especially for those settings centered on the most exotic species, e. g., in the setting centered on ^{129}Ag , the counting rate at S2 was 21000 counts/s while the rate at S4 was 2500 counts/s. Because of this, Trigger #1, used for normalization, can be downscaled by different reduction factors (reduction factors up to 16 were used in this experiment).

4.2. Isotopic separation and identification of fission residues

As mentioned in the previous section, only the first section of the magnetic spectrometer was used for the separation and identification of the fission. The identification technique is based on the determination of the mass-over-charge ratio from the measurements of the magnetic rigidity and the reduced momentum of the transmitted nuclei. The magnetic rigidity was determined from the positions of the fragments in the intermediate focal plane. In principle, the determination of the rigidity in the first stage should be affected by the energy loss of the reaction products in the scintillation detector placed at S1. In our case, the energy loss was quite small, thus the difference in the value of the magnetic rigidity still allowed us to separate the reaction products. The reduced momentum was obtained from the time-of-flight measurement. The energy loss of the fission fragments in the ionization chamber

placed at S2 (MUSIC) provided the atomic number. The value of the atomic number was calibrated using the charge distribution of the fission fragments at low excitation energy, making it possible to identify the symmetric fission, corresponding to Pd.

However, the path length of all the fragments is not the same due to the different trajectories of the ions inside the spectrometer. Therefore, the calculated values of the mass-over-charge for the fragments show a clear dependence on the horizontal angle α_x which needs to be corrected in order to get the separation of the fragments (see Fig. 4.2). The horizontal angle α_x is determined from the measurement of the positions of the fragments by the TPCs, according to equation (4.1).

$$\alpha_x = \frac{X_i - X_j}{D_{ij}} \quad (4.1)$$

where $X_{i(j)}$ is the position of the fragment in the TPC $i(j)$ and D_{ij} is the distance between the two detectors.

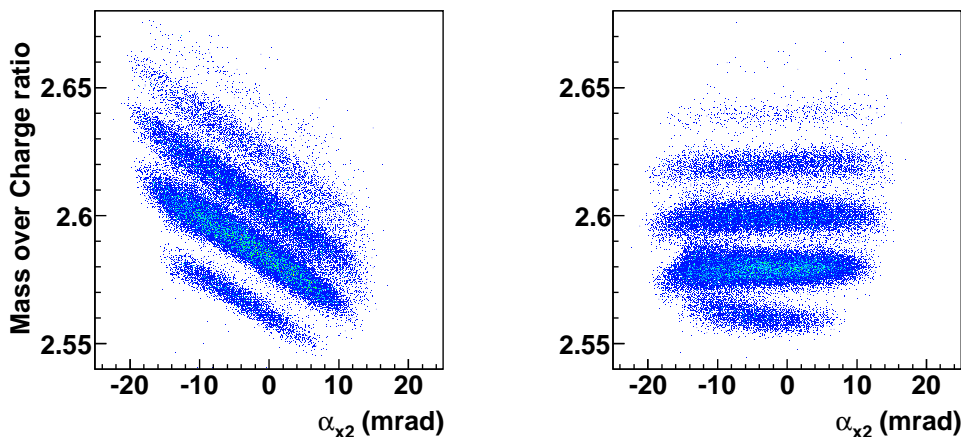


Figure 4.2: Left panel: Calculated mass over charge ratio versus the horizontal angle of the trajectories at the intermediate focal plane for the nuclei transmitted in a setting centered on ^{132}Sn . Right panel: Mass over charge ratio after the correction.

The isotopic identification of the fragments was obtained from the comparison of the position of the fission fragments in the focal planes of the spectrometer with calculated positions obtained with the LIESCHEN code [LIE].

Figure 4.3 shows the resolution achieved for the mass-over-charge ratio in the first part of the spectrometer for the tin isotopes (3.6×10^{-3} (FWHM))

for ^{132}Sn). We can see that the separation is good enough to make a clean selection of the fragments. The left panel in Figure 4.4 shows the identification matrix of all the fission residues arriving at the intermediate focal plane of the Fragment Separator for a magnetic setting centered on ^{132}Sn . The separation and identification of fission residues using the first part of the separator was achieved for the first time.

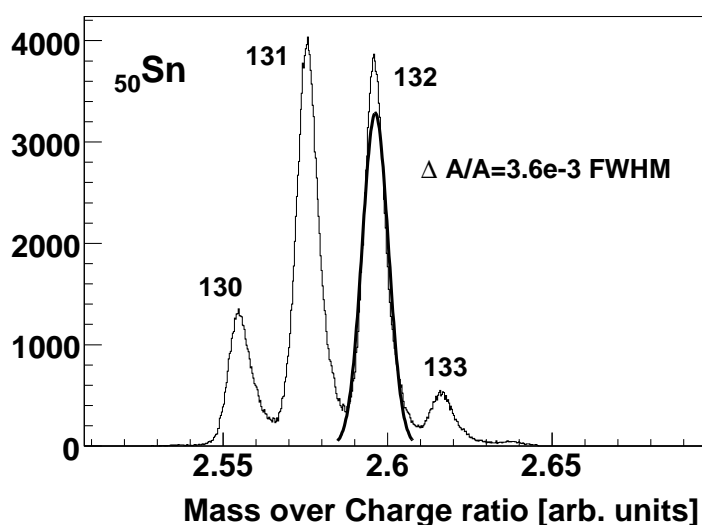


Figure 4.3: Distribution of mass-over-charge ratio of the fragments at $Z=50$.

4.3. Isotopic separation and identification of fragmentation residues

The identification of the fragmentation residues is done in the second part of the separator. The separation technique has already been described in Chapter 2 and is totally analogous to that of the first section of the separator, but with a longer path length for the time of flight. The right panel of Figure 4.4 shows all the fragments that arrive at the final focal plane after traversing the reaction target, placed at the intermediate focal plane, after the overlapping of several settings. Some isotopes will be fission fragments that have not undergone a reaction in the beryllium target, while others will be fragmentation products of the fission residues.

Nuclei coming from a reaction in the secondary target are selected by putting a condition in the identification matrix of the fission residues at the

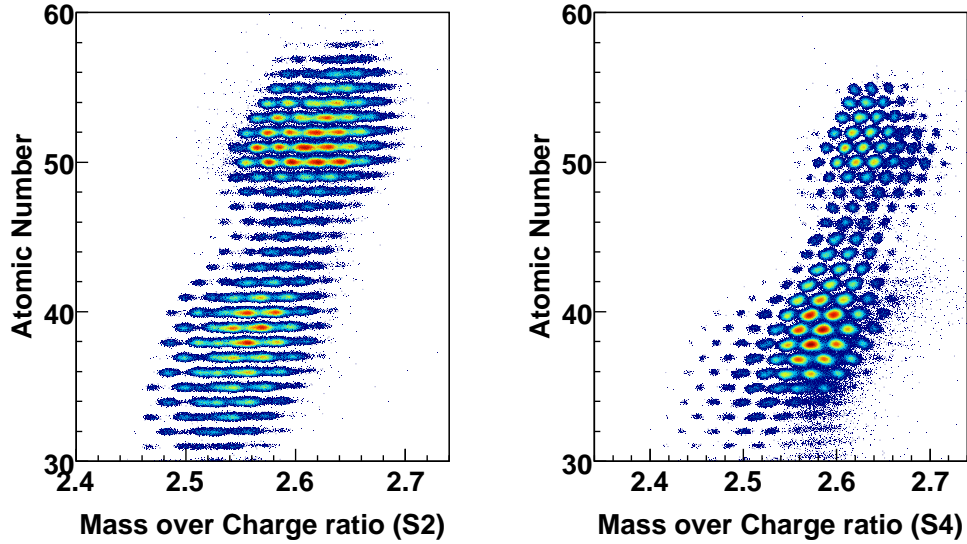


Figure 4.4: Left panel: Identification matrix of nuclei transmitted up to the intermediate focal plane of the Fragment Separator. Right panel: Identification matrix of nuclei identified at the final focal plane. This plot was obtained by overlapping different settings centered on ^{132}Sn , ^{131}In and ^{126}Ag .

intermediate focal plane, to clean it of the fragments not coming from the selected channel. Figure 4.5-left, shows the selected fragment while figure 4.5-right shows the fragmentation residues produced in the reaction of ^{132}Sn at 930 AMeV with beryllium from the overlapping of the different settings of the second half of the spectrometer. The one-, two- and three-proton removal channels are shown. Figure 4.6 shows a projection of the mass-over-charge ratios for each element ranging from In to Ru. We can see that the resolution and the background conditions are good enough to identify fragmentation residues with very few counts.

4.4. Determination of the fragmentation cross sections

In Chapter 3, we described how the cross sections are determined from the production yields of each nucleus, normalized to the number of projectiles and the thickness of the target (Eq. (4.2)).

$$\sigma(Z, A) = \frac{N(Z, A)}{N_p N_t} \cdot F \quad (4.2)$$

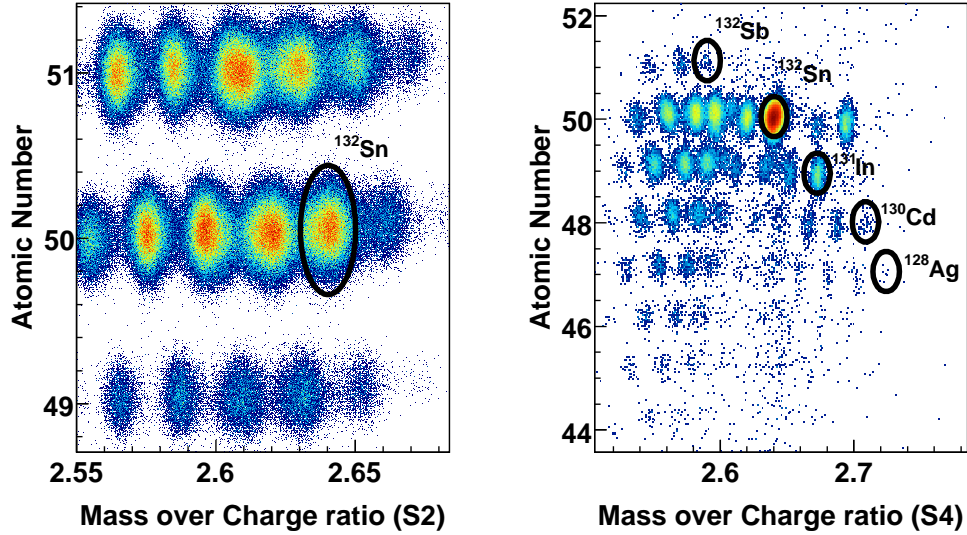


Figure 4.5: Left panel: Part of the identification matrix of nuclei identified in the intermediate focal plane of the Fragment Separator for a setting centered around ^{132}Sn . ^{132}Sn nuclei are marked by the black circle. Right panel: Identification matrix of the residual nuclei produced in the fragmentation of ^{132}Sn .

In this equation, $N(Z, A)$ is the number of counts of the nucleus with atomic number Z and mass number A . N_p represents the number of beam particles and N_t the number of particles in the target per unit area. The number of impinging projectiles is directly determined from the number of counts of the selected fragment in the identification matrix at the intermediate focal plane of the spectrometer, taking into account the two different trigger types and the downscaling factor of the trigger corresponding to fragments that do not reach the final focal plane. The factor F takes into account all the corrections that must be applied to correct the measured yields for losses produced by the experimental setup.

$$F = f_{eff} \cdot f_{tr} \cdot f_{sr} \quad (4.3)$$

where f_{eff} accounts for the efficiency of our detection system, f_{tr} corresponds to the angular transmission due to the limited angular acceptance of the spectrometer, and f_{sr} corrects the secondary reactions in the different layers of matter present in the beam line. Here we offer a brief description of the corrections applied.

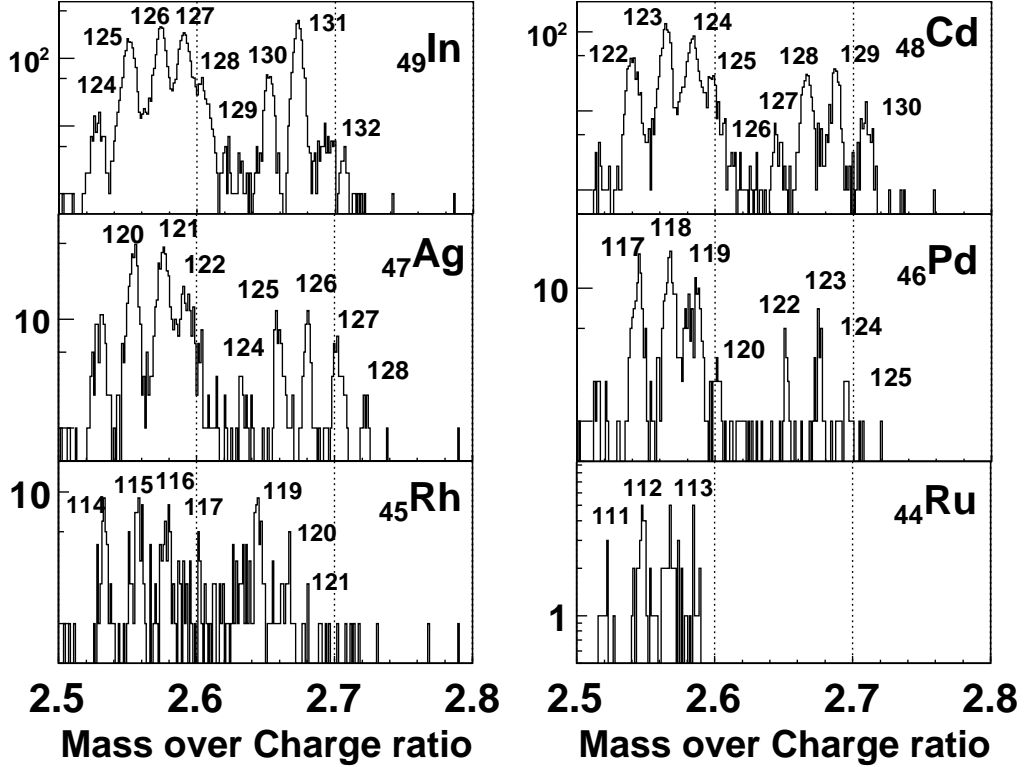


Figure 4.6: One-dimensional spectra of the projected A/Z for the different elements obtained in the fragmentation of ^{132}Sn on beryllium. Mass numbers are indicated for each peak.

4.4.1. Efficiency of the detection set-up

The detection efficiency is defined by the fraction of reaction products that were not registered by the detectors (see Chapter 3). The detection efficiency of the three scintillators and the MUSICs were estimated to be greater than 99%: the time projection chambers (TPCs) with an efficiency of 85%, were the limiting factor. This value was determined by comparing of the number of counts in the scintillators to the number of events with good values of the positions. However, in the experimental runs where the most intense beam was required, the MUSIC placed at S2 presented pile-up effects of the signals due to the very high counting rate of the fission fragments. The pile-up reduced the efficiency of the MUSIC from more than 99 % to only 46%.

| Nucleus | tr. (%) |
|-------------------|---------|-------------------|---------|-------------------|---------|-------------------|---------|
| ^{131}In | 100 | ^{126}Cd | 100 | ^{123}Ag | 100 | ^{117}Pd | 76.6 |
| ^{130}In | 100 | ^{125}Cd | 57.3 | ^{122}Ag | 89 | ^{121}Rh | 100 |
| ^{129}In | 100 | ^{124}Cd | 100 | ^{121}Ag | 100 | ^{120}Rh | 100 |
| ^{128}In | 100 | ^{123}Cd | 100 | ^{120}Ag | 100 | ^{119}Rh | 100 |
| ^{127}In | 100 | ^{122}Cd | 32 | ^{125}Pd | 67 | ^{116}Rh | 100 |
| ^{126}In | 100 | ^{129}Ag | 100 | ^{124}Pd | 100 | ^{115}Rh | 100 |
| ^{125}In | 99.6 | ^{128}Ag | 100 | ^{123}Pd | 100 | ^{114}Rh | 33.7 |
| ^{130}Cd | 100 | ^{127}Ag | 100 | ^{122}Pd | 25 | ^{113}Ru | 100 |
| ^{129}Cd | 100 | ^{126}Ag | 100 | ^{120}Pd | 100 | ^{112}Ru | 100 |
| ^{128}Cd | 100 | ^{125}Ag | 30 | ^{119}Pd | 100 | ^{111}Ru | 100 |
| ^{127}Cd | 100 | ^{124}Ag | 100 | ^{118}Pd | 100 | | |

Table 4.1: Transmission values from S2 to S4 calculated with the LIESCHEN code.

4.4.2. Angular and momentum transmission

The fragmentation residues produced in the intermediate focal plane of the Fragment Separator (S2), have to pass through the second part of the spectrometer, which is tuned to maximize the transmission of one of the desired fragments up to the final focal plane (S4). In the experiments, 6 different magnetic settings centered in ^{132}Sb , ^{132}Sn , ^{131}In , ^{123}Ag , ^{126}Ag and ^{129}Ag were used. However, in these settings, other fragments produced were not fully transmitted up to S4. In order to obtain the value of the cross section for these fragmentation products, the value of the transmission from S2 to S4 was evaluated using the code LIESCHEN [LIE]. Table 4.1 shows the transmission values calculated for the different settings. The systematic uncertainty associated to the transmission calculation is 10%.

4.4.3. Secondary reactions

This correction factor accounts for all the secondary reactions that may take place in the layers of matter different than the reaction target present in the beam line. The outgoing fragmentation residues of ^{132}Sn may undergo a secondary nuclear reaction before leaving the target or a reaction may occur in the detection system. These reactions will populate the neutron-deficient isotopes of the fragmentation residues, but they will not produce neutron-rich fragments. The calculation of the correction factor is explained in Section 3.1. Figure 4.7 shows the correction factor averaged for all the isotopes as a function of the atomic number of the fragment. The value of this factor results in a correction in a 26-30% correction of the final value of the cross

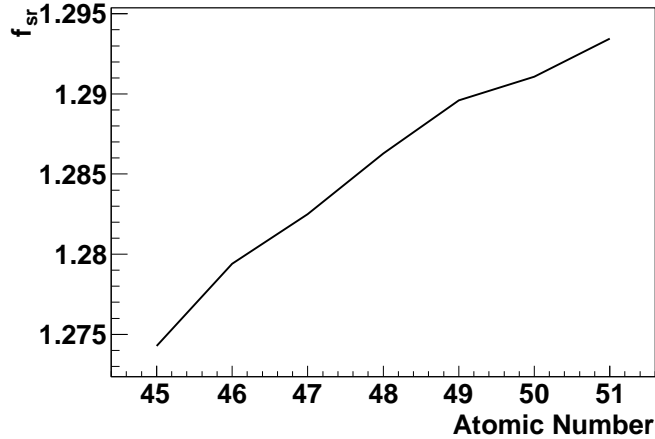


Figure 4.7: Correction factor f_{sr} for the layers of matter from the secondary target up to the final focal plane.

sections.

4.5. Results and discussion

Figure 4.8 shows the isotopic production cross sections of all the fragmentation residues measured in the fragmentation of ^{132}Sn on beryllium at 950 AMeV. The results of different model calculations are shown together with the data. As can be seen, 43 very neutron-rich In, Cd, Ag, Pd, Rh and Ru isotopes with cross sections as low as $5 \mu\text{b}$ were produced. The most neutron-rich nuclei that can be produced, which correspond to the proton-removal channels have been reached for In, Cd and Ag (^{131}In , ^{130}Cd and ^{129}Ag). In these reaction channels, only protons are abraded and the excitation energy gained remains below the neutron-evaporation threshold. The error bars are dominated by statistical uncertainties, due to the very low counting rates of some nuclei.

The results obtained were compared with two reaction codes: the semi-empirical parameterization EPAX [S00] and the COFRA code, an analytical version of the abrasion-ablation model [Ben99; COF], allowing us to benchmark the codes. EPAX describes rather well the production cross sections of residual nuclei that are not too different from the projectiles in mass number. However, for isotopes with a large neutron excess, EPAX clearly overestimates the production cross sections. The COFRA code provides a better overall description of the present data. Nevertheless, one can also

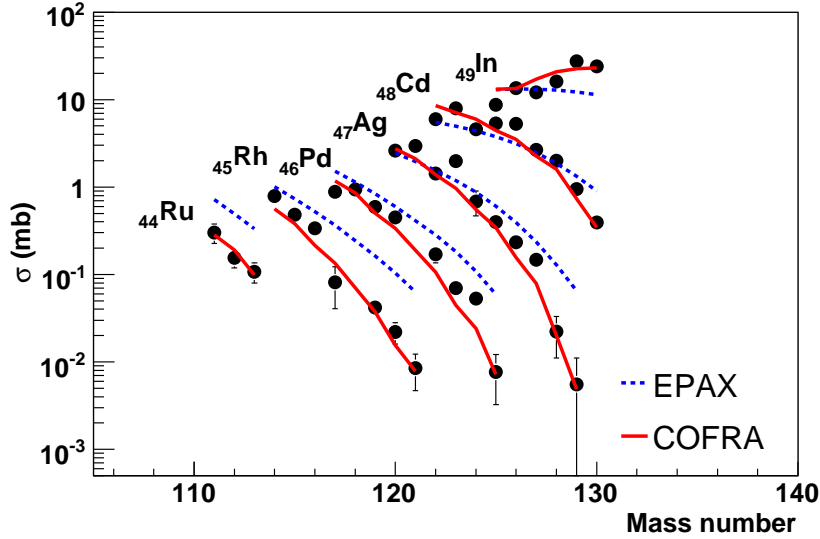


Figure 4.8: Isotopic distributions of the production cross sections of residual nuclei measured in the fragmentation of ^{132}Sn on beryllium. Error bars are shown if larger than symbols. The lines correspond to different model calculations EPAX[S00] (dashed line) and COFRA [Ben99] (solid line).

identify a clear tendency to slightly under-predict the production cross sections of neutron-rich residual nuclei with a large difference in mass number with respect to the projectile. It should be highlighted that the predictions of the COFRA code are extremely sensitive to the precise values of the neutron separation energies of the nuclei of interest, and that the neutron evaporation channel is the only decay channel considered in the code. The measured cross sections allowed us to validate the COFRA code. In fact, COFRA calculated cross sections will be used in the next chapter for the estimation of production yields of medium-mass neutron-rich nuclei.

4.5.1. Comparison with ^{136}Xe fragmentation results

In this section, we compare the isotopic production cross sections of In, Cd, Ag, Rh and Ru residues obtained in the fragmentation of ^{132}Sn on Be, with the results obtained in the fragmentation of ^{136}Xe using the same target [Ben08; Ord08]. The fragmentation of neutron-rich stable beams, has also been considered for the production of medium-mass neutron-rich nuclei. Figure 4.9 shows the production cross sections of In, Cd, Ag, Pd, Rh and Ru measured in the fragmentation of ^{136}Xe and ^{132}Sn at around 1 AGeV.

The COFRA calculations for both systems are shown for the Pd, Rh and Ru isotopes, in order to extrapolate the behaviour to larger neutron number.

These results show that the fragmentation of ^{132}Sn is a more competitive mechanism producing neutron-rich medium-mass secondary beams in the region between $Z=44$ and $Z=49$, due to the fact that the production cross sections are larger in the case of the ^{132}Sn compared to the ^{136}Xe beam for the most neutron-rich isotopes. In some cases, like e. g., Ag, this difference is up to five orders of magnitude larger for the tin beam with respect to the xenon beam. The agreement of the data with the calculations is rather good. However, the COFRA calculations for xenon slightly underestimate the cross sections for fragments several charges far from the projectile.

In order to estimate final production yields of neutron-rich nuclei with both systems, the productions mechanisms of these nuclei have to be taken into account. The fragmentation residues of xenon will be produced using in-flight technique, while the ^{132}Sn beam is prepared in ISOL targets, so the extraction and beam preparation efficiencies have to be taken into account. However, the intensity of the primary beam available for ^{136}Xe is lower than that which can be produced for the ^{132}Sn using ISOL technique. These items will be discussed in the next chapter.

These data can also be used to investigate some properties of medium-mass neutron-rich nuclei, such as the presence of neutron skins. Indeed, one would expect that a neutron skin would hinder the production cross sections for the proton removal channels in the nucleus of interest. In Figure 4.10 we compare the proton removal channels cross sections for ^{136}Xe and ^{132}Sn , looking for a possible neutron skin in the ^{132}Sn . The experimental data show no differences, so we cannot conclude whether the ^{132}Sn presents a neutron skin or not. However, The COFRA calculation shows a lower value for the proton removal cross sections of the ^{132}Sn than the ^{136}Xe .

4.6. Conclusions

In this chapter, we investigated the production cross sections of the residual nuclei produced in the fragmentation of ^{132}Sn on Be. The ^{132}Sn secondary beam was produced in the fission of a 950 AMeV ^{238}U beam after impinging onto a lead target. We have used the Fragment Separator as two independent spectrometers, in order to identify the fission fragments in the first stage and their fragmentation products in the second stage. The resolution achieved in the first stage, made it possible to separate and identify fragments with masses around $A \sim 130$ for the first time, by using only half of the spectrometer with a time-of-flight measurements over 18 m. We have presented

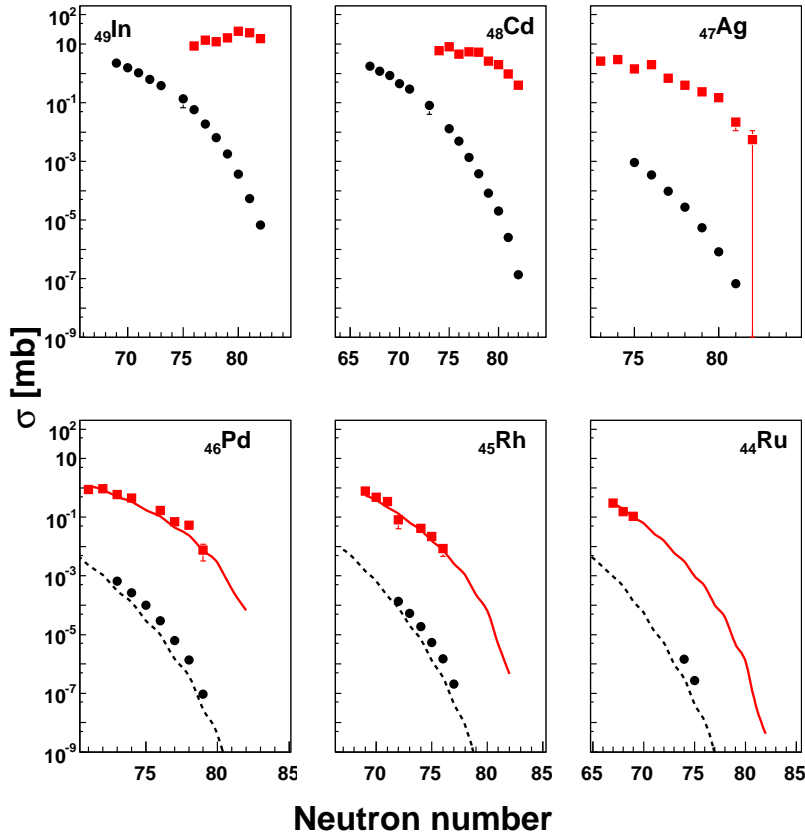


Figure 4.9: Isotopic distributions of the production cross sections of residual nuclei produced by the fragmentation of ^{132}Sn (squares) and ^{136}Xe (circles) in beryllium. The lines correspond to COFRA calculations.

the production cross sections of the residual nuclei produced in the fragmentation of ^{132}Sn , proving the feasibility of using post-accelerated neutron-rich fission fragments in order to produce very neutron-rich medium-mass nuclei. The data obtained allowed us to benchmark the EPAX and COFRA codes. The EPAX formula overestimates the cross sections, especially for those fragments with large differences in mass number with the projectile. The COFRA code provided a better overall description of the experimental data, but with a slight underestimation of the productions of the fragments with moderate number of neutrons. We have thus validated the COFRA code for their use in the estimation of production yields in the next chapter. We have also compared our results with the data obtained in the measure-

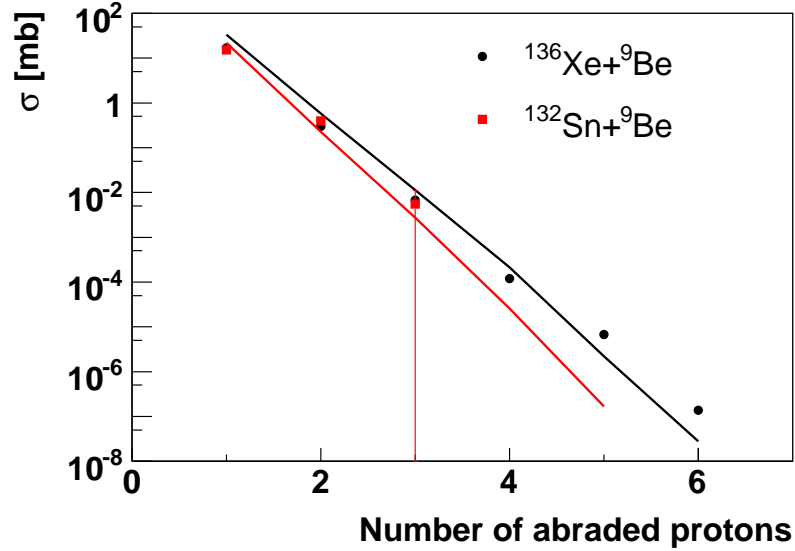


Figure 4.10: Cross sections of the proton removal channels measured in the fragmentation of ^{136}Xe (black circles) and ^{132}Sn (grey squares) on Be. The lines correspond to COFRA calculations.

ment of the fragmentation of ^{136}Xe , showing that fragmentation of ^{132}Sn is a more competitive mechanism for producing neutron-rich medium-mass secondary beams of elements in the region between $Z=44$ and $Z=49$. Finally, we have compared the cold fragmentation channels of both projectiles in order to investigate the existence of a neutron skin in the ^{132}Sn , but the data do not show any effect.

Chapter 5

Production of medium-mass secondary beams in future RIB facilities

In this chapter we will use the results obtained in the previous chapters to estimate the production yields of medium-mass neutron-rich nuclei in future Radioactive Ion Beam Facilities (RIBFs), namely EURISOL and FAIR. As it was presented in Chapter 1, these are two of the next generation RIBFs to be constructed in Europe. In the EURISOL project, the exotic beams will be produced by the ISOL technique, while the FAIR facility will use the in-flight method. In both cases, medium-mass neutron-rich nuclei will be produced from the fission of actinides, but in a different energy regimes. The EURISOL project will take profit from the fission at low excitation energy, while the FAIR facility will use fission at higher excitation energies. In the next subsections the production mechanisms used in both facilities will be described, together with the production yields. The results obtained for EURISOL could be eventually extrapolated to the Spiral II facility by scaling the difference in fission rate induced by the drivers and taking into account the differences in both setups.

5.1. The FAIR facility

FAIR (Facility for Antiproton and Ion Research) is an international accelerator facility of the next generation. It builds on the experience and technological developments already made in the existing GSI facility and incorporates new technological concepts. The currently foreseen layout is shown in Figure 5.1. The existing GSI accelerators will serve as injector for

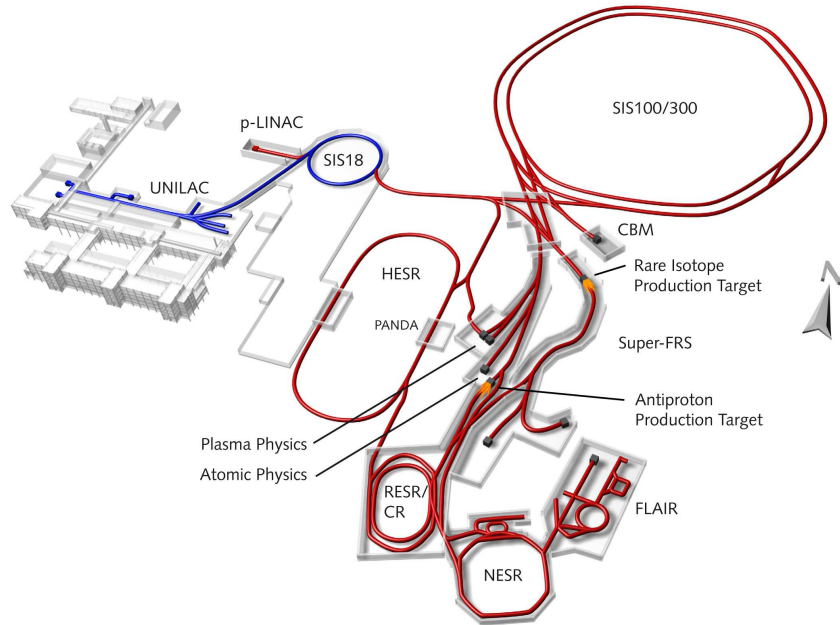


Figure 5.1: Schematic picture of the FAIR facility. The existing GSI facilities are shown in dashed lines. Solid lines show the new accelerator and the new experimental areas.

the new facility. A superconducting double synchrotron SIS100/300 with a circumference of 1100 m and magnetic rigidities of 100 and 300 Tm will serve as the main accelerators. Adjacent to the large double synchrotron is a complex system of storage cooler rings and experiment stations, including a superconducting nuclear fragment separator (Super-FRS). FAIR will supply rare isotope beams of an intensity and quality unprecedented for in-flight facilities.

The driver accelerator

The accelerator system will provide primary beams with intensities increased by a factor of up to several hundred for the heaviest ion species compared to the present installations¹. For the production of radioactive secondary beams, the high intensity beams circulating in the SIS100-synchrotron will be compressed to short bunches of 50-100 ns (fast extraction mode). The goal is to achieve an intensity of $5 \cdot 10^{11}$ ions/s for uranium beams (charge state $q=28+$) at 1.5 A GeV. This increase in primary intensity translates into an

¹The maximum intensity for ^{238}U at 1 AGeV available at GSI is $\sim 3 - 4 \cdot 10^9$ ions/s

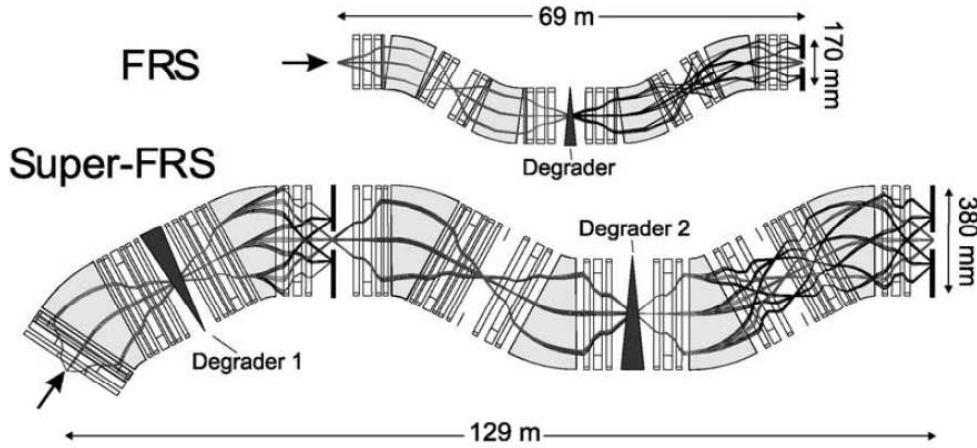


Figure 5.2: Comparison of the layout of the FRS and the Super-FRS.

even higher gain factor, from 1000 to 10000 for the secondary radioactive beam intensities, due to the higher acceptances of the separator and storage rings.

The production targets

Production targets must be able to cope with the high power deposited by the primary beam (12 kW in slow extraction mode, less than 200 GW for fast extraction [Win07]). Therefore, an appropriate cooling system is needed. Depending on the working mode of the accelerator, different cooling systems are foreseen. In the slow-extraction mode, the intensities of 10^{12} particles/s can be distributed almost continuously, therefore, a cooling rotating wheel will be enough. However, in the fast extraction mode, 10^{12} particles per pulse will be available, with a pulse length of 50 ns. The enormously large power deposition in the target, will increase the temperature to more than 10^4 K, which exceeds the melting point of any solid material. Possible solutions for overcoming this limitation are to increase the beam spot in the y direction or to use a windowless liquid lithium target [Nol03].

The Super-FRS

The Super-FRS is a large-acceptance superconducting fragment separator followed by different experimental branches.

Figure 5.2 shows a layout of the Super-FRS compared to the existing FRS. The Super-FRS is optimized for the transmission of fission fragments from a primary uranium beam, therefore fragmentation residues of different

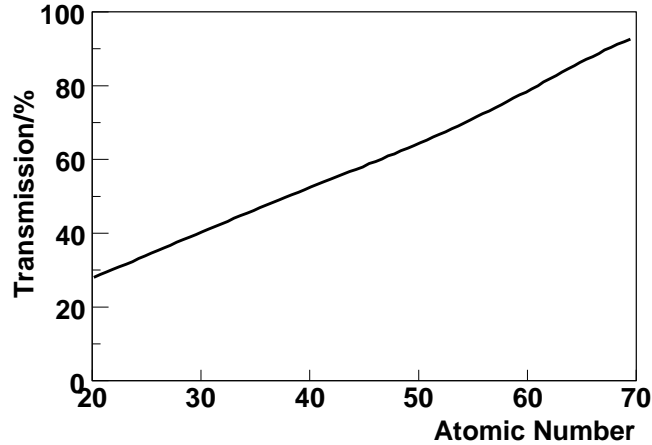


Figure 5.3: Average transmission through the Super-FRS versus atomic number of uranium fission fragments. Data taken from [Gei03].

nuclei will also be transmitted. Due to the relatively large amount of energy released in the fission reaction, the products will populate a large phase-space and therefore larger acceptances will be required. The momentum acceptance in the Super-FRS will be $\pm 2.5\%$ and the angular acceptances will be ± 40 (horizontal) and ± 20 mrad (vertical). Along with these improvements in the geometry, a new separator concept with two independent separation stages (pre- and main- separator) with two independent degraders is considered. This two-stage concept will allow to cope with high production rates due to an efficient background suppression.

Figure 5.3 represents the average transmission as a function of the atomic number of the uranium fission fragments. The transmission values of the fission fragments range from 30% for the lightest fission residues up to 90% for the heaviest. Values are taken from [Gei03].

5.2. Production yields at FAIR

In order to estimate the production yields of neutron-rich fission fragments in the Super-FRS, we used the cross sections obtained with the beryllium target and their extrapolations for large neutron excess, which were presented in Chapter 3. The beryllium target will enhance the fission induced by nuclear reactions. In all the calculations, we have assumed a ^{238}U beam with an intensity of 10^{12} ions per second impinging onto a 1 g/cm^2 Be target at the entrance of the super-FRS. To obtain the final production

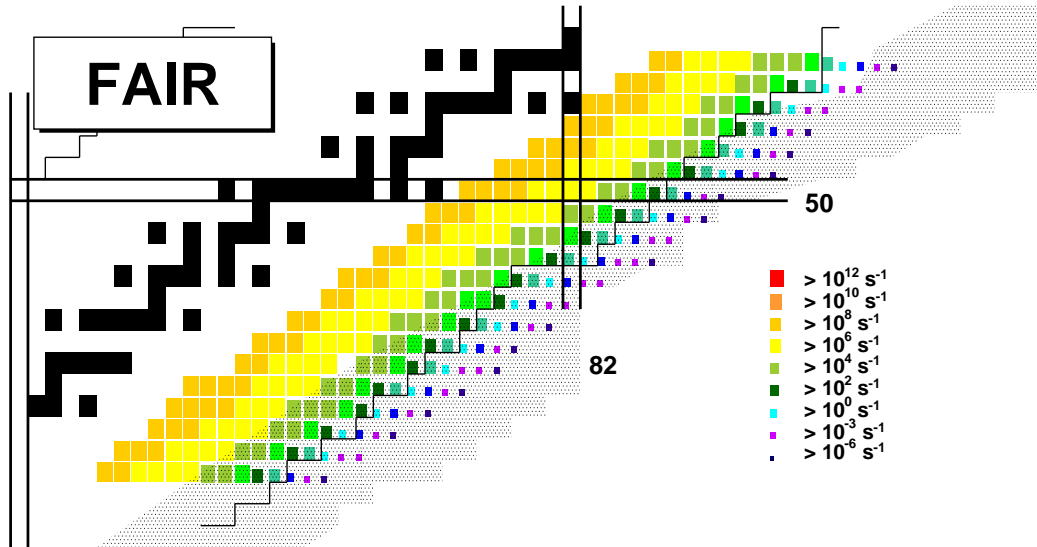


Figure 5.4: Expected production rates in the Super-FRS from beryllium-induced fission of ^{238}U at relativistic energies with a beam intensity of 10^{12} ions/s impinging onto a $1\text{g}/\text{cm}^2$ Be target. The color scale represents the different production rates. See text for details.

rates, after traversing the whole separator, the angular transmission has been taken into account. Figure 5.4 shows the expected productions yields of the neutron-rich fission fragments at FAIR on top of the chart of nuclides. The color scale corresponds to different production rates in nuclei per second. The shadowed area corresponds to the r-process path in stellar nucleosynthesis. We observe that with in-flight fission we can cover a wide range of medium-mass fragments from Rb to La. The expected yields range from 10^{10} ions per second to 10^{-6} ions per second for the most neutron-rich isotopes. Nuclei with yields lower than this value are not shown. The picture also shows that an important fraction of the medium-mass r-process nuclei is covered with rather high intensities.

5.3. The EURISOL facility

EURISOL facility is a next-generation ISOL facility to be constructed in Europe. The aim is to produce exotic radioactive ion beams with intensities many orders of magnitude greater than those available today using the ISOL technology. This facility will offer two different production modes depending on the target used, a multi-MW production mode using a spallation target to produce neutrons in order to induce fission of actinides, and a 100 kW-mode

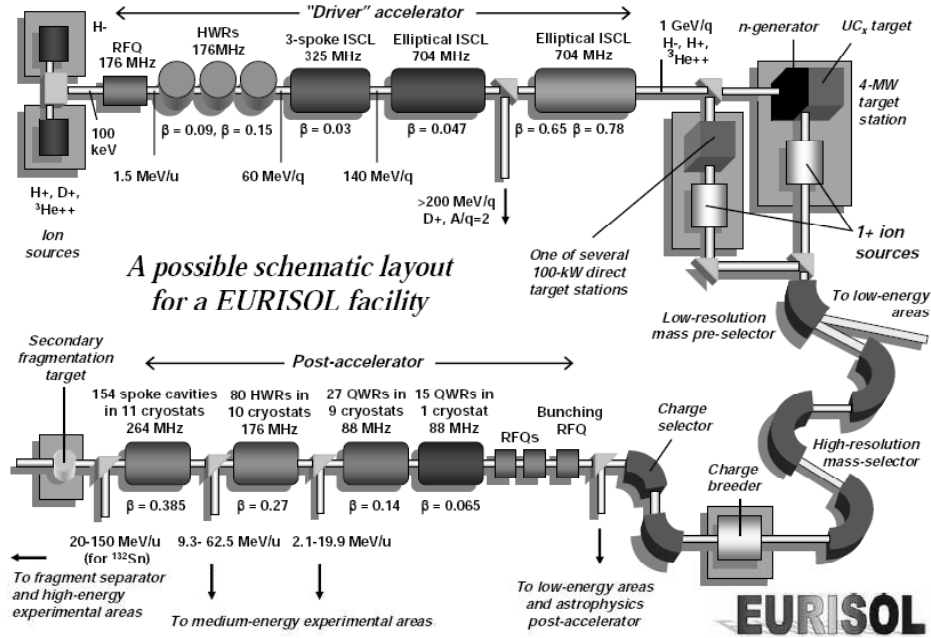


Figure 5.5: Schematic diagram of EURISOL layout.

with direct production from spallation/fragmentation reactions. In the section devoted to the production targets this will be explained in more detail.

Figure 5.5 is a layout of the EURISOL facility, showing its main parts: the accelerator driver, the two production targets, ion sources, the mass separator, and the post accelerator.

The driver accelerator

The driver accelerator at EURISOL will be a superconducting linear accelerator (LINAC) with 5 different sections: the injector, the low- β section, the medium- β section, the high- β section and a high-energy beam transport section. This accelerator will be able to accelerate protons up to 1 GeV, ${}^3\text{He}^{2+}$ ions at 2 GeV and deuterons to less than 300 MeV. The intensity of the proton beam will reach 5 mA for the multi-MW production mode and 0.1 mA for the 100 kW production mode.

The production targets

As already mentioned, two different types of production targets will be used in this facility. The multi-MW target station is a two-step target de-

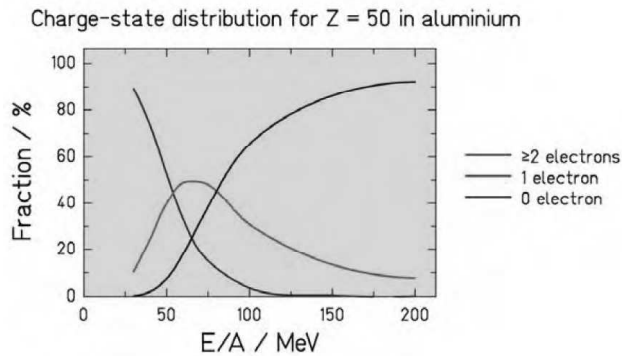


Figure 5.6: Charge state probabilities of Sn projectiles after penetrating a thick aluminium layer as a function of the energy.

signed for a 4 MW proton beam. It uses a liquid metal (Hg) converter target to transform the proton beam to a neutron flux. The neutrons will hit five or six surrounding actinide targets for producing fission fragments. The other production targets will operate with a 100 kW proton beam for the direct production of elements that cannot be obtained from fission via spallation and fragmentation reactions.

The post accelerator

The EURISOL post accelerator is a high-energy, heavy-ion machine, with a nominal design based on $^{132}\text{Sn}^{25+}$ up to an energy of 150 AMeV. The accelerator consists of a superconducting LINAC based on different cavity families with the possibility of having a stripper during the acceleration stages through the LINAC (Fig. 5.5).

The selected energy, 150 AMeV, is a compromise between the physics goals and the cost of the accelerator. The production of neutron-rich nuclei is similar down to energies around 200 AMeV.

Another factor to define the energy of the post-accelerator is the charge state distribution. Figure 5.6 shows the ionic charge-state distribution for Sn at different beam energies. We see that for energies below 100 AMeV, the probability of having charge states is significant, around 30 % for the 1 electron. The purity secondary beam will then be spoiled by the contamination of different charge states. In fact, when dealing with neutron-rich fragments, the charge states of the less-neutron rich elements, which are more abundantly produced, will also be transmitted through the separator. Therefore 150 AMeV is a good value for the post-acceleration energy, with less than a 20% probability of contamination from charge states.

5.4. Production yields at EURISOL

In the EURISOL facility, medium-mass neutron-rich nuclei will be produced from two different mechanisms, fission of uranium in a UC_X thick target and fragmentation of post-accelerated fission residues. In this section both methods will be presented in detail.

5.4.1. Production in fission

Fission will be induced by neutrons with energies around a few MeV. These neutrons will be produced by the 1 GeV proton beam with a very high intensity (5 mA) impinging onto a liquid-metal target-converter. The left panel in Figure 5.7 shows the calculated neutron spectrum produced in a liquid mercury target-converter from a 1 GeV proton beam [HM06]. In the right panel we present the fission yields of ^{238}U for the different neutron energies obtained from the combination of the neutron spectrum and the neutron-induced fission cross sections found in the EXFOR database [EXF]. This curve presents two peaks, one around 2 MeV, which corresponds to the *first chance* fission and another one at 6-7 MeV, which corresponds to the *second chance* fission, after the evaporation of one neutron. This means that the fissioning system will be ^{239}U in the first case and ^{238}U in the second.

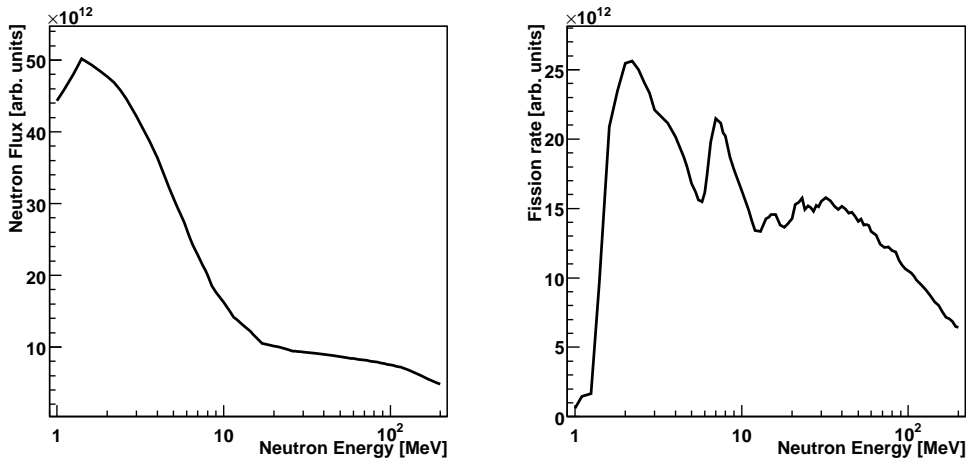


Figure 5.7: Left panel: Calculated neutron flux spectrum for a liquid mercury target in the Multi-MW target station at EURISOL. Right panel: Calculated fission rate for ^{238}U induced by the neutron spectrum shown in the left panel.

In Chapter 3, we explained that the excitation energy distribution induced by electromagnetic interaction in the reaction $^{238}\text{U}+\text{Pb}$ at 950 A MeV

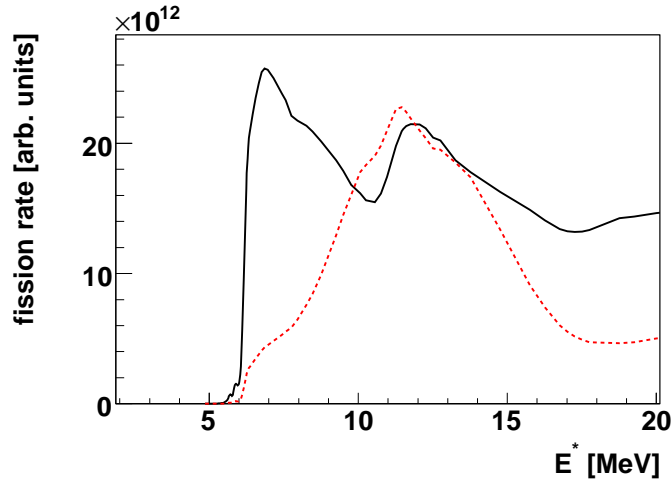


Figure 5.8: Fission rate versus excitation energy for neutron induced (solid line) and Electromagnetic (dashed line) fission.

has its maximum around 10-13 MeV. In the case of neutron-induced fission, the maximum of the distribution occurs around 2 MeV for the neutron energy. By adding the 4.76 MeV energy released in the neutron capture by ^{238}U , the two excitation energy distributions differ by a few MeV (see Fig. 5.8). Consequently, rather similar yields and isotopic distributions could be expected for the fission residues.

Based on this, in a first approximation we can use the results of the isotopic distributions of fission residues obtained with the lead target in Chapter 3 to estimate the in-target production yields of neutron-rich fission fragments with the Multi-MW EURISOL target. In order to do so, we have normalized the the measured isotopic production cross sections, and their extrapolations to large neutron excess, to the total fission cross section of ^{238}U on lead $\sigma_f \approx 3.8$ b [Jur04]. The final production yield in particles per second has been calculated assuming a fission rate of 10^{15} fissions/s in the UC_X target [EUR09a].

The upper panel of Figure 5.9, shows the calculated in-target isotopic production yields of neutron-rich fission fragments between Ba and Rb on top of the chart of nuclides. The different production rates are represented by the color scale and the sizes of the boxes. The scale ranges from 10^{-6} ions per second for the most neutron-rich isotopes up to 10^{12} ions per second. Nuclides with production rates lower than 10^{-6} are not shown. We see that from the fission of ^{238}U , we can cover the medium-mass neutron-rich region of the nuclide chart from elements ranging from Ba to Kr with very high

production yields. In order to get final useful yields, extraction and ionization efficiencies must be taken into account.

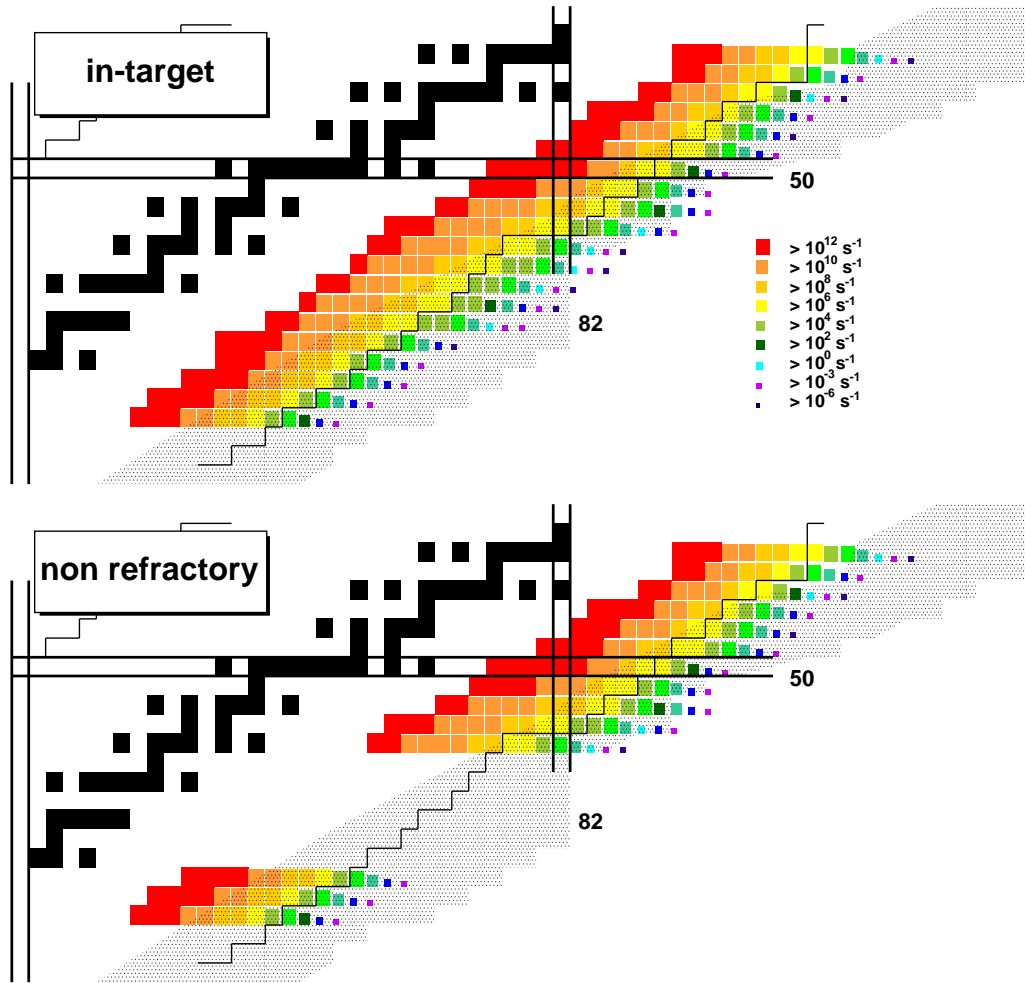


Figure 5.9: Top panel: Calculated in-target production yields in the fission target at future EURISOL facility for a fission rate of 10^{15} fissions/s. The dotted area represents the r-process path. Bottom panel: Same as top panel, but those elements which have never been extracted from ISOL targets have been removed.

The extraction efficiency depends on the chemical properties of the elements. Indeed, not all elements produced can be released from the target with high efficiencies. In fact, the elements between Zr and Rh, known as *refractory metals* due to their very high boiling points, cannot be extracted from ISOL targets at all with the present technology. Pd and Ag isotopes also have very poor extraction efficiencies.

| Nucleus | ε (%) | Nucleus | ε (%) | Nucleus | ε (%) |
|-------------------|-------------------|------------------|-------------------|------------------|-------------------|
| ^{130}Sn | 50 | ^{95}Kr | 7 | ^{85}Ga | 2 |
| ^{131}Sn | 44 | ^{96}Kr | 6 | ^{86}Ga | 1 |
| ^{132}Sn | 42 | ^{97}Kr | 5 | ^{70}Ni | 40 |
| ^{133}Sn | 9 | ^{98}Kr | 4 | ^{71}Ni | 15 |
| ^{134}Sn | 7 | ^{81}Ga | 26 | ^{72}Ni | 8 |
| ^{135}Sn | 3 | ^{82}Ga | 18 | ^{73}Ni | 3.5 |
| ^{136}Sn | 2 | ^{83}Ga | 11 | ^{74}Ni | 3.5 |
| ^{137}Sn | 1 | ^{84}Ga | 3 | ^{75}Ni | 0.83 |

Table 5.1: Extraction efficiencies for Sn, Kr, Ga and Ni isotopes [EUR09b].

In the bottom panel of Figure 5.9 the same production yields as in the upper panel are shown, but without the nuclei which have never been extracted from ISOL targets due to their refractory nature. We see that even though many medium-mass neutron-rich nuclei are produced, some of them cannot be extracted from the production target in a conventional ISOL facility. Because of this fact, the alternative presented in the next section is proposed.

Release efficiencies in ISOL targets were parameterized [Luk06] according to Equation (5.1):

$$\varepsilon(t_{1/2}) = \frac{\varepsilon_s}{1 + (t_{1/2}/t_0)^\alpha} \quad (5.1)$$

where ε_s , t_0 and α are three parameters that depend on the selected element, and $t_{1/2}$ is the half life of the isotope. We have calculated the extraction efficiencies of the elements whose parameters were available in [Luk06]: Rb, Sr, Cd, I, Cs and Ba. For isotopes with no experimental value of the half-life available, we used the calculated values from Möller *et al.* [Möl03].

Table 5.1 presents the release efficiencies used to calculate the estimated yields of those elements with no parameters available. These release efficiency values were taken directly from [EUR09b]. The values of the efficiencies range from the 50% of the ^{130}Sn to values as low as the 0.83% of the ^{75}Ni . All the efficiencies of the nuclei used in this work will be presented in Appendix D.

Figure 5.10 is a comparison of production yields in the EURISOL fission target, before and after correcting from extraction efficiency for Rb, Sr, Cd, I, Cs and Ba. As it can be seen, the values of the extraction efficiencies, depend significantly on the elements and decrease with the neutron number. For Sr and Ba, the ratio between the in-target production and the extracted yield is around a factor 10^3 , independently of the isotope, while for elements

such as I, the efficiency is close to 100 % for the light isotopes and decreases with the mass number, but not so significantly as cadmium does.

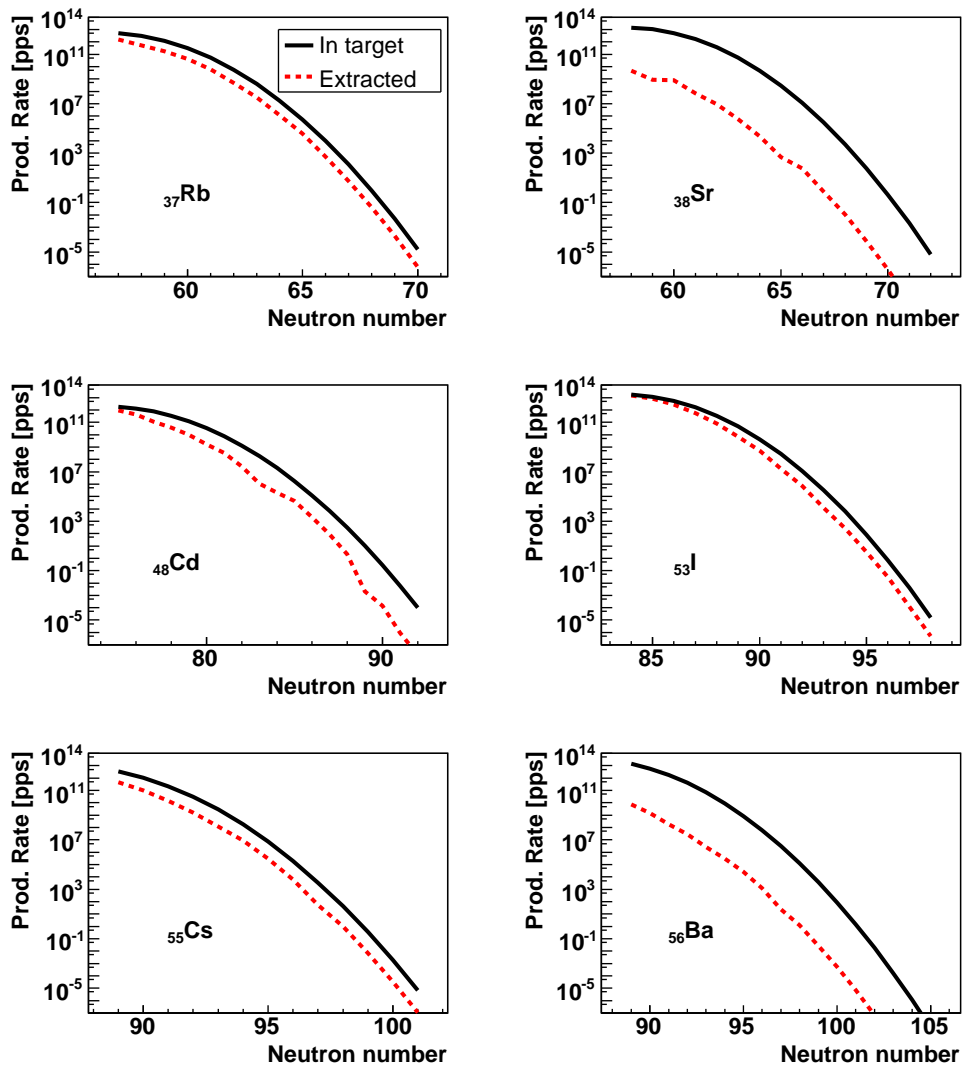


Figure 5.10: Production yields in-target (solid line) and after correction for the extraction efficiency from the fission target (dashed line).

5.4.2. Two-step reaction scheme

The EURISOL facility will take advantage of the extremely high fission rate to produce medium-mass neutron-rich nuclei, except for the refractory elements, between Zr and Rh. A two-step reaction scheme has been proposed [Hel03], as a way to overcome this limitation and produce these elements also. According to this idea, intense beams of neutron-rich nuclei could be produced by re-accelerating non-refractory fission residues such as ^{132}Sn , which are produced in the ISOL target. These neutron-rich projectiles could then be fragmented to produce even more neutron-rich nuclei, covering the refractory elements gap.

The results from the fragmentation of the ^{132}Sn (Chapter 4) validated the COFRA code [Ben99]. Although the cross sections were measured at high energies of the projectile (~ 900 AMeV), the production cross sections of lighter residues and more neutron-rich isotopes is not influenced by the energy of the projectile [Ord08; EUR09b]. Only the neutron-deficient residues close to the initial projectile will present higher yields with the lower energies proposed for the acceleration stage [Ord08; EUR09b]. Based on this facts, we can calculate fragmentation cross sections for neutron-rich fission fragments using this code. With these cross sections we can estimate the expected production yields of medium-mass neutron-rich nuclei in a two-step scenario. For these calculation, we need to know not only the cross sections, but also the intensities of the fission-fragments and thickness of the fragmentation target.

For the estimation of the post accelerated fission fragments beam intensities, some factors have to be taken into account: the release efficiency from the production target, the ionization efficiency of the ion sources and the transport and charge breeding efficiencies for the post-acceleration. In our calculations, a total beam preparation efficiency of 10%, including beam transport and charge breeding, has been assumed.

The target thicknesses considered in the following yield calculations are 20% of the range of the projectile in Be at 150 AMeV. This target thickness was selected as a compromise between the improving the probability of having a nuclear reaction, keeping the probability of multiple reactions in the target low.

Several ions have been considered as projectiles, especially those with very good release efficiency from the ISOL target. Table 5.2 shows all the considered nuclei as projectiles with their corresponding beam intensities and target thicknesses. These projectiles will allow us to cover the whole range of medium-mass nuclei, filling in the gaps for those elements that cannot be extracted from ISOL targets at present.

| Ion | Intensity (pps) | thickness (mg/cm ²) | Ion | Intensity (pps) | thickness (mg/cm ²) | Ion | Intensity (pps) | thickness (mg/cm ²) |
|-------------------|-----------------------|---------------------------------|-------------------|----------------------|---------------------------------|------------------|----------------------|---------------------------------|
| ¹⁵¹ Ba | 2.63×10 ³ | 211 | ¹³⁷ Sn | 5.96×10 ⁴ | 250 | ⁸⁵ Ga | 8.20×10 ³ | 350 |
| ¹⁴⁷ Cs | 1.69×10 ⁸ | " | ¹³⁰ Cd | 2.76×10 ⁶ | 250 | ⁸⁶ Ga | 2.30×10 ³ | " |
| ¹⁵⁰ Cs | 2.94×10 ⁴ | " | ⁹⁵ Kr | 3.97×10 ⁷ | 300 | ⁷⁰ Ni | 7.10×10 ⁵ | 420 |
| ¹³⁰ Sn | 3.55×10 ¹¹ | 250 | ⁹⁶ Kr | 2.20×10 ⁷ | " | ⁷¹ Ni | 3.60×10 ⁵ | " |
| ¹³¹ Sn | 2.76×10 ¹¹ | " | ⁹⁷ Kr | 3.60×10 ⁵ | " | ⁷² Ni | 1.90×10 ⁵ | " |
| ¹³² Sn | 1.39×10 ¹¹ | " | ⁹⁸ Kr | 3.09×10 ⁵ | " | ⁷³ Ni | 6.80×10 ⁴ | " |
| ¹³³ Sn | 9.36×10 ⁹ | " | ⁸¹ Ga | 5.10×10 ⁷ | 350 | ⁷⁴ Ni | 3.20×10 ⁴ | " |
| ¹³⁴ Sn | 1.37×10 ⁹ | " | ⁸² Ga | 1.80×10 ⁷ | " | ⁷⁵ Ni | 2.90×10 ⁴ | " |
| ¹³⁵ Sn | 4.42×10 ⁷ | " | ⁸³ Ga | 2.40×10 ⁶ | " | | | |
| ¹³⁶ Sn | 4.44×10 ⁶ | " | ⁸⁴ Ga | 2.30×10 ⁶ | " | | | |

Table 5.2: Secondary beam intensities and target thicknesses in a two-step reaction scenario.

In the next sections, we will discuss the production of medium-mass neutron-rich nuclei using a two step reaction scheme. We have divided up the discussion by different mass regions: the refractory gap, the region between Sn and Cs and the region of elements below Sr.

Producing very neutron-rich nuclei between Rh (Z=45) and Zr (Z=40)

The fragmentation of two different projectiles, ¹³²Sn and ¹³⁰Cd, has been investigated as a possibility for covering this gap. ¹³²Sn has a very good release efficiency, and its production in low-energy fission is favoured because it is doubly-magic. ¹³⁰Cd is closer to the desired elements, therefore higher production cross sections from fragmentation are expected.

The calculated yields are shown in Figure 5.11 for elements from Pd to Sr which are covered by both projectiles. We see that by using both projectiles we can produce very neutron-rich nuclei, especially from the proton-removal channels, where only protons are abraded in peripheral collisions. The excitation energy introduced in the system is so low that neutrons are not evaporated. Yields are higher for ¹³²Sn than for ¹³⁰Cd, especially for heavier elements in this region. For example, in the case of Pd, the difference in yield for the most neutron rich isotope ¹²⁸Pd is near of one order of magnitude. This difference is also seen in elements such as Rh and Ru. For lighter elements and ¹³²Sn projectiles, the yield decreases rapidly as the neutron number increases. Thus the yields using both projectiles are rather similar for the proton removal channels. In the case of the less neutron-rich isotopes,

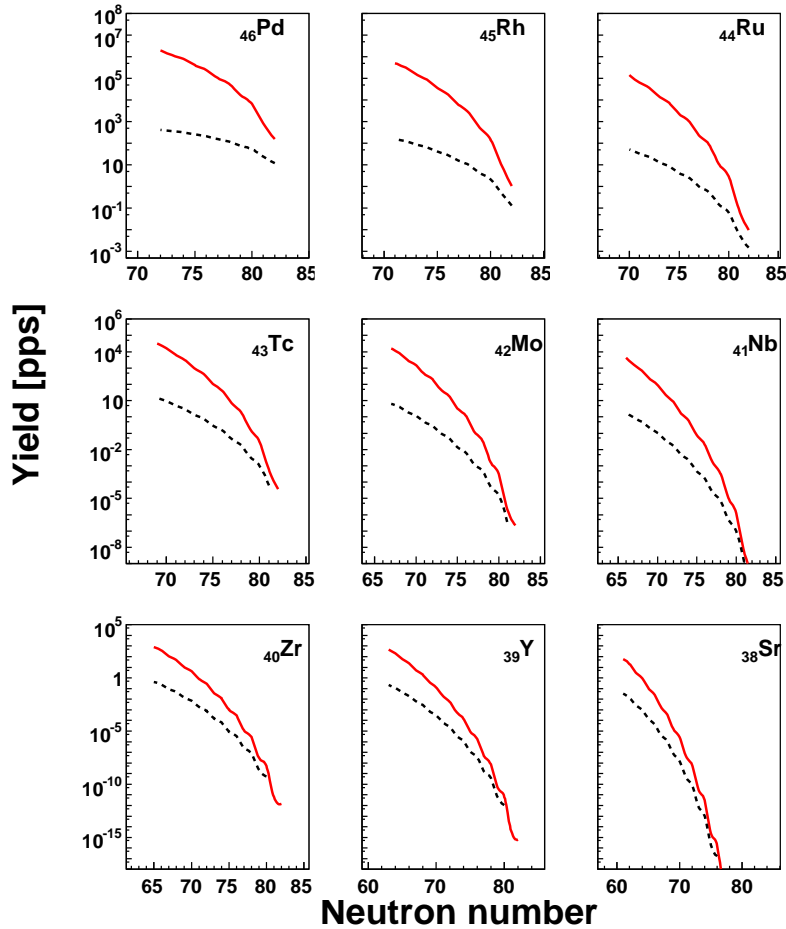


Figure 5.11: Production yields obtained in the fragmentation of ^{132}Sn (solid line) and ^{130}Cd (dashed line).

the higher intensity available for the ^{132}Sn secondary beam (1.4×10^{11} ions per second) compensates the difference in production cross sections when compared to the Cd beam (2.76×10^6 ions per second). A similar behaviour is expected for other isotopes of these elements, due to the difference in the primary beam intensities. From these results, we can conclude that the best option for the production of nuclei in this region is the fragmentation of tin isotopes produced in fission.

Figure 5.12 shows the production rates obtained from the fragmentation of neutron-rich Sn isotopes. The left panel presents the production rates in the fragmentation of ^{132}Sn on beryllium. The right panel displays the production rates obtained from the fragmentation of all the tin isotopes between

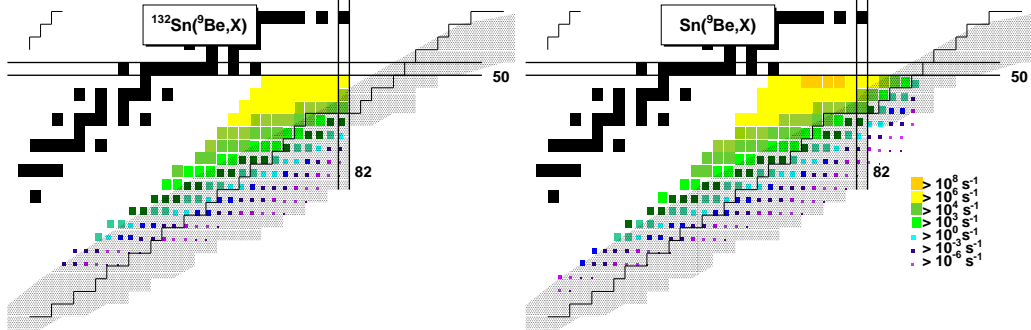


Figure 5.12: Production yields in the fragmentation of Sn isotopes produced in fission on top of the chart of nuclides. The left panel corresponds to fragmentation of ^{132}Sn . The right panel corresponds the fragmentation residues of the isotopic chain of Sn (from 130 to 137). The dotted area corresponds to the r-process path. See text for details.

the 130 and 137. We see how it is possible to cover the Zr-Rh gap with rather high intensities. The r-process path is also covered, extending beyond the present limits of the nuclide chart.

Production of very neutron-rich nuclei between Ba (Z=56) and Sn (Z=50)

In this section, we present the results obtained in the fragmentation of ^{151}Ba and ^{150}Cs , two candidate projectiles for the production of very neutron-rich nuclei in this region of the nuclide chart.

Figure 5.13 shows the calculated yields for the elements between Xe and In, which are covered by both projectiles. In both cases, very neutron-rich nuclei with intensities of several tenths per second are produce for elements closer to the projectiles, and the yields decrease rapidly for the lighter elements. We also see that the use of the ^{150}Cs projectiles provides better yields than the ^{151}Ba beam. This is due not only to the higher cross sections of the ^{150}Cs , but also to the release efficiency of the Ba isotopes in the ISOL target. Figure 5.10 shows how the release efficiency reduces the beam intensity of the Ba beam in several orders of magnitude, while the efficiency is much higher for Cs.

Production of very neutron-rich nuclei below Sr (Z=38)

In a similar way, we have investigated the possibility to take profit from the fragmentation of lighter neutron-rich fission fragments to produce even more neutron-rich isotopes which have low yields from the direct fission.

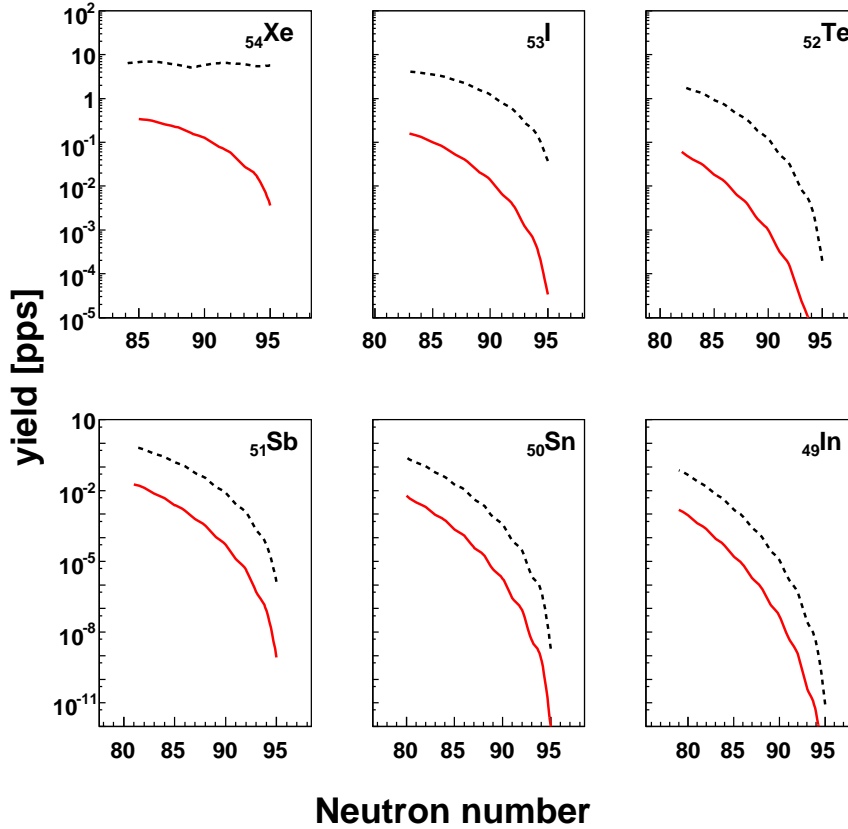


Figure 5.13: Production yields from the fragmentation of ^{151}Ba (solid line) and ^{150}Cs (dashed line).

The light fission fragments evaluated in this study have been ^{100}Sr , ^{98}Kr , ^{84}Ga and ^{73}Ni . These projectiles were selected as a compromise between the neutron number and the secondary beam intensity which can be achieved. Figure 5.15 shows a comparison of the estimated production yields of the fragmentation of ^{100}Sr and ^{98}Kr for the elements covered by both systems. The figure shows that the yields obtained with the Kr beam are much higher than those produced with the Sr. Indeed, the most neutron-rich isotopes of Br, Ge or As have production yields several orders of magnitude higher with the Kr beam than with the Sr beam. The yields decrease rapidly for lighter elements and the yields drop from several hundreds of ions per second to less than 10^{-6} ions/s. Therefore, Kr is a good candidate for the production of very neutron-rich elements in the region between Br and Zn.

Nuclei lighter than Zn can be produced in the fragmentation of Ga or

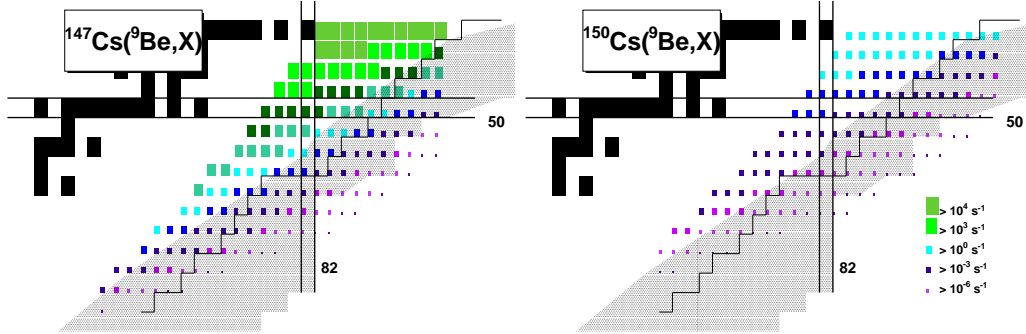


Figure 5.14: Production yields in the fragmentation of Cs isotopes produced in fission on top of the chart of nuclides. The left panel corresponds to fragmentation of ^{147}Cs . The right panel shows the fragmentation residues of ^{150}Cs . The dotted area corresponds to the r-process path. See text for details.

Ni beams. In Fig. 5.16 we show the estimated production yields for the fragmentation of ^{84}Ga and ^{73}Ni . We see here, that the fragmentation of these two neutron-rich fission residues are complementary. Fragmentation of the ^{84}Ga projectiles allows us to produce more neutron-rich fragments than with Ni, because of the larger neutron excess of this isotope. For elements lighter than Cr, the fragmentation of Ni becomes more competitive, but the isotopes available are less neutron-rich.

Based on the obtained results for the expected production yields, we can conclude that the most appropriate neutron-rich fission residues for post-acceleration and fragmentation in a 2-step scenario to overcome the problem of the extraction of the refractory elements, are Sn, Kr, Ga and Ni isotopes. The selected elements will provide very neutron-rich medium mass nuclei in a range between Ca and Sn.

The expected calculated yields are summarized in Figure 5.17. This figure shows all the expected production rates of the fragmentation residues of the projectiles presented in Table 5.2, on top of the nuclide chart. The color scale and size of the boxes represent the different values. The left panels correspond to specific isotopes of each elements (from up to down: ^{98}Kr , ^{84}Ga and ^{73}Ni), while the right panels show the yields obtained with the fragmentation of the whole isotopic chains of each element. We can see that the fragmentation of these neutron-rich fission residues, we produce even more neutron-rich reaction products. The most neutron-rich fragments that can be obtained for each projectile correspond to the proton removal channels, where only protons are abraded. In the case of the fragmentation of ^{132}Sn , many elements of the N=82 shell are produced, from ^{131}In up to ^{125}Tc . This last corresponds to the 7-proton removal channels. Cold fragmentation of the other projectiles

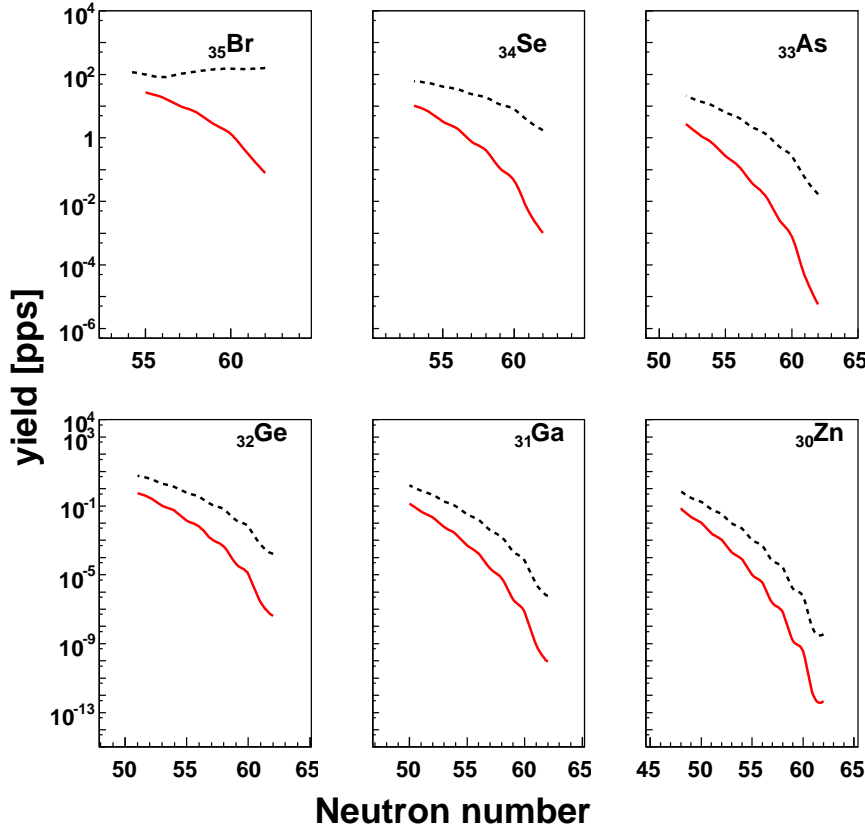


Figure 5.15: Production yields from the fragmentation of ^{100}Sr (solid line) and ^{98}Kr (dashed line).

makes it possible to extend beyond the present limits of the chart of nuclides by six or seven isotopes. In the case of ^{81}Ga the 3-proton removal channel corresponds to the doubly-magic ^{78}Ni , with a production rate of several ions per second.

For each of the nuclei of Table 5.2, we selected two isotopes as optimum candidates for the 2-step reaction scheme. This was based on their production yields in fission and their neutron number. In the Figure 5.18 we can see the area of the nuclide chart that is covered using the 2-step reaction scheme for different projectiles, represented as open circles. We see a big number of medium-mass neutron-rich nuclei are produced. The plot shows that we not only cover the refractory elements gap unreachable by the ISOL technique, but that we are able to extend considerably beyond the present limits of the nuclide chart. We also see that we can produce elements of closed shells

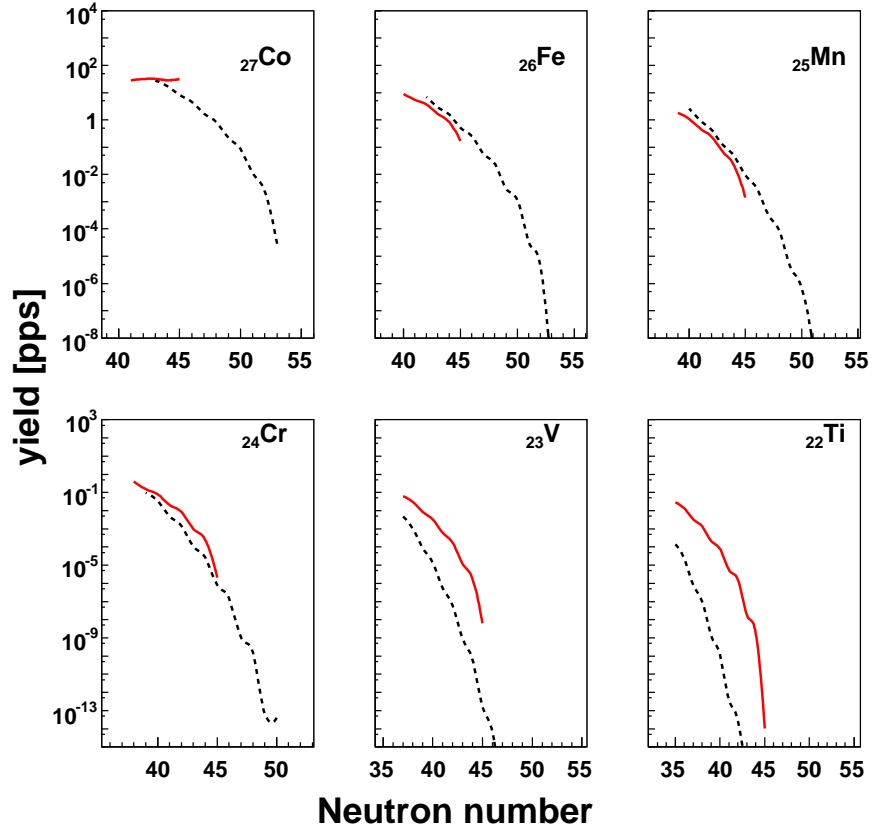


Figure 5.16: Production yields from the fragmentation of ^{73}Ni (solid line) and ^{84}Ga (dashed line).

N=82 and N=50 with rather high production rates. The nuclei produced also cover the r-process path in this region of the nuclear landscape.

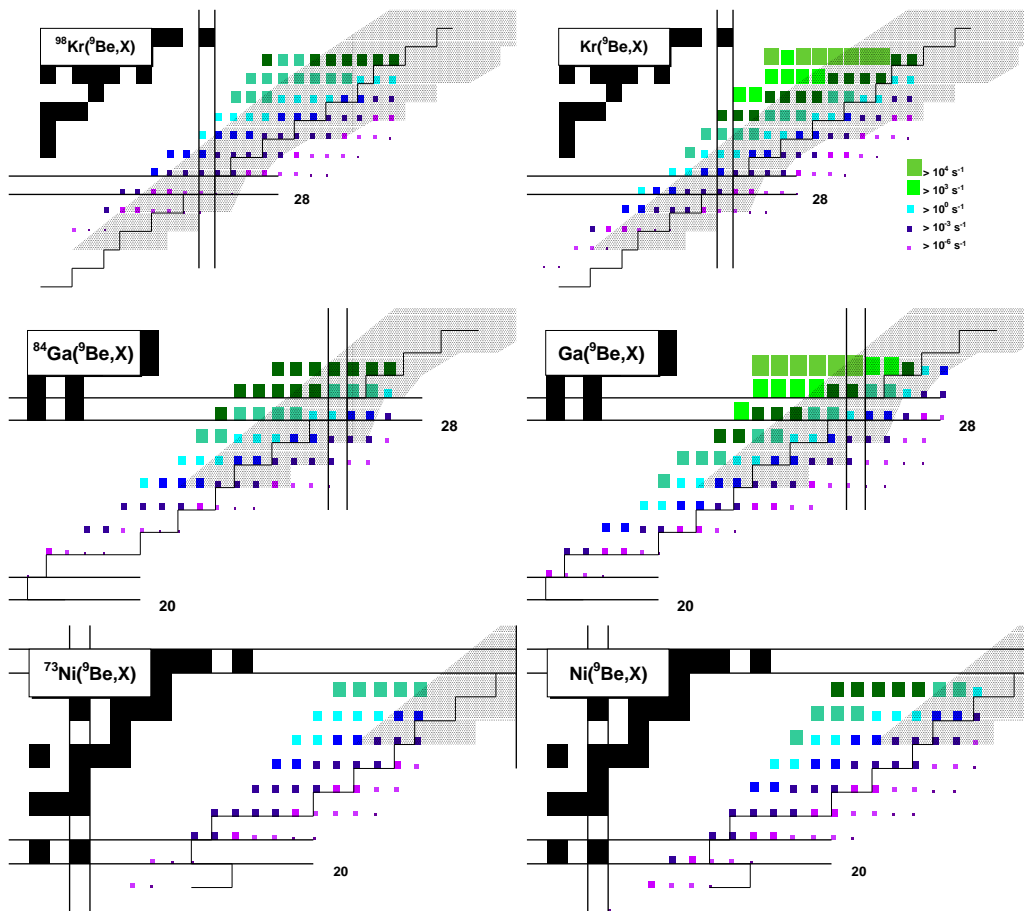


Figure 5.17: Production yields in the fragmentation of fission fragments on top of the chart of nuclides. Left panels corresponds to the fragmentation of ^{98}Kr , ^{84}Ga and ^{73}Ni . Right panels are the fragmentation residues of the isotopic chain of Kr, Ga and Ni. The dotted area corresponds to the r -process path. See text for details.

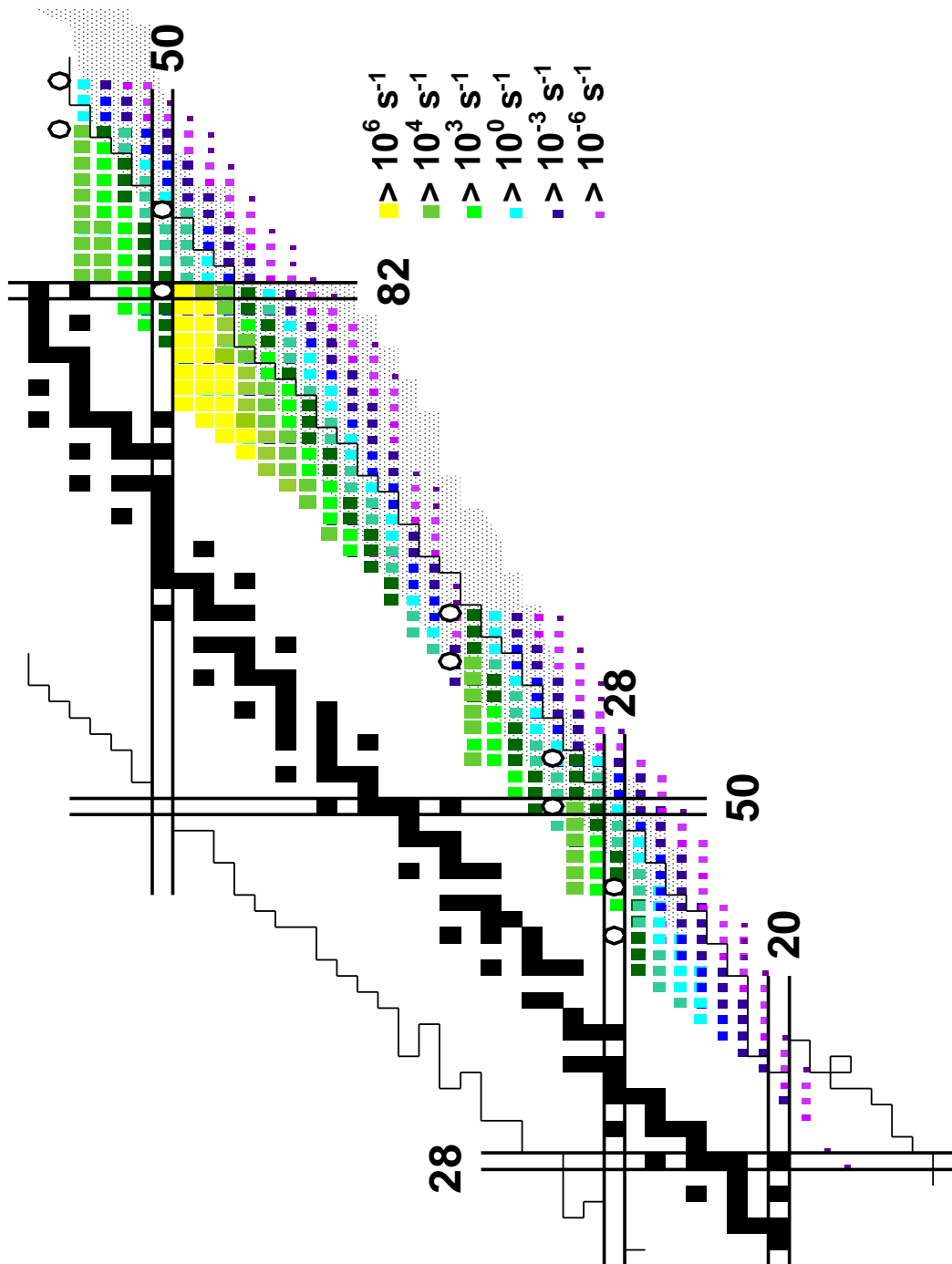


Figure 5.18: Production yields of medium-mass neutron-rich nuclei produced in the fragmentation reactions of selected fission residues, indicated by open circles, on top of the chart of nuclides. The dotted area corresponds to the r-process path.

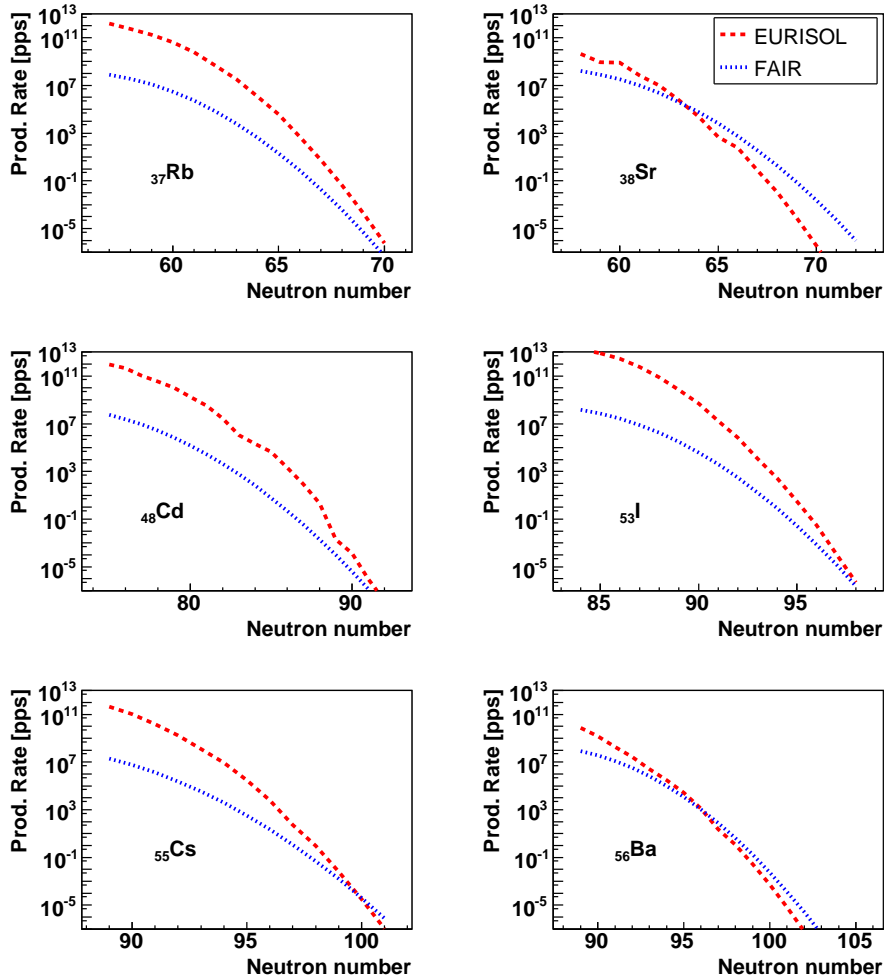


Figure 5.19: Production yields in EURISOL after release efficiency correction (dashed line) compared to the yields obtained for in-flight fission in FAIR (dotted line).

5.5. ISOL Fission versus In-Flight fission

In this section we will compare the expected production yields in of medium mass neutron-rich nuclei in EURISOL considering only the direct production by fission, and the expected production rates in the FAIR facility by means of nuclear reaction induced fission.

Figure 5.19 shows this comparison for those elements whose values of efficiency were available, with the production rates at the Super-FRS in FAIR.

These plots show that for moderate neutron-rich isotopes, the ISOL method gives much higher yields than the in-flight technique. For the production of very-neutron rich fission residues, the in-flight fission is a better choice for elements such as Sr and Ba. Although the fission rate in the ISOL target is three orders of magnitude larger than the intensity of the uranium beam available at the FAIR facility, the release efficiency, combined with the larger production cross section of neutron-rich fission fragments at higher excitation energies makes the in-flight fission a more efficient mechanism for the producing extremely neutron-rich nuclei.

5.6. In-flight fission versus fragmentation of fission residues

In this section, we will compare expected production yields from direct fission using the in-flight method, and the 2-step reaction scenario presented in previous section.

Figure 5.20 shows the expected production yields of elements from In to Nb from in-flight fission and from the fragmentation of ^{132}Sn . We can see that the production yields in fission are higher for the less neutron-rich isotopes, but the yields decrease quickly with the neutron number because of the rapid drop in the cross section. In the neutron-rich part, the fragmentation of ^{132}Sn becomes more competitive. It provides larger production rates than with fission, especially for those elements closer to the projectile, where the yields increase several orders of magnitude. For lighter elements, the difference is not so significant, but the fragmentation of ^{132}Sn is a better alternative for the production of neutron-rich isotopes of these elements. Figure 5.21 shows the comparison of these two mechanisms for lighter elements, from Y to Ga. For those elements lighter than Kr, the production yields for the fragmentation of ^{98}Kr have been included. The production rate of extremely neutron-rich Y isotopes is still higher with the fragmentation of Sn. However, in the region between Sr and Kr, the fragmentation yields drop and fission becomes a better choice for producing large neutron excess isotopes of these elements, giving yields several orders of magnitude larger. For elements lighter than Kr, the fragmentation of ^{98}Kr produces higher yields of neutron-rich isotopes, while for lower neutron number, the fission shows larger productions.

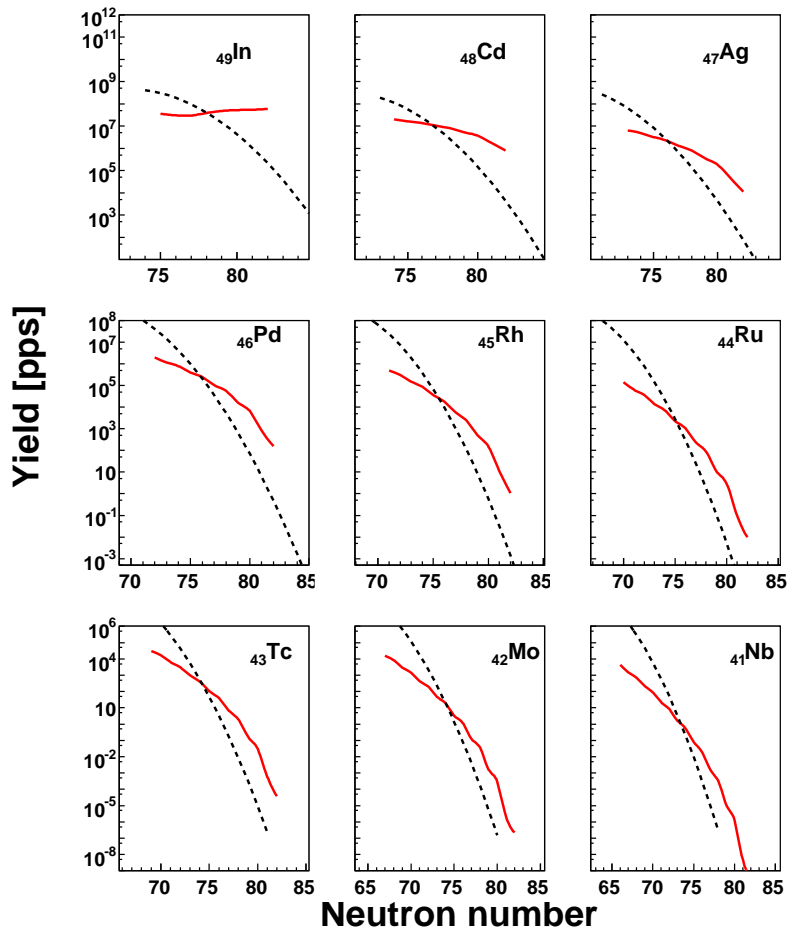


Figure 5.20: Production yields in the fragmentation of ^{132}Sn (solid line) and in-flight ^{238}U fission induced by a beryllium target (dashed line).

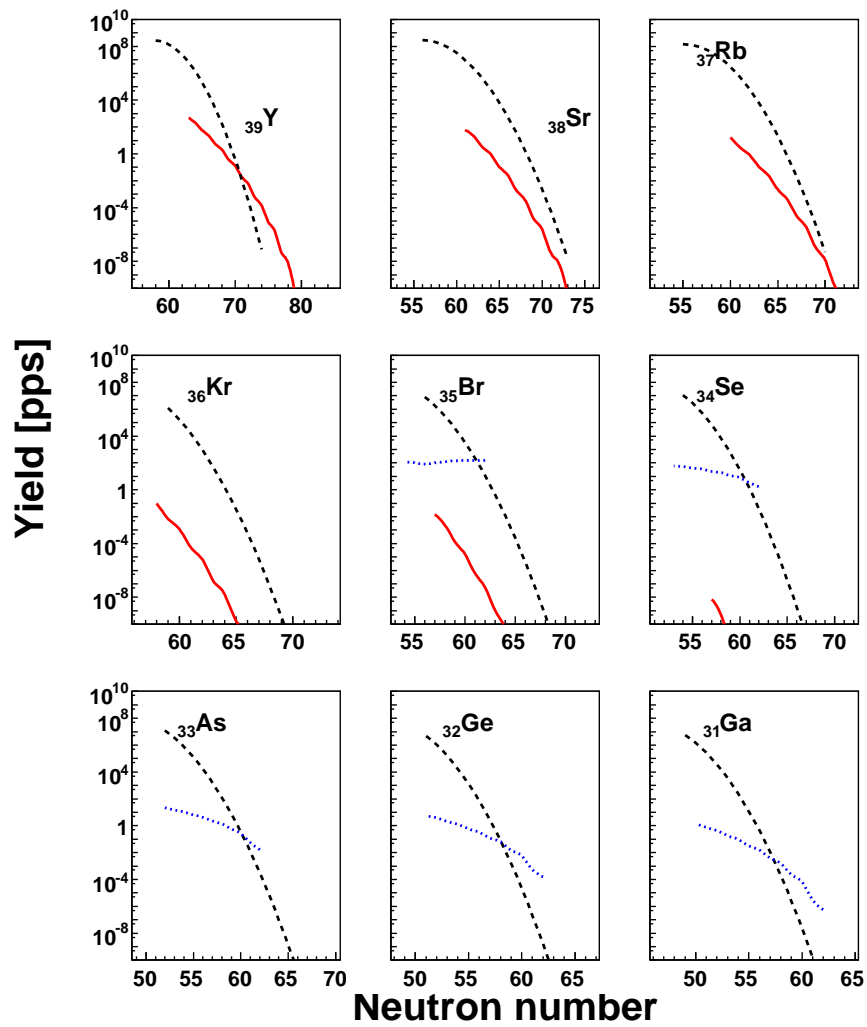


Figure 5.21: Production yields from fragmentation of ^{132}Sn (solid line) and fragmentation of ^{98}Kr (dotted-line) compared to the in-flight fission of ^{238}U induced by a beryllium target (dashed line).

5.7. Conclusions

In this chapter, the expected production yields of medium-mass neutron-rich nuclei in the FAIR and EURISOL facilities were presented and the three methods which will be available in these facilities were compared: in-flight fission in FAIR, and the ISOL fission and the fragmentation of post accelerated fission fragments in the case of the EURISOL facility. We demonstrated that for moderate neutron excess and those elements which are efficiently extracted from ISOL targets, neutron-induced fission at the ISOL target is the best choice, presenting yields several orders of magnitude higher than other mechanisms. However, in-flight fission is a good alternative for larger neutron number, due to the wider distributions of the fission fragments at higher excitation energies.

Since refractory elements cannot be extracted from the ISOL target, in-flight fission and fragmentation of post-accelerated fission fragments are the only two alternatives. We have studied different elements as possible projectiles, and found that Cs, Sn, Kr, Ga and Ni to be good choices. They cover the refractory metals gap and heavier and lighter areas of the nuclide chart, approaching to the r-process path and extending beyond the present limits of the nuclear landscape. Comparison of the yields using these two methods revealed that fragmentation of post-accelerated fission fragments is a more competitive mechanism for producing neutron-rich isotopes for elements up to Sr, where the production rates become higher in fission. In elements lighter than Kr, the fragmentation of ^{98}Kr presents a behaviour similar to that of ^{132}Sn . While for moderate neutron excess the fission is a better mechanism for producing these isotopes, the fragmentation becomes more competitive for larger neutron excess.

Conclusions

In this manuscript we have presented the results of an experimental program aimed at investigating the reaction mechanisms for the production of medium-mass neutron-rich nuclei. Two different production mechanisms were investigated: the fission of ^{238}U at different excitation energies and the fragmentation of fission fragments using a two-step reaction scheme.

Both production mechanisms were investigated on the basis of the isotopic production cross sections of their reaction products, which were determined from an experiment performed in November-December, 2006 at the GSI experimental facilities in Darmstadt (Germany). The ^{238}U beam delivered by SIS synchrotron at 950 AMeV impinged onto a beryllium or lead target in order to induce the fission of the projectiles. The experiments were carried out in the FRS magnetic spectrometer, which uses inverse kinematics to provide the isotopic separation and identification of all the fission and fragmentation residues.

By using a beryllium and a lead target, we were able to investigate the role of the excitation energy in the distribution of the fission residues, especially neutron-rich nuclei, due to the different production mechanisms enhanced by each target. Two targets were used to simulate the productions of fission fragments in two different scenarios: the low-energy neutron-induced fission in ISOL facilities and the in-flight fission induced by fragmentation reactions. The use of a heavy element like lead, enhances the Coulomb fission, with an excitation energy around 10-12 MeV. The light beryllium target, on the other hand, enhances the fission induced by nuclear reactions. The mean excitation energy in this last mechanism is 27 MeV per abraded nucleon. The cross sections obtained from the experiment were compared with ABRABLA model calculations and previous measurements found on the literature: lead induced fission [Enq99] and beryllium induced fission [Per07b]. Rather good agreement was seen in the overlapping area. The new data complement the previous measurements and go further in neutron excess. The very high intensity of the primary beam allowed us to produce very neutron-rich isotopes of fission fragments ranging from Rb to La, with cross sections as low as 100

pb. The model calculations cannot reach the most neutron-rich isotopes that were measured, even for very long calculations. Our measured data were also fitted to extrapolate the behaviour of the distributions for very large neutron excess. The extrapolation allowed us to estimate the optimum energy range in which fission leads to the production of the largest variety of very neutron-rich fragments. The fission induced by the lead target yields an asymmetric pattern for fission fragments when compared to the symmetric splitting. In the case of beryllium target, the distribution becomes more symmetric, with similar productions for all the fission residues measured. The maximum of the distribution for the lead target is more neutron-rich than that of the beryllium target. This is due to the fact that the larger excitation energy introduced in the fissioning system by the beryllium target yields a higher probability of neutron evaporation. In spite of the less neutron-rich maximum of the isotopic distributions of fission fragments, the fluctuations in isospin increase, leading to a wider distribution that reaches larger neutron excess than with low excitation energy fission. Therefore, we can conclude that fission at moderate excitation energies (around 50 MeV) not only covers a larger range of elements enhancing the symmetric splitting, but also produces more neutron-rich isotopes, especially for lighter elements.

The other possibility considered for producing medium-mass neutron rich-nuclei in this work was the fragmentation of fission residues in a two step-reaction scheme, in which the neutron-rich fission products can be used to produce very neutron-rich fragmentation products via the *cold fragmentation* channels. In order to investigate this method, a pioneering experiment was performed in the FRagment Separator at GSI using the spectrometer as two independent spectrometers in a two-stage scheme: the fission fragments produced in the production target were identified in the first part of the spectrometer up to the intermediate focal plane, where they impinged onto a beryllium fragmentation target. Then, the second part of the spectrometer was tuned to transmit the reaction products to the final focal plane of the spectrometer, where they were identified. Two main difficulties were overcome during this experiment: the identification of fragments with masses up to $A \sim 150$ using only the first part of the spectrometer and managing the very high counting rates at the first stage of the experimental setup. The first of these was resolved by an improved time-of-flight system with very fast plastic scintillators and the use of high resolution TPC position detectors, which for the first time allowed us to identify medium-mass fragments using only the first half of the spectrometer. For the second we used detectors with high counting capabilities, which made it possible to manage the rates produced by the fission fragments.

We measured the production cross sections of neutron-rich isotopes of

In, Cd, Ag, Rh and Ru, close to or at the $N=82$ shell, in the fragmentation of ^{132}Sn produced in the fission of ^{238}U at 950 AMeV with cross sections as low as $5 \mu\text{b}$. The most neutron-rich nuclei that can be produced, which correspond to the proton removal channels have been reached for In, Cd and Ag. The results obtained were used to benchmark two different codes, the semi-empirical EPAX formula and the COFRA code. We demonstrated that the COFRA code provides a better overall description of the obtained results than the EPAX formula. EPAX presents very good agreement with those fragments close in mass to the projectile, but it clearly overestimates the productions of those nuclei far from the projectile, especially for the most neutron-rich ones. On the other hand, COFRA slightly underestimates the cross sections for those elements with moderate neutron number. Our results confirmed the validity of the COFRA code for the estimation of cold fragmentation cross sections in neutron-rich nuclei.

The cross sections obtained were also compared with the results measured in the fragmentation of ^{136}Xe on Be. The cross sections obtained with the ^{132}Sn projectiles are higher than those obtained with the Xe beam. Therefore, the fragmentation of ^{132}Sn produced in fission is a more appropriate mechanism for the production of medium-mass neutron-rich nuclei. We have also compared the cross sections of the cold fragmentation channels in search of a possible neutron skin in the ^{132}Sn . If ^{132}Sn had a neutron skin, lower cross sections would be expected in the proton removal channels. Our results did not show such behaviour, therefore mass distributions for both systems should be similar.

Finally, from the results obtained in the Chapters 3 and 4, we made realistic estimations in Chapter 5 of the production yields of medium-mass neutron-rich nuclei in future radioactive beam facilities in Europe, EURISOL and FAIR, comparing the three methods that will be available in these facilities: in-flight fission at FAIR, ISOL fission and fragmentation of post-accelerated fission fragments in the case at the EURISOL facility.

We have demonstrated that for, moderate neutron excess, and elements that are efficiently extracted from ISOL targets, neutron-induced fission at the ISOL target is the best choice, providing yields several orders of magnitude higher than other methods, like in-flight fission. However, for larger neutron number, in-flight fission is a better alternative due to the wider distributions of the fission fragments at higher excitation energies.

Since the refractory elements cannot be extracted from the ISOL target, in-flight fission and fragmentation of post-accelerated fission fragments, are the only two alternatives. We have studied different fission residues as candidates for post-acceleration and subsequent fragmentation. We found that Cs, Sn, Kr, Ga and Ni cover not only the refractory metals gap, but

also heavier and lighter areas of the nuclide chart, approaching the r-process path and expanding the present limits of the nuclear landscape. Comparison of the yields using these two methods revealed that fragmentation of post-accelerated fission fragments is the more competitive mechanism for producing very neutron-rich isotopes, for elements up to Sr, where the production rates are higher in fission. Between krypton and arsenic, the fission presents higher yields than fragmentation, even for the largest neutron excess. However, even though fission presents higher yields for moderate neutron number nuclei for elements lighter than arsenic, the fragmentation of ^{98}Kr becomes more competitive for producing the most neutron-rich isotopes of these species.

We have then demonstrated that with fragmentation of neutron-rich fission residues, we can exceed the present limits of the chart of nuclei considerably for charges between 20 and 50, completely covering the whole r-process path in this region of the nuclear landscape.

Resumen en castellano

En este trabajo se ha realizado el estudio de dos mecanismos para la producción de núcleos ricos en neutrones de masa intermedia, la fisión directa y la fragmentación de residuos de fisión. La investigación de ambos métodos se realizó en un experimento que tuvo lugar en el centro de investigación alemán *Gesellschaft für Schwerionenforschung* (GSI) [GSI] en Darmstadt entre noviembre y diciembre de 2006.

A lo largo de los últimos años, los haces radiactivos han demostrado ser una herramienta muy potente para explorar las propiedades de los núcleos atómicos. La mayor parte de nuestro conocimiento acerca de la estructura nuclear está basada en las propiedades de los núcleos próximos al valle de estabilidad β , en el cual la razón entre el número de protones y neutrones no es muy diferente de la de los núcleos estables. Sin embargo, extrapolar este comportamiento a regiones de la carta de núcleos lejos de la estabilidad no se puede hacer de forma directa. De este modo, la producción de haces secundarios de estos núcleos se hace necesaria para comprender mejor el funcionamiento de la interacción nuclear.

Los núcleos que son estables frente a la desintegración β están localizados en una banda estrecha de la carta de núcleos (Fig. 1). Esta carta muestra en número de protones frente al número de neutrones de todos los núcleos conocidos hasta ahora. Los límites de la existencia de los núcleos están definidos por las llamadas *driplines*, tanto de protones como de neutrones. En el caso de los neutrones esta línea se encuentra más alejada que en el caso de los protones, debido a la repulsión coulombiana. Mientras que la *dripline* de protones se ha alcanzado para núcleos hasta la carga 80, a la *dripline* de neutrones sólo se ha conseguido llegar para los elementos más ligeros.

A medida que nuevos núcleos radiactivos se han ido produciendo, nuevas propiedades se observaron, desde nuevos tipos de desintegración, como la radiactividad de uno [Hof82] y dos protones [Gio02], hasta nuevas estructuras, como los halos [Tan85] y *pieles* [Suz95] de neutrones. Asimismo, a medida que el número de neutrones se incrementa, el modelo de capas empieza a fallar, produciéndose no sólo la desaparición de ciertos números mágicos [GM84;

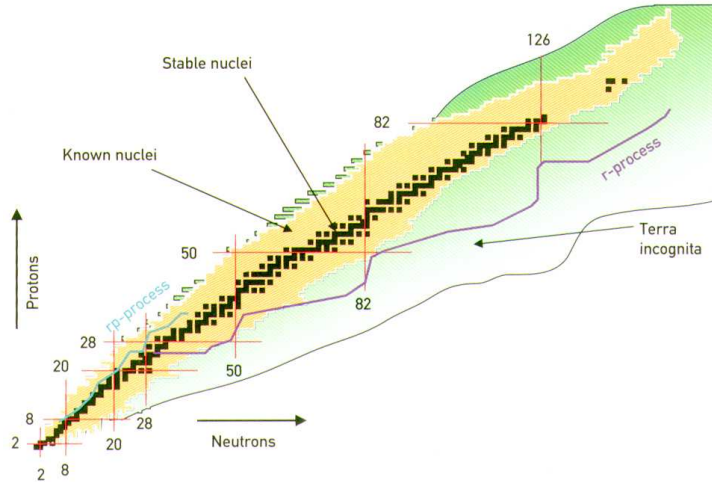


Figura 1: Carta de núcleos: Las líneas de los bordes marcan los límites de existencia (proton y neutron driplines) Los núcleos estables están representados por cuadrados negros. Aquellos núcleos que ya han sido observados se muestran en gris claro.

Sim99], sino también, la aparición de algunos nuevos [Oza00].

En el caso de los núcleos ricos en neutrones de masa intermedia, éstos juegan también un papel importante en la astrofísica nuclear, especialmente en los procesos de nucleosíntesis estelar. Uno de los mecanismos que explican la producción de núcleos más pesados que el hierro es el proceso r [Bur57]. Este proceso consiste en la captura rápida de neutrones en escenarios con un flujo de los mismos muy elevado. El camino que este proceso sigue a lo largo la zona de los elementos ricos en neutrones se denomina (*r-process path*). La producción de haces radiactivos en esta región permitirá mejorar nuestro conocimiento de la estructura y las propiedades de estos núcleos para así comprender el origen de los elementos presentes en nuestro sistema solar.

Esta serie de descubrimientos han tenido lugar debido a la disponibilidad haces de núcleos exóticos con los que poder hacer tanto estudios de reacciones como de estructura de los mismos. De este modo, el poder ir más allá en el número de neutrones en elementos más pesados, se presenta como un apasionante reto en el que se confirmen no sólo los fenómenos observados hasta ahora, si no que nuevas propiedades aparezcan. Para ello, nuevas instalaciones se están desarrollando actualmente en Europa, donde se puedan producir haces radiactivos de grandes intensidades de un gran número de núcleos [EUR; FAI].

Producción de núcleos exóticos

Dos son las técnicas que se utilizan actualmente para la producción de núcleos exóticos: la separación isotópica on-line (ISOL por sus siglas en inglés) y la separación en vuelo.

En la producción de núcleos exóticos en vuelo los mecanismos de reacción utilizados son la fragmentación y la fisión de iones pesados acelerados a altas energías. Éstos inciden sobre blancos relativamente delgados para que los productos de la reacción salgan del mismo. De este modo, pueden ser separados empleando un espectrómetro magnético. Las energías típicas de los haces producidos van desde los 30 MeV/u hasta 1 GeV/u. Este método de producción es el utilizado ya en algunas instalaciones actuales de forma exitosa para la producción de haces radiactivos de numerosas especies [GSI; RIK; NSC].

El método ISOL utiliza reacciones inducidas por proyectiles ligeros a energías de 1 GeV/u o por neutrones. Los núcleos radiactivos son producidos en reposo y luego extraídos de un blanco de producción grueso para luego ser enviados a una fuente de iones. Una vez separados, los iones producidos son post-acelerados. También esta técnica es usada también en instalaciones actuales [CRC; RIB; TRI].

Ambas técnicas son complementarias en varios aspectos. En lo que se refiere a intensidades de los haces secundarios, el método ISOL es superior para isótopos de determinados elementos, es decir, aquellos que se extraen rápida y eficientemente del sistema blanco-fuente. La separación en vuelo sin embargo, es independiente de las propiedades químicas de los elementos, y por tanto produce haces de todos los elementos. El método ISOL, está limitado por tanto, por la eficiencia de extracción y en muchos casos restringido a núcleos con una vida media larga. En el caso de a producción en vuelo, esta técnica nos da acceso a especies de vida media muy corta, por debajo del microsegundo.

Debido al gran número de descubrimientos realizados en la primera generación de instalaciones de haces radiactivos, una nueva generación de instalaciones se ha impulsado. En éstas, las mayores intensidades de los haces primarios, así como mejores técnicas de separación de los fragmentos, nos permitirán extender los límites actuales de la carta de núcleos, así como hacer estudios de reacciones y estructura de núcleos muy alejados de la estabilidad [FAI; EUR; SPI].

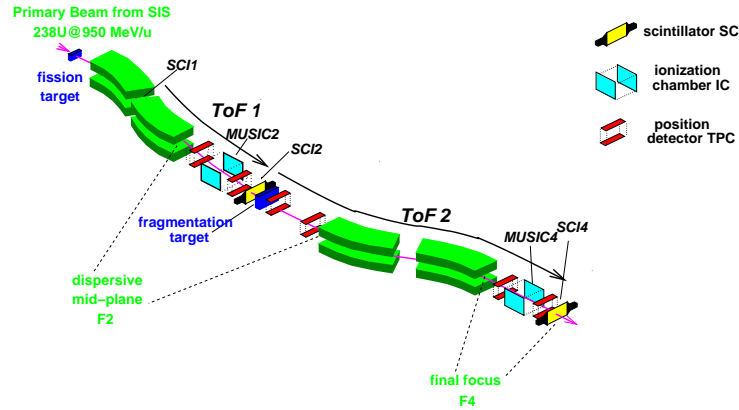


Figura 2: Representación esquemática del dispositivo experimental. La carga de los núcleos se determina con las cámaras de ionización (MUSIC). Las posiciones se miden con las TPCs. Los tiempos de vuelo para la determinación de las velocidades se miden entre los centelleadores SCI1-SCI2 (ToF1) y SCI2-SCI4 (ToF2).

Descripción del experimento

El experimento se realizó en las instalaciones de la GSI en Darmstadt, Alemania. El haz primario de ^{238}U con una energía de 950 MeV/u y una intensidad de 10^9 partículas por pulso incidía sobre un blanco de fisión que podía ser de Pb o Be. Los fragmentos fisión son emitidos hacia adelante debido a la focalización que produce la alta energía del haz incidente. De este modo, pueden ser analizados y separados usando el espectrómetro magnético FRS [Gei92].

La identificación de los fragmentos se hace basándose en la determinación de la razón carga-masa A/Q , a partir de la rigidez magnética y el tiempo de vuelo entre los centelleadores. La rigidez magnética se obtiene a partir de la posición de los fragmentos en el plano focal del espectrómetro con ayuda de las TPCs. Para obtener una identificación isotópica completa, la medida de la pérdida de energía de los iones en una cámara de ionización (MUSIC) permite medir la carga de los productos de la reacción.

En el caso del estudio de la fragmentación de los fragmentos de fisión, es necesario hacer dos identificaciones, una del proyectil, y otra del residuo de fragmentación. Para ello se empleó el FRS como dos espectrómetros diferentes. En la primera parte, se producía la identificación del proyectil, en este caso ^{132}Sn , y en la segunda parte se separaban e identificaban los productos de la reacción de fragmentación producidos por un blanco situado en el plano focal intermedio del FRS (Fig. 2). Las mayores dificultades en este experimento era la separación de elementos de masa $A \sim 150$ usando sólo la primera

parte del espectrómetro, así como la gran tasa de contaje en la primera parte debida al gran número de fragmentos de fisión producidos. Para conseguir separar elementos tan pesados usando sólo la primera parte del espectrómetro se usaron centelleadores rápidos y se hicieron correcciones en los valores del tiempo de vuelo usando el ángulo de entrada de los fragmentos incidentes. Pudiendo así identificar por primera vez fragmentos de fisión usando sólo la primera parte del separador. El problema de la tasa, se resolvió usando detectores preparados para soportar las tasas alcanzadas.

Producción de núcleos ricos en neutrones de masa intermedia

Fisión

La producción de elementos ricos en neutrones de masa intermedia en fisión se ha investigado usando dos blancos diferentes, plomo y berilio. Estos dos blancos nos permitieron estudiar la fisión a diferentes energías de excitación. De esta forma, se esperaba simular las producciones de los residuos de fisión en dos futuras instalaciones de haces radiactivos, FAIR y EURISOL. El blanco de plomo, al tener un número atómico muy alto hace que el principal mecanismo para inducir la fisión sea la excitación coulombiana del proyectil. Sin embargo, el uso de un elemento tan ligero como el berilio, hace que la excitación coulombiana se vea suprimida en favor de las reacciones nucleares. De este modo, la fisión inducida por el blanco de berilio, tiene lugar a una mayor energía de excitación. Se hicieron medidas de las secciones eficaces de producción de los isótopos más ricos en neutrones de elementos desde el Kr hasta el La usando ambos blancos, La figura 3 muestra las secciones eficaces de producción medidas en la fisión inducida por ambos blancos para algunos de elementos. Se muestran también los ajustes realizados de los datos a la exponencial de un polinomio de segundo grado en ambos blancos para extrapolar el comportamiento de las secciones eficaces a núcleos con mayor número de neutrones. Se observa que para la producción de elementos extremadamente ricos en neutrones, la fisión a energía de excitación moderada, es decir, la inducida por reacciones nucleares, es más competitiva que la fisión a baja energía de excitación. El máximo de las distribuciones isotópicas es más rico en neutrones en el caso de la fisión a baja energía de excitación, sin embargo, la fisión a energía de excitación moderada produce distribuciones más anchas, compensando este efecto, y permitiendo llegar más lejos en número de neutrones.

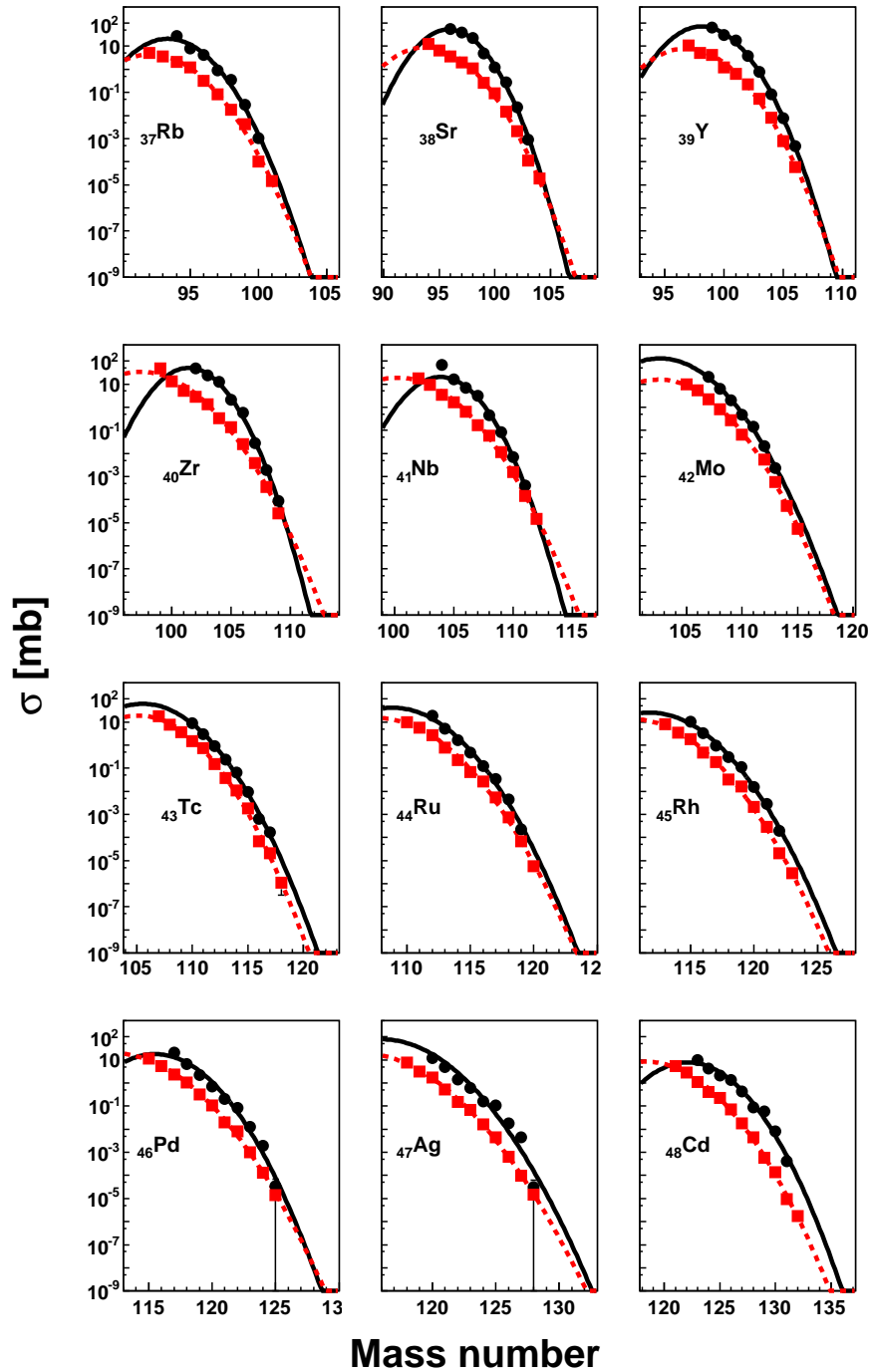


Figura 3: Secciones eficaces de producción de fragmentos de fisión producidos en la reacción $^{238}\text{U}(950 \text{ A MeV})+\text{Pb}$ (círculos negros) y $^{238}\text{U}(950 \text{ A MeV})+\text{Be}$ (cuadrados grises). Las líneas se corresponden con los ajustes para cada blanco. (Para más detalles ver texto).

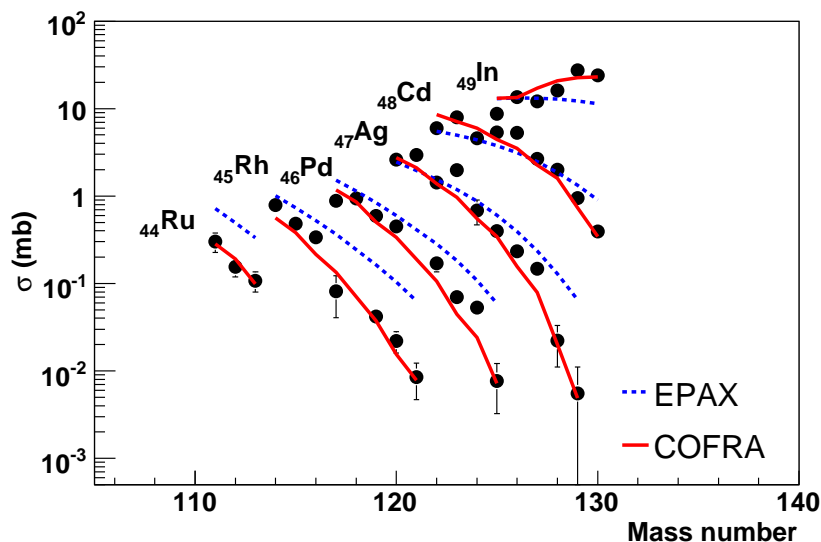


Figura 4: Distribuciones isotópicas de las secciones eficaces de producción de los núcleos producidos en la fragmentación de ^{132}Sn sobre berilio. Las barras de error se muestran si son mayores que los símbolos. Las líneas corresponden a los cálculos: EPAX [S00] (línea a trazos) y COFRA [COF] (línea continua).

Fragmentación de productos de fisión

La otra posibilidad investigada para producir núcleos ricos en neutrones de masa intermedia es la fragmentación de residuos de fisión ricos en neutrones. En este trabajo se ha medido la fragmentación de ^{132}Sn producido por fisión a energías relativistas incidiendo sobre un blanco de berilio de 2.6 g/cm^2 . El estudio de este proyectil es muy interesante, porque a partir de la fragmentación de éste es posible poblar el área de la carta de núcleos correspondiente a los elementos refractarios entre en niobio y el rodio, que no es posible extraer de blancos ISOL de forma eficiente con la tecnología actual. La figura 4 muestra las secciones eficaces de producción medidas en la fragmentación del ^{132}Sn sobre berilio a 950 MeV/u , para elementos desde el In hasta el Ru. Los resultados obtenidos son comparados con los cálculos usando dos modelos, la parametrización semiempírica EPAX [S00] y la aproximación analítica del modelo de abrasión-ablación COFRA [Ben99; COF]. Podemos ver como EPAX funciona bastante bien para describir la producción de fragmentos no muy diferentes en masa a la del proyectil, sin embargo, claramente sobreestima las producciones para aquellos núcleos más alejados del mismo, especialmente para los más ricos en neutrones. El código CO-

FRA, hace una mejor descripción global para las producciones de todos los fragmentos. De esta forma, hemos validado COFRA para la estimación de las secciones eficaces de producción en la fragmentación fría de proyectiles ricos en neutrones.

Producción de núcleos ricos en neutrones de masa intermedia en futuras instalaciones de haces radiactivos

A partir de los resultados de las secciones eficaces obtenidos tanto en la fisión directa como en la fragmentación de productos de fisión, se han podido hacer estimaciones realistas de las tasas de producción de elementos ricos en neutrones de masa intermedia en las dos futuras instalaciones de haces radiactivos que serán desarrolladas en Europa, EURISOL [EUR] y FAIR [FAI]. La primera es una instalación ISOL, aunque algunos productos de fisión serán post-acelerados para producir elementos mas ricos en neutrones a partir de la fragmentación de los mismos. De este modo, se puede producir haces radiactivos de elementos que no pueden ser extraídos de forma eficiente de los blancos de producción. FAIR en cambio es una instalación en la que el mecanismo de producción en la fragmentación y la fisión en vuelo de iones pesados a energías relativistas. La obtención de las tasas de producción en fisión, se ha realizado basándose en los resultados medidos con ambos blancos, así como las extrapolaciones de los ajustes de los mismos para elementos muy ricos en neutrones. La figura 5 muestra las tasas de producción calculadas en fisión usando ambos mecanismos, la fisión en vuelo inducidas por reacciones nucleares, y la fisión inducida por neutrones en un blanco ISOL. En el caso de la producción en vuelo (panel inferior), se ha tenido en cuenta la transmisión angular a lo largo de todo el espectrómetro. Para el método ISOL, aquellos elementos que no pueden ser extraídos del blanco han sido suprimidos. Con el fin de obtener una comparación lo más realista posible, las eficiencias de extracción e ionización han sido tenido en cuenta para la determinación de las tasas finales. Podemos ver como aunque el rango de elementos producidos en la producción en vuelo es mayor, las intensidades conseguidas con el método ISOL son mayores para ciertos elementos, como por ejemplo el ^{132}Sn .

Aprovechando las grandes intensidades disponibles para ciertos núcleos en EURISOL, se ha investigado la fragmentación de residuos de fisión. La figura 6 muestra las tasas de producción estimadas de cada fragmento sobre la carta de núcleos en iones por segundo. Los proyectiles utilizados para la obtención de estas estimaciones están indicados en la figura por un círcu-

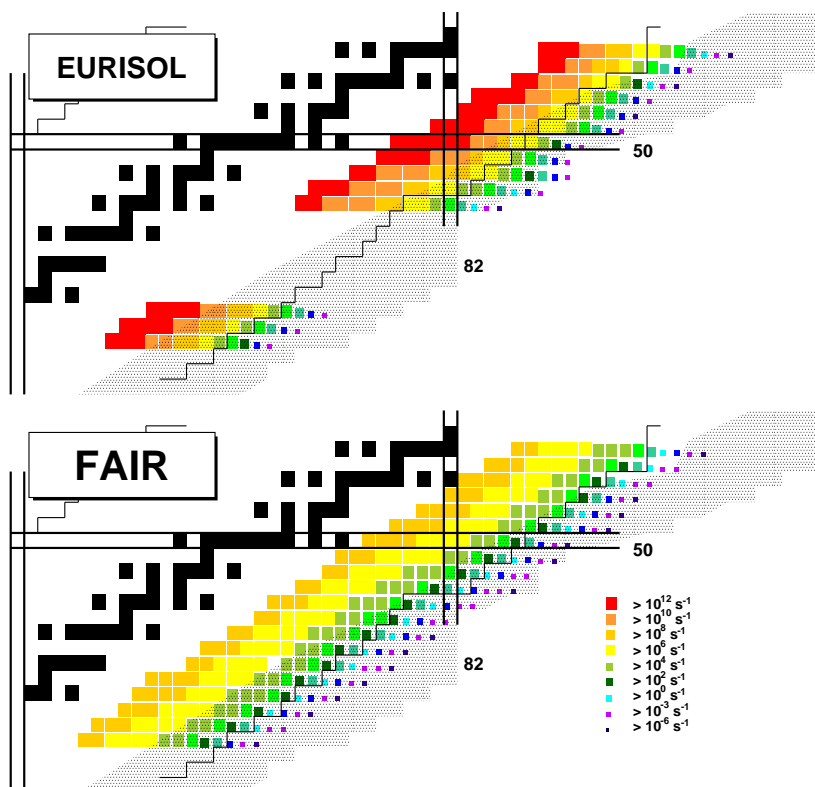


Figura 5: Panel superior: Estimación de las tasas de producción en el blanco de producción de EURISOL para una tasa de fisión de 10^{15} fisiones/s, aquellos elementos que no pueden ser extraídos del blanco ya han sido suprimidos. Panel inferior: Estimación de las tasas de producción en el super FRS de FAIR a partir de la fisión de ^{238}U incidiendo sobre un blanco de berilio. En ambos paneles, el área punteada muestra el camino del proceso r .

lo. Las intensidades iniciales de los mismos se han calculado a partir de la producción en el blanco y teniendo en cuenta las pérdidas por eficiencia de extracción e ionización.

Los resultados indican que con la fragmentación de isótopos de estaño no sólo se cubre el hueco de los elementos refractarios presente en el panel superior de la figura 5, sino que también se producen una gran cantidad de núcleos ricos en neutrones, extendiendo de forma significativa los límites actuales de la carta de núcleos en la región entorno a $N=82$. En base a este resultado, se ha estudiado también la fragmentación de productos de fisión más ligeros, como isótopos de kriptón, galio y níquel. Estos elementos se han seleccionado con el fin de cubrir la mayor área posible de la carta de núcleos correspondiente a isótopos ricos en neutrones de elementos de masa

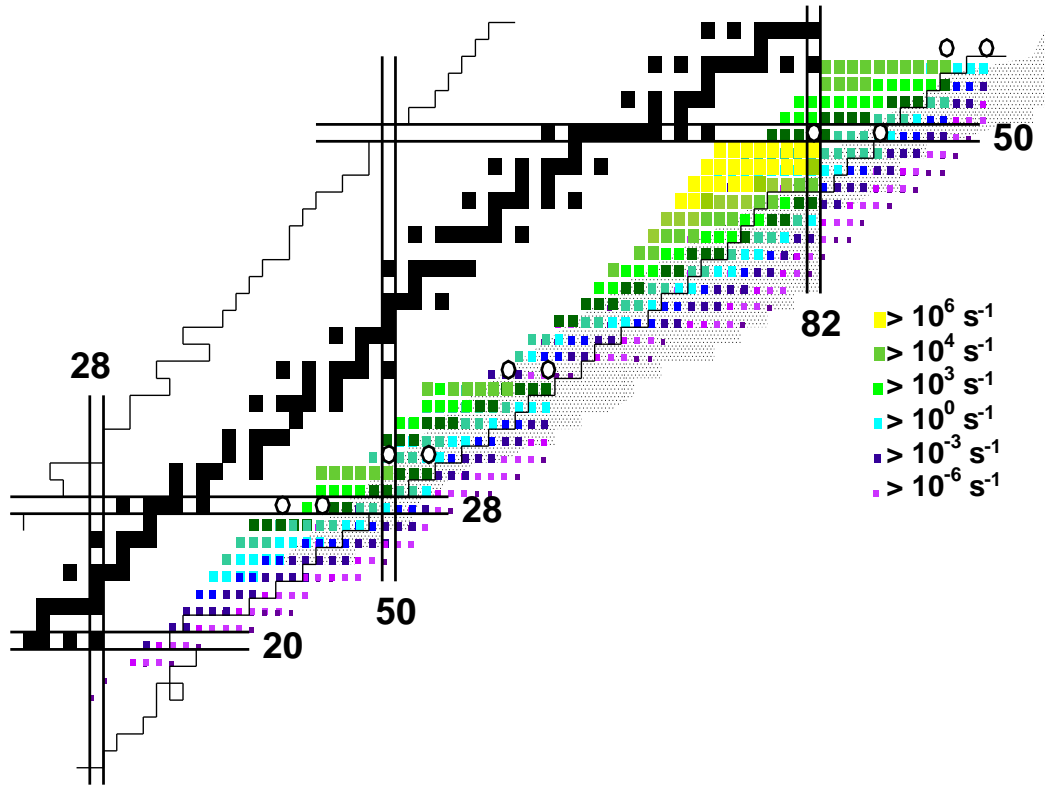


Figura 6: Tasas de producción estimadas en la fragmentación de residuos de fisión (círculos huecos) sobre la carta de núcleos. El área punteada muestra el camino del proceso r .

intermedia. Se observa que con la fragmentación de dichos núcleos, se logra ampliar de forma significativa los límites actuales de la carta de núcleos en la región entre $Z=20$ y 50 , cubriendo casi completamente el camino de proceso r en esta región, y produciendo el núcleo doblemente mágico ^{78}Ni . Por tanto, este método de producción basado en dos pasos, fisión y fragmentación, representa una excelente alternativa para la producción de núcleos ricos en neutrones de masa intermedia.

En general, en este trabajo, se han investigado los diferentes mecanismos para la producción de núcleos ricos en neutrones de masas intermedias fisión y fragmentación de residuos de fisión post-acelerados. En el caso de la fisión, se ha estudiado la dependencia de las producciones de dichos fragmentos con la energía de excitación, mostrando que la fisión a energías de excitación intermedias es más competitiva para la producción de núcleos extremadamente ricos en neutrones. Se ha investigado además la viabilidad de la producción de núcleos de masa intermedia con gran número de neutrones a partir de

la fragmentación de residuos de fisión post-acelerados, validando los resultados de COFRA frente a EPAX para la estimación de tasas de producción. Finalmente, se han hecho estimaciones realistas de las tasas de producción de estos elementos en las futuras instalaciones europeas, mostrando cómo a partir de la fragmentación de fragmentos de fisión es posible producir una gran cantidad de núcleos exóticos, permitiendo ampliar los límites de la carta de núcleos actual en seis y siete isótopos en el caso de algunos elementos, así como producir haces secundarios de elementos presentes en el camino de proceso r de nucleosíntesis estelar.

Appendix A

Measured fission cross sections

In this appendix we present the isotopic cross sections measured in this work: Table A.1, show the measured cross sections in the reaction $^{238}\text{U}+\text{Pb}$ at 950 AMeV and table A.2, the results obtained in the reaction $^{238}\text{U}+\text{Be}$ at 950 AMeV.

Table A.1: Fission production cross sections (in mb) measured in the reaction $^{238}\text{U}+\text{Pb}$ at 950 AMeV

| Z | A | σ_{f} | $\delta\sigma_{\text{f}}$ | Z | A | σ_{f} | $\delta\sigma_{\text{f}}$ | Z | A | σ_{f} | $\delta\sigma_{\text{f}}$ |
|----------|----------|---------------------|---------------------------|----------|----------|---------------------|---------------------------|----------|----------|---------------------|---------------------------|
| 36 | 90 | 4.66E+01 | 5.34E+00 | 39 | 102 | 3.70E+00 | 3.75E-01 | 41 | 110 | 7.04E-03 | 1.02E-03 |
| 36 | 91 | 3.00E+00 | 3.66E-01 | 39 | 103 | 7.73E-01 | 7.99E-02 | 41 | 111 | 4.00E-04 | 1.39E-04 |
| 37 | 94 | 2.74E+01 | 3.05E+00 | 39 | 104 | 8.45E-02 | 9.06E-03 | 42 | 107 | 2.10E+01 | 2.13E+00 |
| 37 | 95 | 7.89E+00 | 8.15E-01 | 39 | 105 | 7.46E-03 | 1.03E-03 | 42 | 108 | 6.20E+00 | 6.41E-01 |
| 37 | 96 | 4.15E+00 | 4.24E-01 | 39 | 106 | 4.74E-04 | 1.65E-04 | 42 | 109 | 1.97E+00 | 2.06E-01 |
| 37 | 97 | 8.79E-01 | 9.23E-02 | 40 | 102 | 4.82E+01 | 4.86E+00 | 42 | 110 | 4.70E-01 | 5.28E-02 |
| 37 | 98 | 3.44E-01 | 3.57E-02 | 40 | 103 | 2.36E+01 | 2.38E+00 | 42 | 111 | 1.46E-01 | 1.66E-02 |
| 37 | 99 | 2.92E-02 | 3.42E-03 | 40 | 104 | 1.24E+01 | 1.25E+00 | 42 | 112 | 2.04E-02 | 3.28E-03 |
| 37 | 100 | 1.06E-03 | 3.13E-04 | 40 | 105 | 2.08E+00 | 2.11E-01 | 42 | 113 | 2.30E-03 | 4.47E-04 |
| 38 | 96 | 5.46E+01 | 5.54E+00 | 40 | 106 | 5.75E-01 | 5.93E-02 | 43 | 110 | 8.81E+00 | 9.02E-01 |
| 38 | 97 | 4.00E+01 | 4.08E+00 | 40 | 107 | 2.77E-02 | 3.24E-03 | 43 | 111 | 2.96E+00 | 3.12E-01 |
| 38 | 98 | 2.28E+01 | 2.30E+00 | 40 | 108 | 1.87E-03 | 3.68E-04 | 43 | 112 | 9.09E-01 | 9.77E-02 |
| 38 | 99 | 4.96E+00 | 5.03E-01 | 40 | 109 | 8.90E-05 | 6.36E-05 | 43 | 113 | 2.37E-01 | 2.87E-02 |
| 38 | 100 | 1.19E+00 | 1.22E-01 | 41 | 103 | 1.00E+03 | 1.01E+02 | 43 | 114 | 6.53E-02 | 8.12E-03 |
| 38 | 101 | 2.67E-01 | 2.77E-02 | 41 | 104 | 6.68E+01 | 6.73E+00 | 43 | 115 | 9.44E-03 | 1.42E-03 |
| 38 | 102 | 2.32E-02 | 2.72E-03 | 41 | 105 | 1.61E+01 | 1.64E+00 | 43 | 116 | 6.25E-04 | 1.91E-04 |
| 38 | 103 | 9.05E-04 | 2.58E-04 | 41 | 106 | 6.92E+00 | 7.04E-01 | 43 | 117 | 1.68E-04 | 7.69E-05 |
| 39 | 99 | 6.45E+01 | 6.50E+00 | 41 | 107 | 3.10E+00 | 3.15E-01 | 44 | 112 | 1.86E+01 | 1.90E+00 |
| 39 | 100 | 3.00E+01 | 3.04E+00 | 41 | 108 | 4.44E-01 | 4.69E-02 | 44 | 113 | 5.03E+00 | 5.20E-01 |
| 39 | 101 | 1.78E+01 | 1.79E+00 | 41 | 109 | 8.37E-02 | 9.43E-03 | 44 | 114 | 1.61E+00 | 1.72E-01 |

Continued on next page

Table A.1: (continued)

| Z | A | σ_f | $\delta\sigma_f$ | Z | A | σ_f | $\delta\sigma_f$ | Z | A | σ_f | $\delta\sigma_f$ |
|----|-----|------------|------------------|----|-----|------------|------------------|----|-----|------------|------------------|
| 44 | 115 | 4.71E-01 | 5.28E-02 | 48 | 128 | 8.91E-02 | 1.30E-02 | 52 | 140 | 1.35E-01 | 1.44E-02 |
| 44 | 116 | 1.25E-01 | 1.69E-02 | 48 | 129 | 6.00E-02 | 6.92E-03 | 52 | 141 | 6.29E-03 | 1.16E-03 |
| 44 | 117 | 3.39E-02 | 4.66E-03 | 48 | 130 | 8.24E-03 | 1.06E-03 | 52 | 142 | 3.04E-04 | 2.17E-04 |
| 44 | 118 | 4.54E-03 | 8.10E-04 | 48 | 131 | 4.05E-04 | 1.16E-04 | 53 | 137 | 8.52E+01 | 8.55E+00 |
| 44 | 119 | 2.23E-04 | 1.02E-04 | 49 | 126 | 9.71E+00 | 9.89E-01 | 53 | 138 | 3.98E+01 | 4.00E+00 |
| 45 | 115 | 1.02E+01 | 1.05E+00 | 49 | 127 | 5.92E+00 | 6.05E-01 | 53 | 139 | 1.54E+01 | 1.55E+00 |
| 45 | 116 | 3.24E+00 | 3.39E-01 | 49 | 128 | 4.51E+00 | 4.59E-01 | 53 | 140 | 5.80E+00 | 5.84E-01 |
| 45 | 117 | 9.64E-01 | 1.04E-01 | 49 | 129 | 3.14E+00 | 3.18E-01 | 53 | 141 | 1.25E+00 | 1.28E-01 |
| 45 | 118 | 2.99E-01 | 3.42E-02 | 49 | 130 | 2.42E+00 | 2.45E-01 | 53 | 142 | 2.55E-01 | 2.68E-02 |
| 45 | 119 | 1.10E-01 | 1.30E-02 | 49 | 131 | 7.19E-01 | 7.32E-02 | 53 | 143 | 2.12E-02 | 2.84E-03 |
| 45 | 120 | 1.57E-02 | 2.57E-03 | 49 | 132 | 6.63E-02 | 7.22E-03 | 53 | 144 | 7.70E-04 | 2.45E-04 |
| 45 | 121 | 2.85E-03 | 5.60E-04 | 49 | 133 | 5.94E-03 | 7.94E-04 | 54 | 141 | 2.85E+01 | 2.86E+00 |
| 45 | 122 | 1.95E-04 | 8.94E-05 | 49 | 134 | 2.56E-04 | 8.49E-05 | 54 | 142 | 1.12E+01 | 1.12E+00 |
| 46 | 117 | 2.06E+01 | 2.12E+00 | 49 | 135 | 1.90E-05 | 1.91E-05 | 54 | 143 | 2.33E+00 | 2.37E-01 |
| 46 | 118 | 6.75E+00 | 6.94E-01 | 50 | 128 | 3.90E+01 | 3.94E+00 | 54 | 144 | 6.75E-01 | 7.00E-02 |
| 46 | 119 | 2.25E+00 | 2.39E-01 | 50 | 129 | 2.88E+01 | 2.90E+00 | 54 | 145 | 4.82E-02 | 5.91E-03 |
| 46 | 120 | 7.04E-01 | 7.66E-02 | 50 | 130 | 2.54E+01 | 2.55E+00 | 54 | 146 | 2.37E-03 | 6.56E-04 |
| 46 | 121 | 2.07E-01 | 2.48E-02 | 50 | 131 | 2.73E+01 | 2.74E+00 | 54 | 147 | 2.48E-04 | 1.26E-04 |
| 46 | 122 | 8.49E-02 | 1.02E-02 | 50 | 132 | 1.63E+01 | 1.63E+00 | 55 | 144 | 1.30E+01 | 1.31E+00 |
| 46 | 123 | 1.28E-02 | 2.20E-03 | 50 | 133 | 2.03E+00 | 2.07E-01 | 55 | 145 | 4.36E+00 | 4.41E-01 |
| 46 | 124 | 1.95E-03 | 4.16E-04 | 50 | 134 | 1.07E+00 | 1.08E-01 | 55 | 146 | 7.35E-01 | 7.67E-02 |
| 46 | 125 | 3.41E-05 | 3.43E-05 | 50 | 135 | 9.05E-02 | 9.87E-03 | 55 | 147 | 1.57E-01 | 1.77E-02 |
| 47 | 119 | 8.36E+01 | 8.99E+00 | 50 | 136 | 5.65E-03 | 1.13E-03 | 55 | 148 | 8.42E-03 | 1.61E-03 |
| 47 | 120 | 1.20E+01 | 1.24E+00 | 50 | 137 | 2.19E-04 | 7.62E-05 | 55 | 149 | 7.28E-04 | 3.34E-04 |
| 47 | 121 | 4.80E+00 | 4.95E-01 | 51 | 132 | 5.78E+01 | 5.80E+00 | 56 | 145 | 5.26E+01 | 5.28E+00 |
| 47 | 122 | 1.42E+00 | 1.56E-01 | 51 | 133 | 4.03E+01 | 4.04E+00 | 56 | 146 | 2.60E+01 | 2.61E+00 |
| 47 | 123 | 5.99E-01 | 6.51E-02 | 51 | 134 | 1.76E+01 | 1.77E+00 | 56 | 147 | 6.50E+00 | 6.59E-01 |
| 47 | 124 | 1.56E-01 | 1.93E-02 | 51 | 135 | 5.67E+00 | 5.71E-01 | 56 | 148 | 1.74E+00 | 1.79E-01 |
| 47 | 125 | 1.06E-01 | 1.21E-02 | 51 | 136 | 8.40E-01 | 8.74E-02 | 56 | 149 | 2.24E-01 | 2.52E-02 |
| 47 | 126 | 1.75E-02 | 2.61E-03 | 51 | 137 | 3.73E-01 | 3.84E-02 | 56 | 150 | 3.82E-02 | 5.37E-03 |
| 47 | 127 | 4.46E-03 | 1.05E-03 | 51 | 138 | 2.29E-02 | 2.97E-03 | 56 | 151 | 3.25E-03 | 8.74E-04 |
| 47 | 128 | 3.17E-05 | 3.18E-05 | 51 | 139 | 2.22E-03 | 6.33E-04 | 57 | 148 | 1.87E+01 | 1.89E+00 |
| 48 | 123 | 9.84E+00 | 1.01E+00 | 52 | 135 | 6.42E+01 | 6.43E+00 | 57 | 149 | 7.47E+00 | 7.56E-01 |
| 48 | 124 | 4.31E+00 | 4.44E-01 | 52 | 136 | 2.69E+01 | 2.71E+00 | 57 | 150 | 1.26E+00 | 1.34E-01 |
| 48 | 125 | 2.07E+00 | 2.16E-01 | 52 | 137 | 1.26E+01 | 1.27E+00 | 57 | 151 | 1.68E-01 | 2.66E-02 |
| 48 | 126 | 1.32E+00 | 1.37E-01 | 52 | 138 | 3.44E+00 | 3.48E-01 | 57 | 152 | 2.56E-02 | 4.50E-03 |
| 48 | 127 | 4.33E-01 | 4.71E-02 | 52 | 139 | 4.72E-01 | 5.05E-02 | 57 | 153 | 2.78E-03 | 1.02E-03 |

Continued on next page

Table A.1: (continued)

| Z | A | σ_f | $\delta\sigma_f$ | Z | A | σ_f | $\delta\sigma_f$ | Z | A | σ_f | $\delta\sigma_f$ |
|----|-----|------------|------------------|----|-----|------------|------------------|----|-----|------------|------------------|
| 58 | 151 | 5.87E+00 | 5.98E-01 | 59 | 152 | 1.39E+01 | 1.47E+00 | 60 | 155 | 3.59E+00 | 4.04E-01 |
| 58 | 152 | 1.55E+00 | 1.63E-01 | 59 | 153 | 4.52E+00 | 4.68E-01 | 60 | 156 | 9.43E-01 | 1.08E-01 |
| 58 | 153 | 1.86E-01 | 2.31E-02 | 59 | 154 | – | – | | | | |
| 58 | 154 | 2.97E-02 | 5.30E-03 | 59 | 155 | 1.81E-01 | 2.48E-02 | | | | |

Table A.2: Fission production cross sections (in mb) measured in the reaction $^{238}\text{U}+\text{Be}$ at 950 A MeV

| Z | A | σ_f | $\delta\sigma_f$ | Z | A | σ_f | $\delta\sigma_f$ | Z | A | σ_f | $\delta\sigma_f$ |
|----|-----|------------|------------------|----|-----|------------|------------------|----|-----|------------|------------------|
| 37 | 92 | 5.07E+00 | 7.91E-01 | 39 | 104 | 7.93E-03 | 8.07E-04 | 42 | 108 | 8.32E-01 | 1.33E-01 |
| 37 | 93 | 3.61E+00 | 4.93E-01 | 39 | 105 | 7.94E-04 | 8.55E-05 | 42 | 109 | 2.68E-01 | 2.92E-02 |
| 37 | 94 | 2.13E+00 | 3.39E-01 | 39 | 106 | 5.92E-05 | 9.77E-06 | 42 | 110 | 6.34E-02 | 8.19E-03 |
| 37 | 95 | 1.22E+00 | 1.30E-01 | 40 | 99 | 4.84E+01 | 7.99E+00 | 42 | 112 | 5.39E-03 | 5.48E-04 |
| 37 | 96 | 3.15E-01 | 3.77E-02 | 40 | 100 | 1.30E+01 | 1.50E+00 | 42 | 113 | 5.65E-04 | 6.49E-05 |
| 37 | 97 | 8.42E-02 | 8.46E-03 | 40 | 101 | 5.13E+00 | 6.00E-01 | 42 | 114 | 5.45E-05 | 8.19E-06 |
| 37 | 98 | 1.76E-02 | 1.78E-03 | 40 | 102 | 2.89E+00 | 3.63E-01 | 42 | 115 | 5.48E-06 | 1.91E-06 |
| 37 | 99 | 4.14E-03 | 4.36E-04 | 40 | 103 | 1.35E+00 | 1.40E-01 | 43 | 107 | 1.75E+01 | 3.12E+00 |
| 37 | 100 | 1.03E-04 | 1.62E-05 | 40 | 104 | 3.30E-01 | 3.62E-02 | 43 | 108 | 7.80E+00 | 9.31E-01 |
| 37 | 101 | 1.43E-05 | 4.98E-06 | 40 | 105 | 1.33E-01 | 1.33E-02 | 43 | 109 | 3.56E+00 | 4.19E-01 |
| 38 | 94 | 1.24E+01 | 1.98E+00 | 40 | 106 | 2.55E-02 | 2.57E-03 | 43 | 110 | 1.51E+00 | 1.96E-01 |
| 38 | 95 | 6.41E+00 | 8.28E-01 | 40 | 107 | 3.81E-03 | 3.93E-04 | 43 | 111 | 7.23E-01 | 7.61E-02 |
| 38 | 96 | 3.62E+00 | 4.70E-01 | 40 | 108 | 3.61E-04 | 4.07E-05 | 43 | 112 | 1.52E-01 | 1.71E-02 |
| 38 | 97 | 1.97E+00 | 2.98E-01 | 40 | 109 | 2.50E-05 | 5.14E-06 | 43 | 113 | 3.81E-02 | 5.36E-03 |
| 38 | 98 | 1.11E+00 | 1.17E-01 | 41 | 102 | 1.81E+01 | 2.42E+00 | 43 | 114 | 1.06E-02 | 1.07E-03 |
| 38 | 99 | 2.64E-01 | 2.65E-02 | 41 | 103 | 9.12E+00 | 1.04E+00 | 43 | 115 | 1.85E-03 | 1.93E-04 |
| 38 | 100 | 9.03E-02 | 9.06E-03 | 41 | 104 | 3.46E+00 | 4.12E-01 | 43 | 116 | 6.87E-05 | 1.27E-05 |
| 38 | 101 | 1.45E-02 | 1.47E-03 | 41 | 105 | 1.64E+00 | 2.25E-01 | 43 | 117 | 2.09E-05 | 4.10E-06 |
| 38 | 102 | 2.11E-03 | 2.30E-04 | 41 | 106 | 6.31E-01 | 6.65E-02 | 43 | 118 | 1.09E-06 | 7.79E-07 |
| 38 | 103 | 1.11E-04 | 1.62E-05 | 41 | 107 | 1.67E-01 | 1.92E-02 | 44 | 110 | 9.71E+00 | 1.42E+00 |
| 38 | 104 | 1.88E-05 | 5.36E-06 | 41 | 108 | 5.86E-02 | 5.88E-03 | 44 | 111 | 5.64E+00 | 6.64E-01 |
| 39 | 97 | 1.06E+01 | 1.41E+00 | 41 | 109 | 1.15E-02 | 1.16E-03 | 44 | 112 | 2.69E+00 | 3.19E-01 |
| 39 | 98 | 5.19E+00 | 6.39E-01 | 41 | 110 | 1.58E-03 | 1.68E-04 | 44 | 113 | 7.86E-01 | 1.16E-01 |
| 39 | 99 | 4.12E+00 | 5.05E-01 | 41 | 111 | 1.41E-04 | 1.76E-05 | 44 | 114 | 2.25E-01 | 5.75E-02 |
| 39 | 100 | 1.19E+00 | 2.00E-01 | 41 | 112 | 1.50E-05 | 3.60E-06 | 44 | 115 | 6.84E-02 | 8.39E-03 |
| 39 | 101 | 6.50E-01 | 6.90E-02 | 42 | 105 | 9.81E+00 | 1.23E+00 | 44 | 116 | 2.63E-02 | 3.95E-03 |
| 39 | 102 | 2.23E-01 | 2.23E-02 | 42 | 106 | 5.47E+00 | 6.33E-01 | 44 | 117 | 5.34E-03 | 5.43E-04 |
| 39 | 103 | 5.33E-02 | 5.35E-03 | 42 | 107 | 2.15E+00 | 2.69E-01 | 44 | 118 | 7.49E-04 | 8.14E-05 |

Continued on next page

Table A.2: (continued)

| Z | A | σ_f | $\delta\sigma_f$ | Z | A | σ_f | $\delta\sigma_f$ | Z | A | σ_f | $\delta\sigma_f$ |
|----|-----|------------|------------------|----|-----|------------|------------------|----|-----|------------|------------------|
| 44 | 119 | 6.93E-05 | 1.04E-05 | 48 | 123 | 1.09E+00 | 1.42E-01 | 51 | 132 | 2.34E+00 | 2.60E-01 |
| 44 | 120 | 5.75E-06 | 1.83E-06 | 48 | 124 | 4.09E-01 | 6.62E-02 | 51 | 133 | 1.40E+00 | 1.67E-01 |
| 45 | 113 | 7.92E+00 | 1.01E+00 | 48 | 125 | 2.20E-01 | 2.43E-02 | 51 | 134 | 6.14E-01 | 6.28E-02 |
| 45 | 114 | 3.37E+00 | 4.06E-01 | 48 | 126 | 7.05E-02 | 8.21E-03 | 51 | 135 | 1.35E-01 | 1.43E-02 |
| 45 | 115 | 1.78E+00 | 2.17E-01 | 48 | 127 | 1.80E-02 | 1.82E-03 | 51 | 136 | 2.26E-02 | 3.00E-03 |
| 45 | 116 | 4.79E-01 | 8.19E-02 | 48 | 128 | 4.37E-03 | 4.46E-04 | 51 | 137 | 1.54E-02 | 1.54E-03 |
| 45 | 117 | 1.82E-01 | 2.03E-02 | 48 | 129 | 5.91E-04 | 6.40E-05 | 51 | 138 | 1.23E-03 | 1.27E-04 |
| 45 | 118 | 3.27E-02 | 4.50E-03 | 48 | 130 | 1.39E-04 | 1.87E-05 | 51 | 139 | 1.33E-04 | 1.68E-05 |
| 45 | 119 | 1.59E-02 | 1.60E-03 | 48 | 131 | 9.26E-06 | 2.37E-06 | 52 | 132 | 6.14E+00 | 7.80E-01 |
| 45 | 120 | 2.10E-03 | 2.17E-04 | 48 | 132 | 1.72E-06 | 7.86E-07 | 52 | 133 | 6.65E+00 | 7.22E-01 |
| 45 | 121 | 2.93E-04 | 3.49E-05 | 49 | 123 | 1.92E+01 | 3.71E+00 | 52 | 134 | 5.72E+00 | 6.03E-01 |
| 45 | 122 | 2.13E-05 | 4.49E-06 | 49 | 124 | 4.87E+00 | 6.23E-01 | 52 | 135 | 2.32E+00 | 2.56E-01 |
| 45 | 123 | 2.80E-06 | 1.18E-06 | 49 | 125 | 3.08E+00 | 3.60E-01 | 52 | 136 | 9.65E-01 | 1.23E-01 |
| 46 | 115 | 1.12E+01 | 2.47E+00 | 49 | 126 | 1.64E+00 | 1.95E-01 | 52 | 137 | 4.07E-01 | 4.19E-02 |
| 46 | 116 | 5.34E+00 | 6.61E-01 | 49 | 127 | 1.08E+00 | 1.37E-01 | 52 | 138 | 8.22E-02 | 8.97E-03 |
| 46 | 117 | 2.27E+00 | 2.80E-01 | 49 | 128 | 2.75E-01 | 2.94E-02 | 52 | 139 | 9.49E-03 | 1.57E-03 |
| 46 | 118 | 1.08E+00 | 1.41E-01 | 49 | 129 | 1.15E-01 | 1.25E-02 | 52 | 140 | 5.63E-03 | 5.68E-04 |
| 46 | 119 | 3.13E-01 | 6.09E-02 | 49 | 130 | 2.98E-02 | 3.00E-03 | 52 | 141 | 4.02E-04 | 4.37E-05 |
| 46 | 120 | 1.07E-01 | 1.23E-02 | 49 | 131 | 7.39E-03 | 7.47E-04 | 52 | 142 | 4.79E-05 | 7.53E-06 |
| 46 | 121 | 1.94E-02 | 2.97E-03 | 49 | 132 | 9.21E-04 | 9.66E-05 | 52 | 143 | 1.09E-06 | 6.39E-07 |
| 46 | 122 | 8.05E-03 | 1.72E-03 | 49 | 133 | 1.77E-04 | 2.22E-05 | 53 | 135 | 7.62E+00 | 8.78E-01 |
| 46 | 123 | 1.01E-03 | 1.07E-04 | 49 | 134 | 8.40E-06 | 2.15E-06 | 53 | 136 | 4.18E+00 | 4.63E-01 |
| 46 | 124 | 1.34E-04 | 1.80E-05 | 50 | 126 | 5.49E+00 | 1.06E+00 | 53 | 137 | 3.20E+00 | 3.46E-01 |
| 46 | 125 | 1.43E-05 | 3.38E-06 | 50 | 127 | 3.24E+00 | 4.14E-01 | 53 | 138 | 1.32E+00 | 1.54E-01 |
| 47 | 118 | 7.62E+00 | 1.20E+00 | 50 | 128 | 2.48E+00 | 2.89E-01 | 53 | 139 | 6.24E-01 | 8.70E-02 |
| 47 | 119 | 3.13E+00 | 3.99E-01 | 50 | 129 | 1.43E+00 | 1.70E-01 | 53 | 140 | 1.73E-01 | 1.83E-02 |
| 47 | 120 | 1.73E+00 | 2.14E-01 | 50 | 130 | 1.04E+00 | 1.32E-01 | 53 | 141 | 3.05E-02 | 3.70E-03 |
| 47 | 121 | 5.23E-01 | 8.09E-02 | 50 | 131 | 4.26E-01 | 7.54E-02 | 53 | 142 | 4.32E-03 | 9.23E-04 |
| 47 | 122 | 1.54E-01 | 3.94E-02 | 50 | 132 | 4.07E-01 | 4.17E-02 | 53 | 143 | 2.17E-03 | 2.21E-04 |
| 47 | 123 | 6.91E-02 | 8.23E-03 | 50 | 133 | 5.00E-02 | 5.86E-03 | 53 | 144 | 1.10E-04 | 1.39E-05 |
| 47 | 124 | 1.63E-02 | 2.54E-03 | 50 | 134 | 1.17E-02 | 1.18E-03 | 53 | 145 | 3.87E-06 | 1.63E-06 |
| 47 | 125 | 4.40E-03 | 4.49E-04 | 50 | 135 | 8.82E-04 | 9.24E-05 | 54 | 137 | 7.07E+00 | 1.09E+00 |
| 47 | 126 | 6.36E-04 | 6.90E-05 | 50 | 136 | 1.28E-04 | 1.66E-05 | 54 | 138 | 6.60E+00 | 7.43E-01 |
| 47 | 127 | 9.56E-05 | 1.38E-05 | 50 | 137 | 5.23E-06 | 1.60E-06 | 54 | 139 | 4.41E+00 | 4.79E-01 |
| 47 | 128 | 1.44E-05 | 3.23E-06 | 51 | 129 | 4.72E+00 | 7.16E-01 | 54 | 140 | 2.74E+00 | 2.97E-01 |
| 48 | 121 | 5.52E+00 | 7.70E-01 | 51 | 130 | 4.28E+00 | 4.97E-01 | 54 | 141 | 1.02E+00 | 1.22E-01 |
| 48 | 122 | 2.90E+00 | 3.54E-01 | 51 | 131 | 3.65E+00 | 4.00E-01 | 54 | 142 | 2.87E-01 | 5.01E-02 |

Continued on next page

Table A.2: (continued)

| Z | A | $\sigma_{\mathbf{f}}$ | $\delta\sigma_{\mathbf{f}}$ | Z | A | $\sigma_{\mathbf{f}}$ | $\delta\sigma_{\mathbf{f}}$ | Z | A | $\sigma_{\mathbf{f}}$ | $\delta\sigma_{\mathbf{f}}$ |
|----------|----------|-----------------------|-----------------------------|----------|----------|-----------------------|-----------------------------|----------|----------|-----------------------|-----------------------------|
| 54 | 143 | 6.75E-02 | 7.57E-03 | 55 | 149 | 7.56E-05 | 1.06E-05 | 57 | 149 | 2.03E-01 | 3.47E-02 |
| 54 | 144 | 9.33E-03 | 1.45E-03 | 56 | 143 | 3.88E+00 | 5.32E-01 | 57 | 150 | 4.00E-02 | 5.82E-03 |
| 54 | 145 | 2.61E-03 | 6.68E-04 | 56 | 144 | 3.19E+00 | 3.67E-01 | 57 | 151 | 5.64E-03 | 1.21E-03 |
| 54 | 146 | 3.84E-04 | 4.22E-05 | 56 | 145 | 1.89E+00 | 2.15E-01 | 57 | 152 | 6.89E-03 | 7.39E-04 |
| 54 | 147 | 8.85E-06 | 4.06E-06 | 56 | 146 | 6.57E-01 | 8.34E-02 | 57 | 153 | 6.10E-04 | 7.14E-05 |
| 55 | 140 | 3.96E+00 | 6.08E-01 | 56 | 147 | 1.73E-01 | 3.23E-02 | 57 | 154 | 2.96E-05 | 6.25E-06 |
| 55 | 141 | 4.37E+00 | 4.98E-01 | 56 | 148 | 5.14E-02 | 6.21E-03 | 58 | 148 | 1.55E+00 | 4.17E-01 |
| 55 | 142 | 2.69E+00 | 2.99E-01 | 56 | 149 | 2.06E-02 | 2.66E-03 | 58 | 149 | 7.89E-01 | 1.41E-01 |
| 55 | 143 | 1.26E+00 | 1.46E-01 | 56 | 150 | 3.18E-03 | 3.32E-04 | 58 | 150 | 4.74E-01 | 7.52E-02 |
| 55 | 144 | 4.58E-01 | 6.42E-02 | 56 | 151 | 1.93E-04 | 2.42E-05 | 58 | 151 | 1.73E-01 | 3.27E-02 |
| 55 | 145 | 1.11E-01 | 2.77E-02 | 56 | 152 | 2.00E-05 | 4.17E-06 | 58 | 152 | 1.52E-01 | 2.11E-02 |
| 55 | 146 | 1.74E-02 | 2.39E-03 | 57 | 146 | 1.89E+00 | 2.80E-01 | 58 | 153 | 1.31E-02 | 2.57E-03 |
| 55 | 147 | 6.12E-03 | 1.06E-03 | 57 | 147 | 1.26E+00 | 1.64E-01 | | | | |
| 55 | 148 | 8.87E-04 | 9.49E-05 | 57 | 148 | 5.35E-01 | 7.39E-02 | | | | |

Appendix B

Measured fragmentation cross sections

In this appendix we present the isotopic cross sections of the fragmentation residues of reaction $^{132}\text{Sn}+\text{Be}$ at 950 A MeV.

Table B.1: Isotopic production cross sections (in mb) measured in the reaction $^{132}\text{Sn}+\text{Be}$ at 950 A MeV

| Z | A | σ_{f} | $\delta\sigma_{\text{f}}$ | Z | A | σ_{f} | $\delta\sigma_{\text{f}}$ | Z | A | σ_{f} | $\delta\sigma_{\text{f}}$ |
|----------|----------|---------------------|---------------------------|----------|----------|---------------------|---------------------------|----------|----------|---------------------|---------------------------|
| 51 | 130 | 1.38E+00 | 3.41E-01 | 48 | 126 | 5.26E+00 | 1.19E+00 | 46 | 122 | 1.70E-01 | 5.11E-02 |
| 51 | 131 | 1.55E+00 | 3.62E-01 | 48 | 127 | 2.65E+00 | 6.82E-01 | 46 | 123 | 6.99E-02 | 1.91E-02 |
| 51 | 132 | 7.31E-01 | 1.79E-01 | 48 | 128 | 2.00E+00 | 4.54E-01 | 46 | 124 | 5.29E-02 | 1.52E-02 |
| 50 | 127 | 2.98E+01 | 6.94E+00 | 48 | 129 | 9.46E-01 | 2.15E-01 | 46 | 125 | 7.68E-03 | 4.76E-03 |
| 50 | 128 | 2.00E+01 | 4.48E+00 | 48 | 130 | 3.95E-01 | 9.20E-02 | 45 | 114 | 7.87E-01 | 2.19E-01 |
| 50 | 129 | 2.93E+01 | 6.58E+00 | 47 | 120 | 2.61E+00 | 5.99E-01 | 45 | 115 | 4.81E-01 | 1.23E-01 |
| 50 | 130 | 4.28E+01 | 9.58E+00 | 47 | 121 | 2.96E+00 | 6.78E-01 | 45 | 116 | 3.38E-01 | 9.01E-02 |
| 50 | 131 | 1.45E+02 | 3.26E+01 | 47 | 122 | 1.43E+00 | 3.38E-01 | 45 | 117 | 8.14E-02 | 4.49E-02 |
| 49 | 125 | 8.71E+00 | 1.96E+00 | 47 | 123 | 1.98E+00 | 4.52E-01 | 45 | 119 | 4.17E-02 | 1.56E-02 |
| 49 | 126 | 1.35E+01 | 3.03E+00 | 47 | 124 | 6.83E-01 | 2.64E-01 | 45 | 120 | 2.21E-02 | 7.87E-03 |
| 49 | 127 | 1.21E+01 | 2.71E+00 | 47 | 125 | 3.98E-01 | 1.01E-01 | 45 | 121 | 8.50E-03 | 4.25E-03 |
| 49 | 128 | 1.60E+01 | 3.60E+00 | 47 | 126 | 2.32E-01 | 5.57E-02 | 44 | 111 | 3.02E-01 | 1.01E-01 |
| 49 | 129 | 2.74E+01 | 6.28E+00 | 47 | 127 | 1.47E-01 | 3.65E-02 | 44 | 112 | 1.55E-01 | 4.95E-02 |
| 49 | 130 | 2.39E+01 | 5.51E+00 | 47 | 128 | 2.21E-02 | 1.21E-02 | 44 | 113 | 1.07E-01 | 3.67E-02 |
| 49 | 131 | 1.54E+01 | 3.45E+00 | 47 | 129 | 5.53E-03 | 4.53E-03 | | | | |
| 48 | 122 | 6.00E+00 | 1.39E+00 | 46 | 117 | 8.83E-01 | 2.17E-01 | | | | |
| 48 | 123 | 7.97E+00 | 1.80E+00 | 46 | 118 | 9.36E-01 | 2.25E-01 | | | | |
| 48 | 124 | 4.58E+00 | 1.04E+00 | 46 | 119 | 5.91E-01 | 1.47E-01 | | | | |
| 48 | 125 | 5.36E+00 | 1.21E+00 | 46 | 120 | 4.51E-01 | 1.10E-01 | | | | |

Appendix C

Fit parameters for fission velocities

In this appendix we present the parameters obtained for the determination of the fission velocities according to following equation:

$$v_{fiss}(Z, A) = \frac{a + bA + cA^2}{1 + dA + eA^2} \quad (\text{C.1})$$

where Z and A are the atomic and mass number of the fragment, respectively

Table C.1: Parameters used for the determination of the fission velocities

| Z | a | b | c | d | e |
|----------|-------------|-------------|-------------|-------------|-------------|
| 23 | 1.6607e+00 | -4.1766e-02 | -6.9617e-02 | 4.3682e-04 | 7.3059e-04 |
| 24 | 1.6324e+00 | -4.0479e-02 | -6.6410e-02 | 4.1013e-04 | 6.7586e-04 |
| 25 | 1.5705e+00 | -3.8654e-02 | -6.1019e-02 | 3.7383e-04 | 5.9295e-04 |
| 26 | 1.5771e+00 | -3.7470e-02 | -5.9246e-02 | 3.5121e-04 | 5.5661e-04 |
| 27 | 1.6059e+00 | -3.6074e-02 | -5.8066e-02 | 3.2556e-04 | 5.2508e-04 |
| 28 | 1.5910e+00 | -3.5020e-02 | -5.5978e-02 | 3.0731e-04 | 4.9299e-04 |
| 29 | -8.1914e+01 | -1.2672e+01 | -1.8423e+01 | 2.1564e-01 | 3.3521e-01 |
| 30 | 1.6127e+00 | -3.2406e-02 | -5.2173e-02 | 2.6263e-04 | 4.2206e-04 |
| 31 | 1.5483e+00 | -3.1597e-02 | -4.8967e-02 | 2.4982e-04 | 3.8735e-04 |
| 32 | -5.8936e+01 | -1.2887e+00 | -3.8820e-01 | 1.9516e-02 | 1.9472e-02 |
| 33 | 1.5394e+00 | -1.4783e-02 | -2.2629e-02 | 0.0000e+00 | 0.0000e+00 |
| 34 | 1.2198e+00 | -3.3757e-02 | -4.3843e-02 | 2.8079e-04 | 3.7947e-04 |
| 35 | 1.2594e+00 | -3.2307e-02 | -4.2752e-02 | 2.5918e-04 | 3.5406e-04 |
| 36 | 4.7075e-01 | -3.3613e-02 | -2.6209e-02 | 2.8087e-04 | 2.7684e-04 |
| 37 | 5.4469e-01 | -5.0393e-02 | -5.2151e-02 | 4.9286e-04 | 5.9099e-04 |
| 38 | 1.4669e+00 | 0.0000e+00 | 0.0000e+00 | -1.7036e-04 | -2.4453e-04 |

Continued on next page

Table C.1: (continued)

| Z | a | b | c | d | e |
|----|------------|-------------|-------------|------------|------------|
| 39 | 1.1531e+00 | -3.0980e-02 | -3.7982e-02 | 2.3296e-04 | 2.9567e-04 |
| 40 | 1.2719e+00 | -4.3360e-01 | -6.0913e-01 | 5.2248e-03 | 7.2668e-03 |
| 41 | 1.1800e+00 | -2.4245e-02 | -2.9221e-02 | 1.4865e-04 | 1.8218e-04 |
| 42 | 1.1403e+00 | -2.4592e-02 | -2.8884e-02 | 1.5216e-04 | 1.8268e-04 |
| 43 | 1.0353e+00 | -2.6708e-02 | -2.9239e-02 | 1.7488e-04 | 1.9825e-04 |
| 44 | 1.1476e+00 | -2.1853e-02 | -2.5385e-02 | 1.2056e-04 | 1.4144e-04 |
| 45 | 1.1640e+00 | -2.0706e-02 | -2.4207e-02 | 1.0756e-04 | 1.2620e-04 |
| 46 | 1.0674e+00 | -2.2167e-02 | -2.4182e-02 | 1.2379e-04 | 1.3720e-04 |
| 47 | 1.1363e+00 | -1.9667e-02 | -2.2393e-02 | 9.6962e-05 | 1.1057e-04 |
| 48 | 1.0812e+00 | -1.9196e-02 | -2.0915e-02 | 9.3122e-05 | 1.0210e-04 |
| 49 | 1.0666e+00 | -1.8878e-02 | -2.0258e-02 | 8.9436e-05 | 9.6459e-05 |
| 50 | 8.4671e-01 | -2.2110e-02 | -2.0200e-02 | 1.2117e-04 | 1.1614e-04 |
| 51 | 8.3302e-01 | -2.0011e-02 | -1.7768e-02 | 1.0094e-04 | 9.3907e-05 |
| 52 | 8.1431e-01 | -1.9426e-02 | -1.6965e-02 | 9.5929e-05 | 8.8120e-05 |
| 53 | 8.8508e-01 | -2.5754e-02 | -2.4247e-02 | 1.4905e-04 | 1.4410e-04 |
| 54 | 4.3463e-01 | -1.9639e-02 | -1.1038e-02 | 9.6260e-05 | 6.3414e-05 |
| 55 | 6.9357e-01 | -1.8268e-02 | -1.3428e-02 | 8.3392e-05 | 6.4104e-05 |
| 56 | 9.0184e-01 | -1.6819e-02 | -1.5234e-02 | 7.0817e-05 | 6.4352e-05 |
| 57 | 6.5531e-01 | -2.0626e-02 | -1.5091e-02 | 1.0225e-04 | 7.9516e-05 |
| 58 | 2.6155e-01 | -2.3196e-02 | -1.1669e-02 | 1.2228e-04 | 7.6558e-05 |
| 59 | 6.5662e-01 | -2.0729e-02 | -1.5411e-02 | 1.0262e-04 | 8.1103e-05 |
| 60 | 6.3094e-01 | -7.7688e-02 | -6.4183e-02 | 5.4476e-04 | 4.5754e-04 |
| 61 | 7.7817e-01 | -1.5458e-02 | -1.2143e-02 | 5.9884e-05 | 4.7397e-05 |
| 62 | 7.7922e-01 | -1.4450e-02 | -1.1259e-02 | 5.2231e-05 | 4.0690e-05 |
| 63 | 7.7530e-01 | -2.6593e-02 | -2.1386e-02 | 1.3998e-04 | 1.1317e-04 |
| 64 | 7.0408e-01 | -1.3411e-02 | -9.4578e-03 | 4.5027e-05 | 3.1800e-05 |
| 65 | 7.0368e-01 | -1.3282e-02 | -9.4766e-03 | 4.5470e-05 | 3.2810e-05 |
| 66 | 6.6387e-01 | -1.2541e-02 | -8.3264e-03 | 3.9326e-05 | 2.6115e-05 |
| 67 | 6.6387e-01 | -1.2541e-02 | -8.3264e-03 | 3.9326e-05 | 2.6115e-05 |

Appendix D

Release efficiency from ISOL targets

In this appendix we present the release efficiencies used in this work for the estimation.

Table D.1: Release efficiencies from UC_X target

| Z | A | ϵ (%) | Z | A | ϵ (%) | Z | A | ϵ (%) |
|----------|----------|----------------|----------|----------|----------------|----------|----------|----------------|
| 27 | 70 | 4.00E+001 | 37 | 98 | 1.13E+001 | 38 | 105 | 2.56E-004 |
| 27 | 71 | 1.50E+001 | 37 | 99 | 8.23E+000 | 38 | 106 | 2.14E-004 |
| 27 | 72 | 8.00E+000 | 37 | 100 | 8.27E+000 | 38 | 107 | 1.25E-004 |
| 27 | 73 | 3.50E+000 | 37 | 101 | 6.86E+000 | 38 | 108 | 8.85E-005 |
| 27 | 74 | 3.50E+000 | 37 | 102 | 7.27E+000 | 38 | 109 | 5.74E-005 |
| 27 | 75 | 8.30E-001 | 37 | 103 | 5.22E+000 | 38 | 110 | 3.74E-005 |
| 31 | 81 | 2.60E+001 | 37 | 104 | 4.61E+000 | 38 | 111 | 2.84E-005 |
| 31 | 82 | 1.80E+001 | 37 | 105 | 4.49E+000 | 48 | 123 | 5.22E+001 |
| 31 | 83 | 1.10E+001 | 37 | 106 | 4.04E+000 | 48 | 124 | 3.31E+001 |
| 31 | 84 | 3.00E+000 | 37 | 107 | 3.77E+000 | 48 | 125 | 1.46E+001 |
| 31 | 85 | 2.00E+000 | 37 | 108 | 3.62E+000 | 48 | 126 | 1.06E+001 |
| 31 | 86 | 1.00E+000 | 38 | 96 | 3.28E-002 | 48 | 127 | 8.38E+000 |
| 36 | 95 | 7.00E+000 | 38 | 97 | 8.13E-003 | 48 | 128 | 5.04E+000 |
| 36 | 96 | 6.00E+000 | 38 | 98 | 1.54E-002 | 48 | 129 | 4.33E+000 |
| 36 | 97 | 5.00E+000 | 38 | 99 | 3.98E-003 | 48 | 130 | 2.06E+000 |
| 36 | 98 | 4.00E+000 | 38 | 100 | 2.57E-003 | 48 | 131 | 5.66E-001 |
| 37 | 94 | 3.13E+001 | 38 | 101 | 1.13E-003 | 48 | 132 | 9.62E-001 |
| 37 | 95 | 1.74E+001 | 38 | 102 | 4.96E-004 | 48 | 133 | 2.51E+000 |
| 37 | 96 | 1.40E+001 | 38 | 103 | 1.62E-004 | 48 | 134 | 1.74E+000 |
| 37 | 97 | 1.31E+001 | 38 | 104 | 5.15E-004 | 48 | 135 | 1.29E+000 |

Continued on next page

Table D.1: (continued)

| Z | A | ϵ (%) | Z | A | ϵ (%) | Z | A | ϵ (%) |
|----------|----------|----------------|----------|----------|----------------|----------|----------|----------------|
| 48 | 136 | 7.03E-001 | 53 | 144 | 6.19E+000 | 55 | 156 | 1.58E+000 |
| 48 | 137 | 2.00E-002 | 53 | 145 | 6.13E+000 | 55 | 157 | 1.33E+000 |
| 48 | 138 | 5.15E-002 | 53 | 146 | 3.81E+000 | 56 | 145 | 4.93E-002 |
| 48 | 139 | 1.61E-002 | 53 | 147 | 4.15E+000 | 56 | 146 | 2.49E-002 |
| 48 | 140 | 1.59E-002 | 53 | 148 | 3.86E+000 | 56 | 147 | 9.90E-003 |
| 48 | 141 | 1.73E-002 | 53 | 149 | 4.51E+000 | 56 | 148 | 6.73E-003 |
| 50 | 130 | 5.00E+001 | 53 | 150 | 2.95E+000 | 56 | 149 | 3.76E-003 |
| 50 | 131 | 4.40E+001 | 53 | 151 | 3.02E+000 | 56 | 150 | 3.27E-003 |
| 50 | 132 | 4.20E+001 | 53 | 152 | 2.61E+000 | 56 | 151 | 3.07E-003 |
| 50 | 133 | 9.00E+000 | 55 | 144 | 1.33E+001 | 56 | 152 | 2.06E-003 |
| 50 | 134 | 7.00E+000 | 55 | 145 | 9.69E+000 | 56 | 153 | 7.07E-004 |
| 50 | 135 | 3.00E+000 | 55 | 146 | 6.71E+000 | 56 | 154 | 9.38E-004 |
| 50 | 136 | 2.00E+000 | 55 | 147 | 5.50E+000 | 56 | 155 | 6.77E-004 |
| 50 | 137 | 1.00E+000 | 55 | 148 | 4.38E+000 | 56 | 156 | 6.03E-004 |
| 53 | 137 | 8.62E+001 | 55 | 149 | 4.94E+000 | 56 | 157 | 4.87E-004 |
| 53 | 138 | 6.98E+001 | 55 | 150 | 4.08E+000 | 56 | 158 | 3.63E-004 |
| 53 | 139 | 5.16E+001 | 55 | 151 | 3.14E+000 | 56 | 159 | 2.16E-004 |
| 53 | 140 | 3.39E+001 | 55 | 152 | 1.57E+000 | 56 | 160 | 1.98E-004 |
| 53 | 141 | 2.33E+001 | 55 | 153 | 2.22E+000 | 56 | 161 | 1.13E-004 |
| 53 | 142 | 1.46E+001 | 55 | 154 | 1.90E+000 | 56 | 161 | 1.13E-004 |
| 53 | 143 | 1.15E+001 | 55 | 155 | 1.74E+000 | | | |

Appendix E

Layers of matter in the beamline

List of the layers of matter used in the experiment described in this work, These layers are placed in the beam line on the particles analyzed in this work, from the exit of the SIS synchrotron to the final focal area (S4). Figures E.1 and E.2 show the experimental setup in S2 and S4 areas respectively.

Table E.1: Thicknesses of the layers of matter that constitute the different elements placed along the FRS beam line.

| Place | Material | Layer | thickness (mg/cm ²) | Place | Material | Layer | thickness (mg/cm ²) |
|-------|----------|--------------|---------------------------------|-------|-------------|---------------|---------------------------------|
| S0 | Ti | SIS Window | 4.5 | S2 | O | TPC1 windows | 0.78 |
| | Ti | SEETRAM | 13.5 | | Ar | TPC1 gas | 18.29 |
| | Pb | Target | 649 | | N | Air gap | 15.48 |
| | Pb | Target | 1534 | | O | Air gap | 4.74 |
| | Be | Target | 1036 | | Ar | Air gap | 0.26 |
| S1 | Al | Protection | 8.64 | | B | MUSIC windows | 4.22 |
| | C | Scintillator | 471.99 | | O | MUSIC windows | 56.87 |
| | H | Scintillator | 44.01 | | Na | MUSIC windows | 2.97 |
| | Al | Protection | 8.64 | | Al | MUSIC windows | 1.23 |
| S2 | Fe | Vac. Window | 78.66 | | Si | MUSIC windows | 39.76 |
| | N | Air gap | 18.21 | | K | MUSIC windows | 0.35 |
| | O | Air gap | 5.58 | | C | MUSIC gas | 22.52 |
| | Ar | Air gap | 0.31 | | F | MUSIC gas | 142.38 |
| | C | TPC1 windows | 2.59 | | C | MUSIC Mylar | 4.35 |
| | H | TPC1 windows | 0.10 | | H | MUSIC Mylar | 0.29 |
| | N | TPC1 windows | 0.27 | O | MUSIC Mylar | 2.32 | |

Continued on next page

Table E.1: (continued)

| Place | Material | Layer | thickness (mg/cm ²) | Place | Material | Layer | thickness (mg/cm ²) |
|-------|----------|-----------------|------------------------------------|-------|----------|---------------|------------------------------------|
| S2 | N | Air gap | 45.98 | S4 | Ti | Vac. Window | 90 |
| | O | Air gap | 14.09 | | N | Air gap | 16.84 |
| | Ar | Air gap | 0.77 | | O | Air gap | 5.16 |
| | C | TPC2 windows | 2.59 | | Ar | Air gap | 0.28 |
| | H | TPC2 windows | 0.10 | | C | TPC5 windows | 2.59 |
| | N | TPC2 windows | 0.27 | | H | TPC5 windows | 0.10 |
| | O | TPC2 windows | 0.78 | | N | TPC5 windows | 0.27 |
| | Ar | TPC2 gas | 18.29 | | O | TPC5 windows | 0.78 |
| | N | Air gap | 20.03 | | Ar | TPC5 gas | 18.29 |
| | O | Air gap | 6.14 | | N | Air gap | 23.22 |
| | Ar | Air gap | 0.34 | | O | Air gap | 7.12 |
| | Be | SecondaryTarget | 2591 | | Ar | Air gap | 0.39 |
| | N | Air gap | 18.21 | | B | MUSIC windows | 4.22 |
| | O | Air gap | 5.58 | | O | MUSIC windows | 56.87 |
| | Ar | Air gap | 0.31 | | Na | MUSIC windows | 2.97 |
| | C | TPC3 windows | 2.59 | | Al | MUSIC windows | 1.23 |
| | H | TPC3 windows | 0.10 | | Si | MUSIC windows | 39.76 |
| | N | TPC3 windows | 0.27 | | K | MUSIC windows | 0.35 |
| | O | TPC3 windows | 0.78 | | C | MUSIC gas | 22.52 |
| | Ar | TPC3 gas | 18.29 | | F | MUSIC gas | 142.38 |
| | N | Air gap | 76.48 | | C | MUSIC Mylar | 4.35 |
| | O | Air gap | 23.44 | | H | MUSIC Mylar | 0.29 |
| | Ar | Air gap | 1.29 | | O | MUSIC Mylar | 2.32 |
| | C | TPC4 windows | 2.59 | | N | Air gap | 25.04 |
| | H | TPC4 windows | 0.10 | | O | Air gap | 7.68 |
| | N | TPC4 windows | 0.27 | | Ar | Air gap | 0.42 |
| | O | TPC4 windows | 0.78 | | C | TPC6 windows | 2.59 |
| | Ar | TPC4 gas | 18.29 | | H | TPC6 windows | 0.10 |
| | N | Air gap | 23.22 | | N | TPC6 windows | 0.27 |
| | O | Air gap | 7.12 | | O | TPC6 windows | 0.78 |
| | Ar | Air gap | 0.39 | | Ar | TPC6 gas | 18.29 |
| | C | Scintillator | 370.44 | | N | Air gap | 60.55 |
| | H | Scintillator | 34.54 | | O | Air gap | 18.56 |
| | N | Air gap | 11.38 | | Ar | Air gap | 1.02 |
| | O | Air gap | 3.49 | | C | Scintillator | 370.44 |
| | Ar | Air gap | 0.19 | | H | Scintillator | 34.54 |
| | Ti | Vac. Window | 90 | | | | |

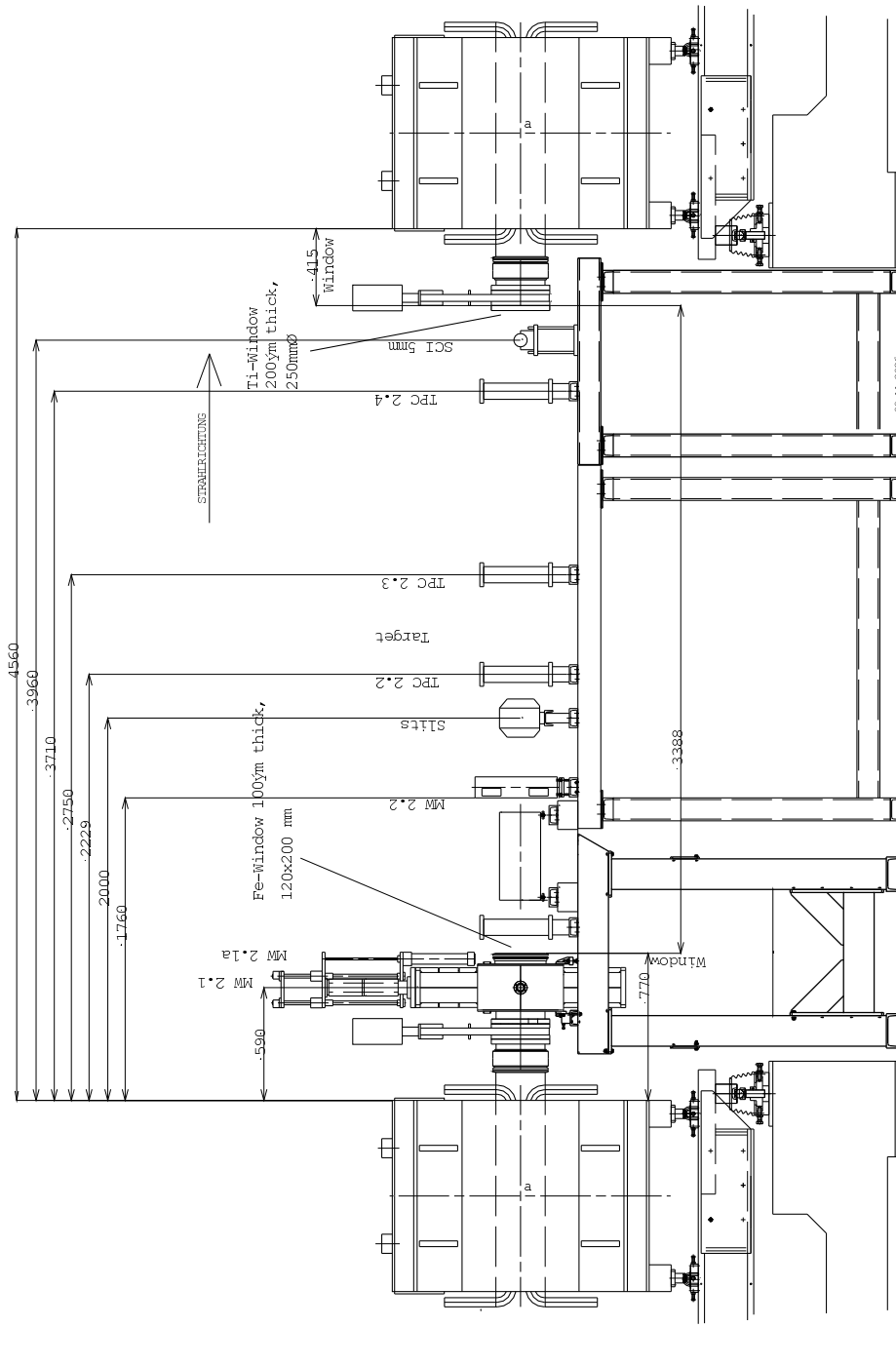


Figure E.1: Schematic view of the experimental setup placed at S2 intermediate focal plane. The arrows indicate the relative distances (in millimeters) between the different detectors.

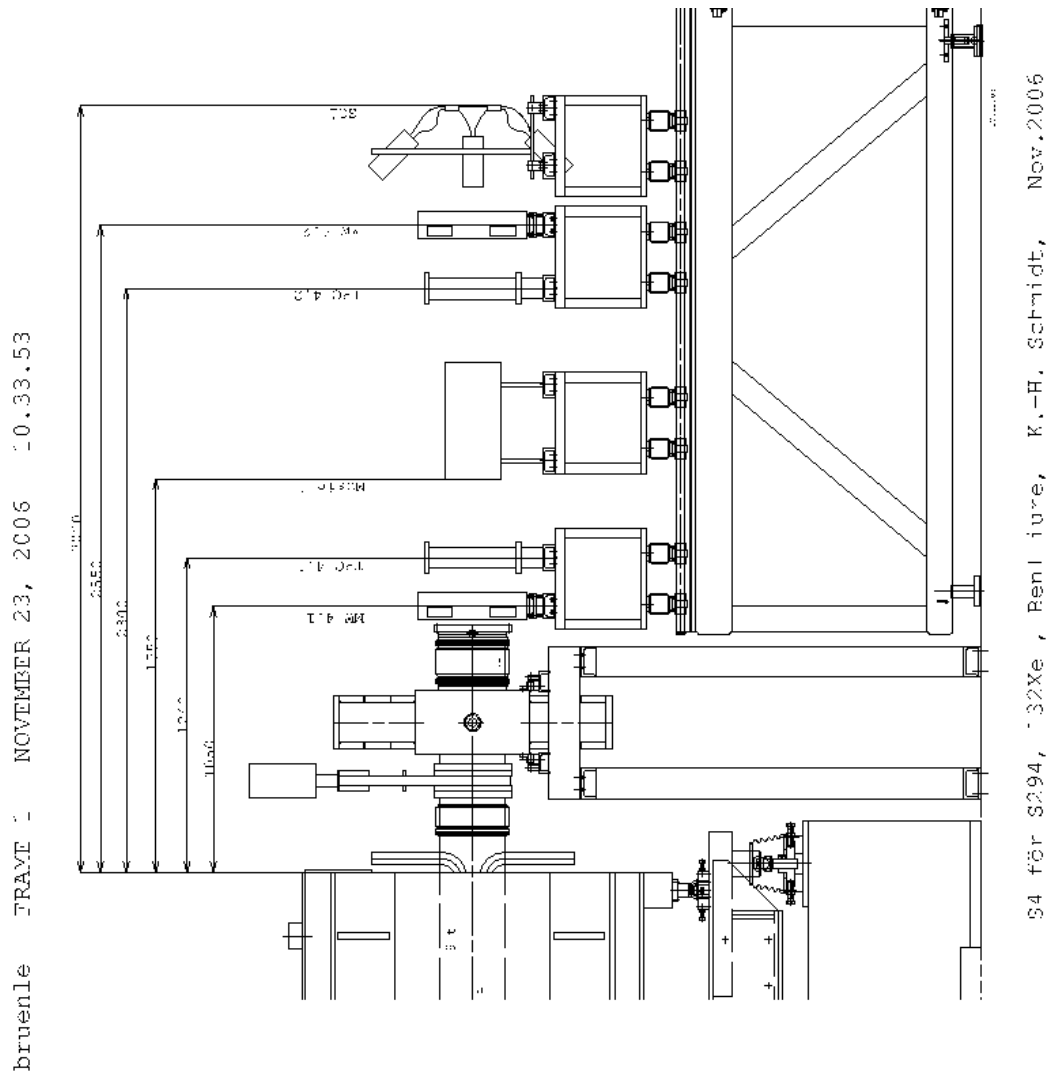


Figure E.2: Schematic view of the experimental setup placed at S4 final focal plane. The arrows indicate the relative distances (in millimeters) between the different detectors.

Bibliography

- [AMA] *AMADEUS is available online at*, <http://www-wnt.gsi.de/CHARMS/amadeus.htm>.
- [Ann87] R. Anne *et al.*, *The achromatic spectrometer LISE at GANIL*, Nuclear Instruments and Methods in Physics Research Section A: Accelerators, Spectrometers, Detectors and Associated Equipment **257** (1987) 215 – 232.
- [AP09] H. Alvarez-Pol *et al.*, *Production cross-sections of neutron-rich Pb and Bi isotopes in the fragmentation of ^{238}U* , The European Physical Journal A - Hadrons and Nuclei **42** (2009) 485–488.
- [Arm70] P. Armbruster, *On the calculation of charge values of fission fragments*, Nuclear Physics A **140** (1970) 385 – 399.
- [Bau07] T. Baumann *et al.*, *Discovery of ^{40}Mg and ^{42}Al suggests neutron drip-line slant towards heavier isotopes*, Nature (2007) 1022–1024.
- [Ben98] J. Benlliure *et al.*, *Calculated nuclide production yields in relativistic collisions of fissile nuclei*, Nuclear Physics A **628** (1998) 458 – 478.
- [Ben99] J. Benlliure *et al.*, *Production of neutron-rich isotopes by cold fragmentation in the reaction $^{197}\text{Au} + \text{Be}$ at 950 A MeV*, Nuclear Physics A **660** (1999) 87 – 100.
- [Ben08] J. Benlliure *et al.*, *Production of medium-mass neutron-rich nuclei in reactions induced by ^{136}Xe projectiles at 1 A GeV on a beryllium target*, Phys. Rev. C **78** (2008) 054605.
- [Ben10] J. Benlliure *et al.*, *Extending the north-east limit of the chart of nuclides*, arXiv:1004.0265v1 (2010).

- [Ber88] C. A. Bertulani and G. Baur, *Electromagnetic processes in relativistic heavy ion collisions*, Physics Reports **163** (1988) 299 – 408.
- [Ber97] M. Bernas *et al.*, *Discovery and cross-section measurement of 58 new fission products in projectile-fission of 750 A MeV ^{238}U* , Physics Letters B **415** (1997) 111 – 116.
- [Bet30] H. Bethe, *Zur Theorie des Durchgangs schneller Korpuskularstrahlen durch Materie*, Annalen der Physik **397** (1930) 325–400.
- [Boh36] N. Bohr, *Neutron Capture and Nuclear Constitution*, Nature (1936) 344–348.
- [Boh39] N. Bohr and J. A. Wheeler, *The Mechanism of Nuclear Fission*, Phys. Rev. **56** (1939) 426–450.
- [Bou02] A. Boudard *et al.*, *Intranuclear cascade model for a comprehensive description of spallation reaction data*, Phys. Rev. C **66** (2002) 044615.
- [Bow73] J. D. Bowman, W. J. Swiatecki and C. E. Tsang, *Abrasion and Ablation of Heavy Ions*, Lawrence Berkeley Laboratory report LBL-2980 (1973).
- [Bro90] U. Brosa, S. Grossmann and A. Müller, *Nuclear scission*, Physics Reports **197** (1990) 167 – 262.
- [Bur57] E. M. Burbidge *et al.*, *Synthesis of the Elements in Stars*, Rev. Mod. Phys. **29** (1957) 547–650.
- [Caa07] M. Caamaño *et al.*, *Resonance State in $H7$* , Phys. Rev. Lett. **99** (2007) 062502.
- [Car87] D. C. Carey, *The Optics of the Charged Particle Beams*, Harwood Academic Publishers (1987).
- [Cha98] R. J. Charity, *N - Z distributions of secondary fragments and the evaporation attractor line*, Phys. Rev. C **58** (1998) 1073–1077.
- [COF] *COFRA is available online at*, <http://www.usc.es/genp/cofra/>.
- [CRC] *CRC web page*, <http://www.cyc.ucl.ac.be/>.

- [Cug87] J. Cugnon, *Proton-nucleus interaction at high energy*, Nuclear Physics A **462** (1987) 751 – 780.
- [Enq99] T. Enqvist *et al.*, *Systematic experimental survey on projectile fragmentation and fission induced in collisions of ^{238}U at 1 A GeV with lead*, Nuclear Physics A **658** (1999) 47 – 66.
- [EUR] *EURISOL web page*, <http://www.eurisol.org>.
- [EUR09a] *Final Report of the EURISOL Design Study*, Technical report, EURISOL (2009).
- [EUR09b] *Final Report Task 11: Beam intensity calculations*, Technical report, EURISOL (2009).
- [EXC] *EXCYT web page*, <http://lnsweb.lns.infn.it/excyt/index.html>.
- [EXF] EXFOR (Experimental Nuclear Reaction Data). Available online at: <http://www-nds.iaea.org/exfor/exfor.htm>.
- [FAI] *FAIR web page*, <http://www.gsi.de/fair/>.
- [FRI] *FRIB web page*, <http://www.frib.msu.edu/>.
- [Gai91] J. J. Gaimard and K. H. Schmidt, *A reexamination of the abrasion-ablation model for the description of the nuclear fragmentation reaction*, Nuclear Physics A **531** (1991) 709 – 745.
- [GAN] *GANIL web page*, <http://www.ganil-spiral2.eu/>.
- [Gei92] H. Geissel *et al.*, *The GSI projectile fragment separator (FRS): a versatile magnetic system for relativistic heavy ions*, Nuclear Instruments and Methods in Physics Research Section B: Beam Interactions with Materials and Atoms **70** (1992) 286 – 297.
- [Gei03] H. Geissel *et al.*, *The Super-FRS project at GSI*, Nuclear Instruments and Methods in Physics Research Section B: Beam Interactions with Materials and Atoms **204** (2003) 71 – 85, 14th International Conference on Electromagnetic Isotope Separators and Techniques Related to their Applications.
- [Gio02] J. Giovinazzo *et al.*, *Two-Proton Radioactivity of ^{45}Fe* , Phys. Rev. Lett. **89** (2002) 102501.

- [GM84] D. Guillemaud-Mueller *et al.*, *[beta]-Decay schemes of very neutron-rich sodium isotopes and their descendants*, Nuclear Physics A **426** (1984) 37 – 76.
- [Go4] *Go4 web page*, <http://www-win.gsi.de/go4/>.
- [Gos77] J. Gosset *et al.*, *Central collisions of relativistic heavy ions*, Phys. Rev. C **16** (1977) 629–657.
- [Gre97] A. Grewe *et al.*, *Fission barriers from electromagnetic fission of 430 \AA MeV radioactive ion beams*, Nuclear Physics A **614** (1997) 400 – 414.
- [GSI] *GSI web page*, <http://www.gsi.de>.
- [Hau52] W. Hauser and H. Feshbach, *The Inelastic Scattering of Neutrons*, Phys. Rev. **87** (1952) 366–373.
- [Hel03] K. Helariutta *et al.*, *Model calculations of a two-step reaction scheme for the production of neutron-rich secondary beams*, Eur. Phys. J. A **17** (2003) 181–193.
- [HIE] *HIE ISOLDE web page*, http://hie-isolde.web.cern.ch/HIE-ISOLDE/HIE-ISOLDE_site/Welcome.html.
- [Hli98] V. Hlinka *et al.*, *Time projection chambers for tracking and identification of radioactive beams*, Nuclear Instruments and Methods in Physics Research Section A: Accelerators, Spectrometers, Detectors and Associated Equipment **419** (1998) 503 – 510.
- [HM06] A. Herrera-Martínez and Y. Kadi, *EURISOL-DS Multi-MW Target Comparative Neutronic Performance of the Baseline Configuration vs. the Hg-Jet Option*, Technical report, EURISOL Design Study (2006), available at http://www.eurisol.org/site02/doc_details.php?operation=download_dev&docu=565.
- [Hof82] S. Hofmann *et al.*, *Proton radioactivity of ^{151}Lu* , Zeitschrift für Physik A Hadrons and Nuclei **305** (1982) 111–123.
- [Hof00] S. Hofmann and G. Münzenberg, *The discovery of the heaviest elements*, Rev. Mod. Phys. **72** (2000) 733–767.
- [Hüf75] J. Hüfner, K. Schäfer and B. Schürmann, *Abrasion-ablation in reactions between relativistic heavy ions*, Phys. Rev. C **12** (1975) 1888–1898.

- [ISO] *ISOLDE web page*, <http://isolde.web.cern.ch/isolde/>.
- [Jon98] M. de Jong *et al.*, *Fragmentation cross sections of relativistic 208Pb projectiles*, Nuclear Physics A **628** (1998) 479 – 492.
- [Jun96] A. Junghans *et al.*, *A self-calibrating ionisation chamber for the precise intensity calibration of high-energy heavy-ion beam monitors*, Nuclear Instruments and Methods in Physics Research Section A: Accelerators, Spectrometers, Detectors and Associated Equipment **370** (1996) 312 – 314.
- [Jun98] A. R. Junghans *et al.*, *Projectile-fragment yields as a probe for the collective enhancement in the nuclear level density*, Nuclear Physics A **629** (1998) 635 – 655.
- [Jur02] B. Jurado, K. H. Schmidt and K. H. Behr, *Application of a secondary-electron transmission monitor for high-precision intensity measurements of relativistic heavy-ion beams*, Nuclear Instruments and Methods in Physics Research Section A: Accelerators, Spectrometers, Detectors and Associated Equipment **483** (2002) 603 – 610.
- [Jur04] B. Jurado *et al.*, *New signatures on dissipation from fission induced by relativistic heavy-ion collisions*, arXiv:nucl-ex/0403006 (2004).
- [Kar75] P. J. Karol, *Nucleus-nucleus reaction cross sections at high energies: Soft-spheres model*, Phys. Rev. C **11** (1975) 1203–1209.
- [Kor94] A. A. Korshennikov *et al.*, *Observation of 10He*, Physics Letters B **326** (1994) 31 – 36.
- [Kra40] H. A. Kramers, Physika VII (1940) 284.
- [Lew95] M. Lewitowicz *et al.*, *Observation of 100Sn*, Nuclear Physics A **583** (1995) 857 – 860, nucleus-Nucleus Collisions.
- [LIE] *LIESCHEN code is available on-line at:*, <http://www-wnt.gsi.de/charms/software.htm>.
- [Luk06] S. Lukic *et al.*, *Systematic comparison of ISOLDE-SC yields with calculated in-target production rates*, Nuclear Instruments and Methods in Physics Research Section A: Accelerators, Spectrometers, Detectors and Associated Equipment **565** (2006) 784 – 800.

- [Luk09] S. Lukyanov *et al.*, *Projectile fragmentation of radioactive beams of Ni68, Cu69, and Zn72*, Phys. Rev. C **80** (2009) 014609.
- [LYN] *LYNX OS web page*, <http://www.lynuxworks.com/>.
- [Mac65] R. D. Macfarlane and A. Siivola, *New Region of Alpha Radioactivity*, Phys. Rev. Lett. **14** (1965) 114–115.
- [MBS] *MBS web page*, <http://www-win.gsi.de/daq/>.
- [Met58] N. Metropolis *et al.*, *Monte Carlo Calculations on Intranuclear Cascades. I. Low-Energy Studies*, Phys. Rev. **110** (1958) 185–203.
- [MOC] *MOCADI web page*, <http://www-linux.gsi.de/~weick/mocadi>.
- [Möl03] P. Möller, B. Pfeiffer and K.-L. Kratz, *New calculations of gross β -decay properties for astrophysical applications: Speeding-up the classical r process*, Phys. Rev. C **67** (2003) 055802.
- [Mor75] L. G. Moretto, *Statistical emission of large fragments: A general theoretical approach*, Nuclear Physics A **247** (1975) 211 – 230.
- [Nol03] J. A. Nolen *et al.*, *Development of windowless liquid lithium targets for fragmentation and fission of 400-kW uranium beams*, Nuclear Instruments and Methods in Physics Research Section B: Beam Interactions with Materials and Atoms **204** (2003) 293 – 297, 14th International Conference on Electromagnetic Isotope Separators and Techniques Related to their Applications.
- [NSC] *NSCL web page*, <http://www.nsc1.msu.edu/>.
- [Oga06] Y. T. Oganessian *et al.*, *Synthesis of the isotopes of elements 118 and 116 in the Cf249 and Cm245 + Ca48 fusion reactions*, Phys. Rev. C **74** (2006) 044602.
- [Ord08] M. F. Ordóñez, *Peripheral collisions induced by ^{124}Xe and ^{136}Xe projectiles at relativistic energies*, Ph.D. thesis, Universidade de Santiago de Compostela (2008).
- [Oza00] A. Ozawa *et al.*, *New Magic Number, $N = 16$, near the Neutron Drip Line*, Phys. Rev. Lett. **84** (2000) 5493–5495.
- [Per07a] J. Pereira *et al.*, *Comprehensive analysis of fission-reaction properties in the nuclear spallation of U238(1 GeV/nucleon) on deuterium*, Phys. Rev. C **75** (2007) 044604.

- [Per07b] J. Pereira *et al.*, *Isotopic production cross sections and recoil velocities of spallation-fission fragments in the reaction [sup 238]U(1A GeV) + d*, Physical Review C (Nuclear Physics) **75** (2007) 014602.
- [RIB] *RIBF web page*, <http://www.phy.ornl.gov/hrifb/>.
- [RIK] *RIKEN web page*, <http://www.rarf.riken.go.jp/Eng/index.html>.
- [Sö0] K. Sümmerer and B. Blank, *Modified empirical parametrization of fragmentation cross sections*, Phys. Rev. C **61** (2000) 034607.
- [Sch93] K. H. Schmidt *et al.*, *Distribution of Ir and Pt isotopes produced as fragments of 1 A GeV 197Au projectiles: a thermometer for peripheral nuclear collisions*, Physics Letters B **300** (1993) 313 – 316.
- [Sch94] R. Schneider *et al.*, *Production and identification of 100Sn*, Zeitschrift für Physik A Hadrons and Nuclei **348** (1994) 241–242.
- [Sch00a] K. H. Schmidt *et al.*, *Relativistic radioactive beams: A new access to nuclear-fission studies*, Nuclear Physics A **665** (2000) 221 – 267.
- [Sch00b] R. Schneider and A. Stolz, *Technical Manual Ionisation Chamber MUSIC80* (2000).
- [Ser47] R. Serber, *Nuclear Reactions at High Energies*, Phys. Rev. **72** (1947) 1114–1115.
- [Sim99] H. Simon *et al.*, *Direct Experimental Evidence for Strong Admixture of Different Parity States in 11Li*, Phys. Rev. Lett. **83** (1999) 496–499.
- [Sou07] G. A. Souliotis *et al.*, *Neutron-rich rare isotope production below the Fermi energy and its application to the Texas A&M RIB upgrade*, The European Physical Journal - Special Topics **150** (2007) 325–327.
- [SPE] *SPES web page*, <http://www.lnl.infn.it/~spes/>.
- [SPI] *SPIRAL II web page*, <http://pro.ganil-spiral2.eu/spiral2>.

- [Ste91] H. Stelzer, *Multiwire chambers with a two-stage gas amplification*, Nuclear Instruments and Methods in Physics Research Section A: Accelerators, Spectrometers, Detectors and Associated Equipment **310** (1991) 103 – 106.
- [Suz95] T. Suzuki *et al.*, *Neutron Skin of Na Isotopes Studied via Their Interaction Cross Sections*, Phys. Rev. Lett. **75** (1995) 3241–3244.
- [Szi05] S. Szilner *et al.*, *Multinucleon transfer processes in Ca40 + Pb208*, Phys. Rev. C **71** (2005) 044610.
- [Tan85] I. Tanihata *et al.*, *Measurements of Interaction Cross Sections and Nuclear Radii in the Light p-Shell Region*, Phys. Rev. Lett. **55** (1985) 2676–2679.
- [TRI] *TRIUMF web page*, <http://www.triumf.ca/research/research-facilities/isac-facilities-for-rare-isotope-beams>.
- [Vio85] V. E. Viola, K. Kwiatkowski and M. Walker, *Systematics of fission fragment total kinetic energy release*, Phys. Rev. C **31** (1985) 1550–1552.
- [Wei37] V. Weisskopf, *Statistics and Nuclear Reactions*, Phys. Rev. **52** (1937) 295–303.
- [Wei40] V. F. Weisskopf and D. H. Ewing, *On the Yield of Nuclear Reactions with Heavy Elements*, Phys. Rev. **57** (1940) 472–485.
- [Wil76] B. D. Wilkins, E. P. Steinberg and R. R. Chasman, *Scission-point model of nuclear fission based on deformed-shell effects*, Phys. Rev. C **14** (1976) 1832–1863.
- [Win07] M. Winkler *et al.*, *The status of the Super-FRS at FAIR*, The European Physical Journal - Special Topics **150** (2007) 263–264.
- [Woo97] P. J. Woods and C. N. Davids, *NUCLEI BEYOND THE PROTON DRIP-LINE*, Annual Review of Nuclear and Particle Science **47** (1997) 541–590.
- [Yar79] Y. Yariv and Z. Fraenkel, *Intranuclear cascade calculation of high-energy heavy-ion interactions*, Phys. Rev. C **20** (1979) 2227–2243.

- [Yar81] Y. Yariv and Z. Fraenkel, *Intranuclear cascade calculation of high energy heavy ion collisions: Effect of interactions between cascade particles*, Phys. Rev. C **24** (1981) 488–494.
- [Yos96] Y. Yoshizawa *et al.*, *The study of countrate stability of photomultiplier tube with different types of voltage dividers*, IEEE Transactions on Nuclear Science **43** (1996) 1656–1660.
- [Yos04] A. Yoshida *et al.*, *High-power rotating wheel targets at RIKEN*, Nuclear Instruments and Methods in Physics Research Section A: Accelerators, Spectrometers, Detectors and Associated Equipment **521** (2004) 65 – 71, accelerator Target Technology for the 21st Century. Proceedings of the 21st World Conference of the International Nuclear Target Society.

Acknowledgments

It is always hard to write an acknowledgements page, because after having written it, one has always the feeling you forgot to acknowledge somebody. I will do my best and I will try not to forget anyone.

A thesis in experimental physics is always the result of the work of many people. I would like thank all the people who participated in the S294 experiment. From its preparation to the measurements which were carried out during November-December 2006. To all of them my deepest gratitude.

I am also indebted to my supervisor Prof. José Benlliure, who gave me the opportunity to join the Experimental Group of Nuclei and Particles (GENP) at the University of Santiago de Compostela, where I got involved in the research field of Nuclear Physics. Without his continuous encouragement and advice this work would never be possible.

I also wanted to thank the rest of the members of the GENP group for their support, specially to those who helped me during my daily work.

I would also like to express my gratitude to the members of the committee who evaluated this thesis for the interest they showed in the results of this work, and their comments and remarks to this manuscript

Finalmente, me gustaría agradecer a mi familia y mis padres su apoyo incondicional en todo y a mis amigos por todos los momentos inolvidables a lo largo de estos años.

This work was partially funded by the EC under the EURISOL-DS contract No. 515768 RIDS and by the Spanish Ministry of Education and Science under grant FPA2007-6252.